

RICE UNIVERSITY

**Numerical Investigations of Medical Applications of
Nanoparticles toward Tumor/Cancer Diagnosis and Treatment**

by

Xiao Xu

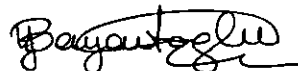
A THESIS SUBMITTED
IN PARTIAL FULFILLMENT OF THE
REQUIREMENTS FOR THE DEGREE

Doctor of Philosophy

APPROVED, THESIS COMMITTEE



Dr. Andrew J. Meade, Chair
Professor and Chair of Mechanical
Engineering and Material Science
Department, Rice University



Dr. Yildiz Bayazitoglu, Co-Chair
Harry S. Cameron Chair Professor of
Mechanical Engineering and Material
Science Department, Rice University



Dr. Jonghae Suh, Committee Member
Assistant Professor of Bioengineering
Department, Rice University

HOUSTON, TEXAS
December, 2012

Numerical Investigations of Medical Applications of
Nanoparticles toward Tumor/Cancer Diagnosis and
Treatment

Xiao Xu

December, 2012

Abstract

Almost a decade has passed ever since the first time nanoparticles were proposed to be used for tumor/cancer diagnosis and treatment. For tumor/cancer treatments, nanoparticles are usually engineered to be the photo-thermal agent to promote the selectivity of the photo-thermal therapy while the most promising diagnostic application for nanoparticles might be being used as the exogenous optical contrast agent for optical imaging technique. This study is targeted at developing numerical modeling & simulation to be a subsidiary tool of experimental investigation of diagnostic & therapeutic applications of nanoparticles, particularly, gold-silica nanoshells. Around this goal, the present study is comprised with four sub-projects, each would be presented as an independent chapter.

Firstly, an alternative method for calculating the spatial distribution of interstitial fluence rate in laser-induced interstitial thermo-therapy is introduced. The method originates from the un-simplified integral-differential radiant transport equation, which is then solved by the radial basis function collocation technique. Validation of the method against the stochastic Monte Carlo and the numerical finite volume method has been done. Secondly, the nanoparticle assisted laser-induced interstitial thermo-therapy for tumor/cancer treatments is numerically investigated, which was targeted at exploring the therapeutic effects of a variety of treatment conditions including laser wavelength, power, exposure time, concentrations of tai-

lored nanoparticles, and optical/thermal properties of the tissue that is under the treatment. Thirdly, the feasibility of extending nanoparticle assisted photo-thermal therapy from treating subcutaneous tumors to treating organ tumors, particularly, tumors growing in the clearance organ liver has been investigated. For organ tumors, nanoparticles could not recognize tumors from the surrounding normal organ tissue very well, as what has been for subcutaneous tumors. And last, how gold-silica nanoshells alter the diffuse reflectance signature of tissue phantoms has been numerically investigated, for the purpose of exploring how to engineering nanoshells to be good exogenous optical contrast agent for early-staged cancer diagnostic imaging.

Journal publications generated by this study:

1. **Xiao Xu**, Andrew Jr. Meade and Yildiz Bayazitoglu, “Feasibility of Selective Nanoparticle Assisted Photothermal Treatment for an Embedded Liver Tumor,” *Lasers in Medical Science* 2012, Accepted and to appear.
2. **Xiao Xu**, Andrew Jr. Meade and Yildiz Bayazitoglu, “Numerical Investigation of Nanoparticle Assisted Laser-induced Interstitial Thermo-therapy for Tumor and Cancer Treatments,” *Lasers in Medical Science* 26(2): 213-222, 2011.
3. **Xiao Xu**, Andrew Jr. Meade and Yildiz Bayazitoglu, “Fluence rate distribution in laser-induced interstitial thermotherapy by meshfree collocation,” *International Journal of Heat and Mass Transfer* 53: 4017-4022, 2010.

Manuscripts in progress:

1. **Xiao Xu**, Andrew Jr. Meade and Yildiz Bayazitoglu, “A numerical investigation of nanoshells as the exogenous optical contrast agent for early cancer diagnostic,” in preparation, 2012.

To the memory of my father

Contents

Abstract	i
List of Tables	vii
List of Figures	viii
Acknowledgements	xii
1 Introduction	1
2 Modeling fluence and distribution in laser-induced interstitial thermotherapy by meshfree collocation	5
2.1 Introduction	5
2.2 Mathematical formulation	7
2.3 Radial basis function collocation technique	11
2.4 Results and discussion	15
2.5 Conclusions	20
2.6 Remarks	21
3 Numerical investigation of nanoparticle-assisted laser-induced interstitial thermotherapy toward tumor and cancer treatments	26
3.1 Introduction	26
3.2 Mathematical and computational models	29
3.3 Results and discussion	35
3.4 Conclusions	43
3.5 Remarks	47

4	Feasibility of selective nanoparticle-assisted photothermal treatment for an embedded liver tumor	53
4.1	Introduction	53
4.2	Mathematical and computational models	55
4.3	Results and discussion	62
4.4	Conclusions	70
4.5	Remarks	71
5	A numerical investigation of nanoshells as the exogeneous optical contrast agent for early cancer diagnosis	78
5.1	Introduction	78
5.2	Mathematical modeling	81
5.3	Results and discussion	87
5.4	Conclusions	98
5.5	Remarks	99
6	Future work	116

List of Tables

3.1	Optical properties of types of human tissues under different wavelengths	35
3.2	Thermal properties of types of human tissues	37
4.1	Optical properties for the liver tumor and normal liver tissues	56
5.1	Optical properties under the wavelength 830nm for nanoshells of different size and core/shell ratio	89
5.2	Under the wavelength of 830nm, the overall optical properties of the tissue medium when the embedded nanoshells concentration is 1E9 nanoshells/ml	96
5.3	Under the wavelength of 830nm, the overall optical properties of the tissue medium when the embedded nanoshells concentration is 1E10 nanoshells/ml	96
5.4	Under the wavelength of 830nm, the overall optical properties of the tissue medium when the embedded nanoshells concentration is 1E11 nanoshells/ml	96

List of Figures

2.1	Layout of LITT experiment	7
2.2	Interstitial fluence rate (Wcm^{-2}) in the $z = 0$ plane for native human prostate. (a) $1064nm$ Nd: YAG laser adopted as energy source; (b) $980nm$ diode laser adopted as laser source; and (c) $850nm$ diode laser adopted as laser source. Results of Monte Carlo method are reconstructed according to data from (21)	16
2.3	Interstitial fluence rate (Wcm^{-2}) in the $z = 0$ plane for coagulated human prostate. (a) $1064nm$ Nd: YAG laser adopted as energy source; (b) $980nm$ diode laser adopted as laser source; and (c) $850nm$ diode laser adopted as laser source. Results of Monte Carlo method are reconstructed according to data from (21)	17
3.1	Layout of LITT experiment	29
3.2	Fluence rate and bioheat distribution along the radius in the $z = 0$ plane for the prostate cylinder	38
3.3	Fluence rate and bioheat distribution along the radius in the $z = 0$ plane for the breast cylinder	39
3.4	Fluence rate and bioheat distribution along the radius in the $z = 0$ plane for the brain cylinder	40
3.5	Transitions of temperature distributions along the radius in the $z = 0$ plane in the human prostate phantom	43
3.6	Transitions of temperature distributions along the radius in the $z = 0$ plane in the human brain phantom	44
3.7	Transitions of temperature distributions along the radius in the $z = 0$ plane in the human breast phantom	45
3.8	Temperature distribution after 90s of illumination in half of the human prostate phantom (nanoshell concentration is $4E9ml^{-1}$)	46

3.9	Temperature distribution after 90s of illumination in half of the human brain phantom (nanoshell concentration is $4E9ml^{-1}$)	47
3.10	Temperature distribution after 90s of illumination in half of the human breast phantom (nanoshell concentration is $4E9ml^{-1}$)	48
4.1	The layout of the PPTT experiment (not up to scale)	56
4.2	The distribution of the fluence rate (W/cm^2) within the study object (the liver tumor and surrounding normal liver tissues) when a the retention ratio = 0 : 0, b the retention ratio = 1/1, c the retention ratio = 2/1, d the retention ratio = 4/1, e the retention ratio = 8/1 .	63
4.3	The distribution of the thermal heat generation (W/cm^2) within the study object (the tumor and surrounding normal liver tissues) when a the retention ratio = 0 : 0, b the retention ratio = 1/1, c the retention ratio = 2/1, d the retention ratio = 4/1, e the retention ratio = 8/1 .	65
4.4	The temperature field ($^{\circ}C$) within the study object after 30s of laser exposure when a the retention ratio = 0 : 0, b the retention ratio = 1/1, c the retention ratio = 2/1, d the retention ratio = 4/1, e the retention ratio = 8/1	67
4.5	The temperature field ($^{\circ}C$) within the study object after 90 s of laser exposure when a the retention ratio = 0 : 0, b the retention ratio = 1/1, c the retention ratio = 2/1, d the retention ratio = 4/1, e the retention ratio = 8/1	69
5.1	Schematic illustrations: (a) Nanoshells embedded in bulky precancerous tissues; (b) Nanoshells embedded in precancerous tissue that is enclosed by normal tissues; (c) Nanoshells embedded in precancerous tissue that is enclosed by normal tissues, nanoshells found in both tissues	88
5.2	Transient diffuse reflectance at the laser emitting face when types of nanoshells were embedded in bulky cancerous tissues (absorption coefficient $k_{\alpha} = 0.05\text{ cm}^{-1}$, the scattering coefficient $k_s = 50\text{cm}^{-1}$) as the optical contrast agent. The embedded nanoshell concentration was $1E9$ nanoshells/ml	100
5.3	Transient diffuse reflectance at the laser emitting face when types of nanoshells were embedded in bulky cancerous tissues (absorption coefficient $k_{\alpha} = 0.05\text{ cm}^{-1}$, the scattering coefficient $k_s = 50\text{cm}^{-1}$) as the optical contrast agent. The embedded nanoshell concentration was $1E10$ nanoshells/ml	101

5.4	Transient diffuse reflectance at the laser emitting face when types of nanoshells were embedded in bulky cancerous tissues (absorption coefficient $k_\alpha = 0.05 \text{ cm}^{-1}$, the scattering coefficient $k_s = 50 \text{ cm}^{-1}$) as the optical contrast agent. The embedded nanoshell concentration was $1E11$ nanoshells/ml	102
5.5	Transient diffuse reflectance at the laser emitting face when types of nanoshells were embedded in cancerous tissues ($k_\alpha = 0.05 \text{ cm}^{-1}$, the scattering coefficient $k_s = 50 \text{ cm}^{-1}$) which were enclosed by normal healthy tissues (absorption coefficient $k_\alpha = 1.5 \text{ cm}^{-1}$, the scattering coefficient $k_s = 50 \text{ cm}^{-1}$) as the optical contrast agent. Nanoshells were found in cancerous tissues only, the nanoshell concentration is $1E9$ nanoshells/ml	103
5.6	Transient diffuse reflectance at the laser emitting face when types of nanoshells were embedded in cancerous tissues ($k_\alpha = 0.05 \text{ cm}^{-1}$, the scattering coefficient $k_s = 50 \text{ cm}^{-1}$) which were enclosed by normal healthy tissues (absorption coefficient $k_\alpha = 1.5 \text{ cm}^{-1}$, the scattering coefficient $k_s = 50 \text{ cm}^{-1}$) as the optical contrast agent. Nanoshells were found in the cancerous tissues only, the nanoshell concentration is $1E10$ nanoshells/ml	104
5.7	Transient diffuse reflectance at the laser emitting face when types of nanoshells were embedded in cancerous tissues ($k_\alpha = 0.05 \text{ cm}^{-1}$, the scattering coefficient $k_s = 50 \text{ cm}^{-1}$) which were enclosed by normal healthy tissues (absorption coefficient $k_\alpha = 1.5 \text{ cm}^{-1}$, the scattering coefficient $k_s = 50 \text{ cm}^{-1}$) as the optical contrast agent. Nanoshells were found in the cancerous tissues only, the nanoshell concentration is $1E10$ nanoshells/ml	105
5.8	Transient diffuse reflectance at the laser emitting face when types of nanoshells were embedded in cancerous tissues ($k_\alpha = 0.05 \text{ cm}^{-1}$, the scattering coefficient $k_s = 50 \text{ cm}^{-1}$) which were enclosed by normal healthy tissues (absorption coefficient $k_\alpha = 1.5 \text{ cm}^{-1}$, the scattering coefficient $k_s = 50 \text{ cm}^{-1}$) as the optical contrast agent. Nanoshells were found in both the cancerous tissues and the enclosing tissue, the nanoshell concentration in the enclosing tissue is $1E9$ nanoshells/ml, the nanoshell concentration in the enclosed cancerous tissue is $1E10$ nanoshells/ml	106

5.9 Transient diffuse reflectance at the laser emitting face when types of nanoshells were embedded in cancerous tissues ($k_{\alpha} = 0.05cm^{-1}$, the scattering coefficient $k_s = 50cm^{-1}$) which were enclosed by normal healthy tissues (absorption coefficient $k_{\alpha} = 1.5cm^{-1}$, the scattering coefficient $k_s = 50cm^{-1}$) as the optical contrast agent. Nanoshells were found in both the cancerous tissues and the enclosing tissue, the nanoshell concentration in the enclosing tissue is $1E10$ nanoshells/ml, the nanoshell concentration in the enclosed cancerous tissue is $1E11$ nanoshells/ml 107

Acknowledgements

I want to thank my advisors Dr. Yildiz Bayazitoglu and Dr. Andrew Jr. Meade for introducing me to this very meaningful and interesting topic, for always being patient and supportive when I got stuck working on the projects and for always being ready to discuss about the problems and difficulties I encountered. I also greatly appreciate the joint efforts of them to win the hard earned fundings so that my graduate study and research at Rice University could be completed. Also, I owe many thanks to Dr. Junghae Suh for her service in my dissertation defense committee and Dr. Andrew Dick for his service in my qualify exam committee.

Many thanks are owed to the Mechanical Engineering & Material Science department of Rice University for accommodating my study and research for six full years. The time I have spent here will be a life-long happy and inspiring memory for me. Thanks to the education and training I have received here, I have matured to be independent both intellectually and mentally. I thank professors, staff and fellow students and scholars here for making the department such a pleasant place to learn and work.

Finally, I want to thank the many fellow students and friends with whom I have co-teaching-assisted courses, co-survived classes and projects and eventually co-survived graduate school. The feeling of comradeship and fighting together has

helped me through some most difficult and self-doubted time of my life and I greatly appreciate that.

Agencies that funded this study include:

1. Texas Institute for Intelligent Bio-Nano Materials and Structures for Aerospace Vehicles
2. NASA NCC-1-02038
3. Rice Collaborative Advances in Biomedical Computing(CABC)
4. John Ann Doerr Fund for Computational Biomedicine

1

Introduction

Almost a decade has passed ever since the first time nanoparticles were proposed to be used for tumor/cancer diagnosis and treatment. For tumor/cancer treatments, nanoparticles are usually engineered to be the photo-thermal agent to promote the selectivity of the photo-thermal therapy while the most promising diagnostic application for nanoparticles might be being used as the exogenous optical contrast agent for optical imaging technique. This study is targeted at developing numerical modeling & simulation to be a subsidiary tool of experimental investigation of diagnostic & therapeutic applications of nanoparticles, particularly, gold-silica nanoshells. Around this goal, the study was comprised with four sub-projects, each would be listed as an independent chapter in the following up text, in which more details about the projects could be found. Here, a brief summary is given:

In chapter 2, an alternative method for calculating the spatial distribution of interstitial fluence rate in laser-induced interstitial thermotherapy(LITT) is introduced. The method originates from the un-simplified integral-differential radiant transport equation, which is then solved by the radial basis function collocation

technique. After comparing with the Monte Carlo and finite volume methods, it is concluded that this method is able to provide accurate predictions of fluence rate distributions along the penetration depth, particularly around the boundary.

In chapter 3, phantom based nanoparticle assisted laser-induced interstitial thermotherapy process for tumor/cancer treatments has been numerically investigated. The goal of this investigation is to explore the therapeutic effects of a variety of treatment conditions including laser wavelength, power, exposure time, concentrations of tailored nanoparticles, and optical/thermal properties of the tissue that is under the treatment. It is found that using absorbing preferential nanoparticles as the photo-thermal agent would weaken fluence rate distributions in terms of lowering fluence rate peaks and reducing the laser penetration depth. However, the local enhancement in absorption induced by nanoparticles is so significant that the reduced fluence rate will not only be balanced out but the eventual medical hyperthermia is greatly enhanced by using nanoparticles. Also, the results of numerical simulations indicate that with constant laser illumination, an increase in nanoparticle concentration beyond a certain range only has an insignificant impact on hyperthermia.

In chapter 4, the feasibility of extending nanoparticle assisted photothermal therapy (PPTT) from treating subcutaneous tumors to treating organ tumors, particularly, tumors growing in the clearance organ liver, has been numerically explored. A superficially embedded liver tumor and its immediate surrounding medium is selected as the study object. The tumor is externally irradiated by a $633nm$ laser beam of the intensity $1 - W/cm^2$. The matching [16, 21] nm gold-silica nanoshell with a $16 - nm$ silica core and a $5 - nm$ thick gold shell is used as the photothermal agent. The nanoshell retention ratio is varied to simulate different levels of nanoshell tumor discriminations. Laser light distributions, conversions from the photon energy

to heat and thermal responses of the tissues to the generated heat within the study object are analyzed. It is found that although nanoshells have enhanced the thermal transportation, they at the same time refrain the optical transportation of PPTT, indicating that PPTT is more demanding for laser delivery techniques compared to convention laser therapy. For the investigated case, when the nanoshell retention ratio is in the range of 2/1 - 4/1, the therapeutic effects is optimal: a confined medium temperature hyperthermia ($47 - 55^{\circ}\text{C}$) is achieved in the liver tumor while impacts on the surrounding health liver tissues are only marginal; When then nanoshell retention ratio is 8/1 or higher, about half of the liver tumor is ablated. However, part of the surrounding healthy liver tissue is sacrificed as well. PPTT therapeutic effects nonlinearly depends on the nanoshell tumor discriminations, better tumor discriminations does not necessarily result in better PPTT therapeutic effects.

Finally in chapter 5, how gold-silica nanoshells alter the diffuse reflectance signature of tissue phantoms has been investigated, for the purpose of exploring how to engineering nanoshells to be good exogenous optical contrast agent for early-staged cancer diagnostic imaging. Seven generics of nanoshells with different overall size and ratio of core radius-to-gold shell thickness are tested. Two of these generics are preferentially absorbing and the rest are preferentially scattering. Three phantom models have been used, including: (a) The laser lights directly illuminate the precancerous tissue bulk with nanoshells embedded within; (b) The precancerous tissue bulk is enclosed from the outside by the normal tissue bulk. Nanoshells are confined wholly in the precancerous tissue bulk; (c) the layout is the same as (b),but nanoshells are found in both the precancerous tissue bulk and the enclosing normal tissues bulk, with the nanoshell concentration in the normal tissue bulk ten times lower. The simulation results show that the all seven generics of nanoshells diminish the diffuse reflectance signature of the phantoms, at different levels. It is analyzed and argued

that whether a generic of nanoshell would augment or diminish the diffuse reflectance signature depends on whether the overall scattering albedo of the tissue medium is increased or decreased after the addition of nanoshells. Nanoshells whose scattering dominates the extinction spectrum are as capable of diminish the diffuse reflectance signature as nanoshells whose absorption dominates the extinction spectrum. It was also found that for all three phantom models, nanoshells could alter the diffuse reflectance signature significantly as long as sufficient amount of nanoshells could be deposited in the precancerous tissue bulk. Particularly, the diffuse reflectance signature in phantom (c) is altered the most while the diffuse reflectance signature in phantom (a) is altered the least, when same amount of same generic nanoshells are embedded.

Modeling fluence rate distribution in laser-induced interstitial thermotherapy by meshfree collocation

2.1 Introduction

The laser-induced interstitial thermo-therapy (LITT) is a minimally invasive treatment of deeply embedded cancers/tumors (1). During the treatment, the diffusing laser applicator is placed inside the cancer tissues/tumors for a period of time that lasts from minutes to tens of minutes. The goal of LITT is to “ burn out” targeted cancerous tissues/tumors while minimizing the lasers’ impact on surrounding healthy tissues and structures such as nerves and blood vessels. Because of potential damages to surrounding healthy tissues, accurate predictions of spatial distribution of laser fluence rate, laser energy absorption and subsequently, thermal response of biological tissues to the absorbed laser energy are crucial.

The first stage of LITT simulation is optical modeling, namely, the computation of spatial distributions of fluence rate and laser energy absorption. The second stage is bio-heat modeling, which simulates biological tissues’ thermal responses to the ab-

sorbed laser energy. For optical modeling, the Monte Carlo method (2; 3; 4) and the diffusion approximation (5) are two most commonly used tools. The Monte Carlo method is well known for its accuracy and flexibility handling complex computation geometry, though, the method's merits have been weakened by its prohibitively computation time cost, which actually prevents the method from becoming an ideal tool for clinical real-time usage. Particularly, if the Monte Carlo method is used for the optical modeling, because of the statistical nature of this method, extra work is usually required to bridge the optical modeling and bioheat modeling, which generally is handled by numerical techniques such as finite difference method (FDM), finite volume method (FVM) or finite element method (FEM). On the other hand, approximations such as diffusion approximation, P1 approximation and delta-P1 (6; 7; 8; 9; 10) are efficient in terms of computation time however, at the sacrifice of computation accuracy.

In this chapter, a new alternative to compute spatial distribution of interstitial laser fluence rate in LITT besides Monte Carlo and the mentioned approximations is brought forward. The proposed method starts from the un-simplified integro-differential radiative transfer equation (RTE) (11), which is the mathematical equivalence of Monte Carlo method. The RTE is then solved using the radial basis function collocation method, a technique which could be easily extended to bio-heat modeling. During the past decade, it has been more and more realized that mesh free techniques, with its many branches (12; 13; 14; 15; 16; 17; 18; 19; 20) maybe be more competent when handling problems that involves discontinuities, irregular geometry, large deformations and moving boundaries compared to the more traditional FDM, FVM and FEM. Particular to biomedicine research, this very technique has been tried in different aspects including biomedical imaging (18), medical image restoration (19), surgery plan optimization (20) and so on. In this chapter, this

technique's potential applications in laser therapy plan and real time monitor are exploited.

2.2 Mathematical formulation

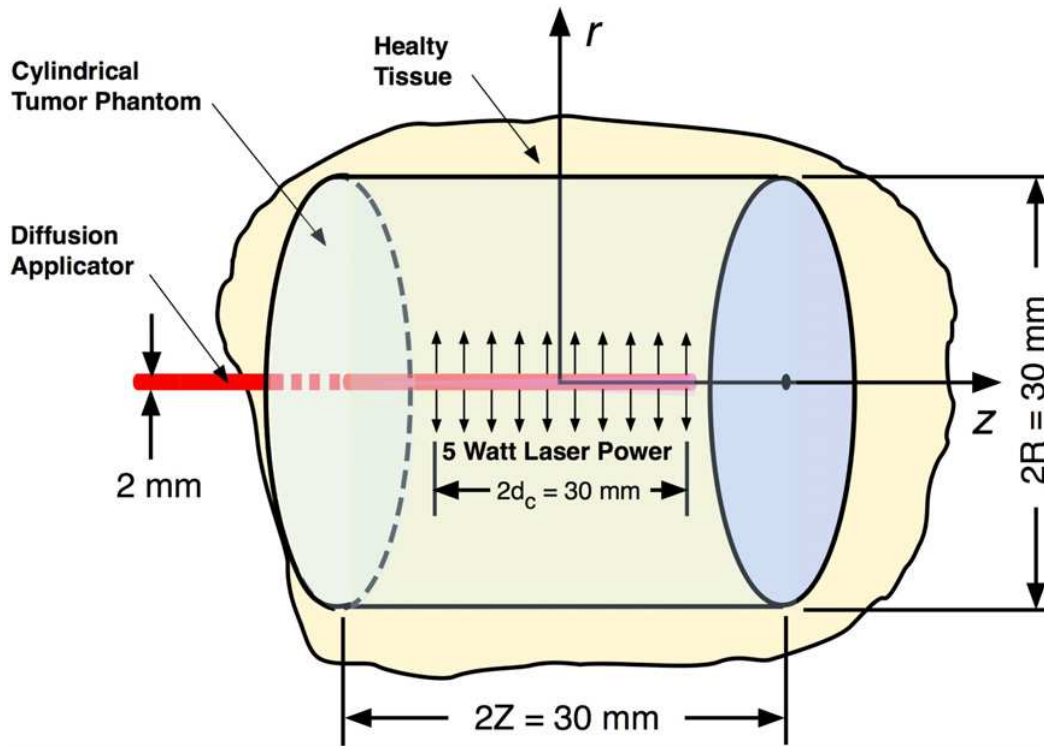


FIGURE 2.1: Layout of LITT experiment

The performing of LITT is achieved by placing fibers/diffusing applicators inside cancer tissues/tumors. According to Roggan et al (21), typical in LITT tumor treatment, lasers of the power of 3 – 10 Watts irradiate for a period of 10 – 20 minutes. And Nd: YAG laser (1064nm) or diode lasers (800 – 980nm) are most oftenly adopted as LITT laser sources.

The characteristics of fibers/applicators determine how the laser power would be applied to biological tissues (21). On the surface of the fiber/applicator, radiant intensity $L(\mathbf{r}, \mathbf{s})$ obeys the law of Fresnel reflection and after laser beam leaves the surface of the applicator and emits into the biological tissue, $L(\mathbf{r}, \mathbf{s})$ is comprised with two parts: (1) the remnant of collimation irradiance $L_c(\mathbf{r}, \mathbf{s})$, and (ii) the diffusion radiant intensity $L_d(\mathbf{r}, \mathbf{s})$, which is induced by the collimation irradiance $L_c(\mathbf{r}, \mathbf{s})$:

$$L(\mathbf{r}, \mathbf{s}) = L_c(\mathbf{r}, \mathbf{s}) + L_d(\mathbf{r}, \mathbf{s}) \quad (2.1)$$

The distribution of $L_c(\mathbf{r}, \mathbf{s})$ within the tissue is governed by the equation:

$$\mathbf{s} \cdot \nabla L_c(\mathbf{r}, \mathbf{s}) = -(k_\alpha + k_s)L_c(\mathbf{r}, \mathbf{s}) \quad (2.2)$$

Meanwhile is subjected to the boundary condition:

$$L_c(\mathbf{r}, \mathbf{s}) = [1 - R_{sp}]q_0\delta(\mathbf{s} - \mathbf{s}_c) \quad (2.3)$$

where k_α and k_s are absorption coefficient and scattering coefficient of the tissue individually, R_{sp} is the Fresnel specular reflection(1) and q_0 is the laser power.

The distribution of $L_d(\mathbf{r}, \mathbf{s})$ is governed by the integro-differential radiant transport equation (RTE) (22):

$$\frac{dL_d(\mathbf{r}, \mathbf{s})}{ds} = -(k_\alpha + k_s)L_d(\mathbf{r}, \mathbf{s}) + \frac{k_s}{4\pi} \int_{4\pi} \Phi(\mathbf{s}, \mathbf{s}')L_d(\mathbf{r}, \mathbf{s}')d\omega + S_c(\mathbf{r}, \mathbf{s}) \quad (2.4)$$

and is subjected to the following boundary conditions:

$$\begin{aligned}
& L_d(r = 1, z \in [-d_c, d_c], \mathbf{s}) \\
&= L_c(r = 1, z \in [-d_c, d_c])\delta[\mathbf{s} - \mathbf{s}_c] + \frac{R_d}{\pi} \int_{\mathbf{n} \cdot \mathbf{s}' < 0} L_d(r = 1, z \in [-d_c, d_c], \mathbf{s}') |\mathbf{n} \cdot \mathbf{s}'| d\omega' \quad (2.5)
\end{aligned}$$

$$L_d(r = 1, z \notin [-d_c, d_c], \mathbf{s}) = \frac{R_d}{\pi} \int_{\mathbf{n} \cdot \mathbf{s}' < 0} L_d(r = 1, z \notin [-d_c, d_c], \mathbf{s}') |\mathbf{n} \cdot \mathbf{s}'| d\omega' \quad (2.6)$$

$$L_d(r = R, z, \mathbf{s}) = \frac{R_d}{\pi} \int_{\mathbf{n} \cdot \mathbf{s}' < 0} L_d(r = R, z, \mathbf{s}') |\mathbf{n} \cdot \mathbf{s}'| d\omega' \quad (2.7)$$

$$L_d(r, z = |Z|, \mathbf{s}) = \frac{R_d}{\pi} \int_{\mathbf{n} \cdot \mathbf{s}' < 0} L_d(r, z = |Z|, \mathbf{s}') |\mathbf{n} \cdot \mathbf{s}'| d\omega' \quad (2.8)$$

where r is the radial position, z is the axial position ($\mathbf{r} = (r, z)$), d_c is the half width of the laser beam, R is the radius of the phantom cylinder, and Z is the half-length of the phantom cylinder, R_d is the reflectivity of the biological tissue, $\Phi(\mathbf{s}, \mathbf{s}')$ is the phase function, for turbid medium such as most biological tissues, the Henyey-Greenstein function (22) has most frequently been used to represent the phase function, and $S_c(\mathbf{r}, \mathbf{s})$ is the source term induced by collimation:

$$S_c(\mathbf{r}, \mathbf{s}) = \frac{k_s}{4\pi} \int_{4\pi} \Phi(\mathbf{s}, \mathbf{s}_c) L_c d\omega_c \quad (2.9)$$

At any location within the tissue phantom, the interstitial fluence rate $\Psi(\mathbf{r})$ can be computed by integrating $L(\mathbf{r}, \mathbf{s})$ over the space of solid angle:

$$\Psi(\mathbf{r}) = \int_{4\pi} L(\mathbf{r}, \mathbf{s}) d\omega = \int_{4\pi} [L_c(\mathbf{r}, \mathbf{s}) + L_d(\mathbf{r}, \mathbf{s})] d\omega \quad (2.10)$$

Solving Eqs. 2.2 and 2.3 to get $L_c(\mathbf{r}, \mathbf{s})$ is straightforward but numerical techniques are necessary to solve Eqs. 2.4, 2.5, 2.6, 2.7 and 2.8 to get $L_d(\mathbf{r}, \mathbf{s})$.

Under cylindrical coordinate, Eq.2.4 can be rewrote into the discrete form (2):

$$\frac{\mu}{r} \frac{\partial}{\partial r}(rL_d) - \frac{1}{r} \frac{\partial}{\partial \psi}(\eta L_d) + \xi \frac{\partial L_d}{\partial z} + (k_\alpha + k_s)L_d = \frac{k_s}{4\pi} \int_{4\pi} L_d \Phi(\mathbf{s}, \mathbf{s}') d\omega' + \frac{k_s}{4\pi} \int_{4\pi} L_c \Phi(\mathbf{s}, \mathbf{s}_c) d\omega_c \quad (2.11)$$

here \mathbf{s}_c indicates the direction of collimation and μ , η and ξ are directional cosines:

$$\mu = \sin(\theta) \cos(\psi)$$

$$\eta = \sin(\theta) \sin(\psi)$$

$$\xi = \cos(\theta)$$

and θ and ψ are polar angle and azimuthal angle, respectively.

The central difference scheme is applied for the ψ derivative in Eq. 2.11, representing it in terms of the quadrature weights (w and w'), and the term coefficient (α) as

$$\frac{\partial}{\partial \psi}(\eta L_d) \Big|_{\psi=\psi_i} \approx \frac{\alpha_{i+\frac{1}{2}} L_{d,i+1} - \alpha_{i-\frac{1}{2}} L_{d,i-1}}{2w_i'} \quad (2.12)$$

for $i = 1, 2, \dots, N$

here the subscript i is the index of discrete direction.

Eqs. 2.11, 2.5, 2.6, 2.7 and 2.8 are re-written below where the numerical quadratures replace the integral:

for $i = 1, 2, \dots, N$

$$\frac{\mu_i}{r} L_{d,i} + \mu_i \frac{\partial L_{d,i}}{\partial r} - \frac{\alpha_{i+\frac{1}{2}} L_{d,i+1} - \alpha_{i-\frac{1}{2}} L_{d,i-1}}{2r w_i'} + (k_\alpha + k_s) L_{d,i} = \frac{k_s}{4\pi} \sum_{i'=1, i' \neq i}^N L_{d,i'} \Phi_{i,i'} w_{i'} + \frac{k_s}{4\pi} L_c \Phi_{i_c, i} w_{i_c} \quad (2.13)$$

$$L_d(r = 1, z \in [-d_c, d_c], \mathbf{s}) = L_c(r = 1, z \in [-d_c, d_c]) \delta[\mathbf{s} - \mathbf{s}_c] + \frac{R_d}{\pi} \sum_{\mathbf{n} \cdot \mathbf{s}' < 0} w_{i'} L_{d,i'}(r = 1, z \in [-d_c, d_c], \mathbf{s}') |\mathbf{n} \cdot \mathbf{s}'| \quad (2.14)$$

$$L_d(r = 1, z \notin [-d_c, d_c], \mathbf{s}) = \frac{R_d}{\pi} \sum_{\mathbf{n} \cdot \mathbf{s}' < 0} w_{i'} L_{d,i'}(r = 1, z \notin [-d_c, d_c], \mathbf{s}') |\mathbf{n} \cdot \mathbf{s}'| \quad (2.15)$$

$$L_d(r = R, z, \mathbf{s}) = \frac{R_d}{\pi} \sum_{\mathbf{n} \cdot \mathbf{s}' < 0} w_{i'} L_{d,i'}(r = R, z, \mathbf{s}') |\mathbf{n} \cdot \mathbf{s}'| \quad (2.16)$$

$$L_d(r, z = |Z|, \mathbf{s}) = \frac{R_d}{\pi} \sum_{\mathbf{n} \cdot \mathbf{s}' < 0} w_{i'} L_{d,i'}(r, z = |Z|, \mathbf{s}') |\mathbf{n} \cdot \mathbf{s}'| \quad (2.17)$$

Term coefficient $\alpha_{i+\frac{1}{2}}$ and $\alpha_{i-\frac{1}{2}}$ in Eqs.2.13 obey the following recursion formula:

$$\alpha_{i+\frac{1}{2}} - \alpha_{i-\frac{1}{2}} = 2w_i' \mu_i \quad (2.18)$$

$$\alpha_{\frac{1}{2}} = \alpha_{N+\frac{1}{2}} = 0 \quad (2.19)$$

for $i = 1, 2, \dots, N$

2.3 Radial basis function collocation technique

In this section, it is demonstrated how radial basis function collocation methods could be applied to solve Eqs. 2.13, 2.14, 2.15, 2.16 and 2.17. Firstly, rewrite Eqs. 2.13, 2.14, 2.15, 2.16 and 2.17 in terms of operators:

$$\mathbf{L}_i L_{d,i}(r, z) = f_i \quad (2.20)$$

$$\mathbf{B}_i L_{d,i}(r, z) = g_i, \quad (2.21)$$

for $i = 1, 2, \dots, N$

where \mathbf{L}_i and \mathbf{B}_i are operators defined as

$$\mathbf{L}_i = \frac{\mu_i}{r} + \mu_i \frac{\partial}{\partial r} + \xi_i \frac{\partial}{\partial z} + (k_\alpha + k_s) \quad (2.22)$$

$$\mathbf{B}_i = 1 \quad (2.23)$$

The force functions f_i and g_i in Eqs.2.20 and 2.21 are individually defined as

$$f_i = \frac{k_s}{4\pi} \sum_{i'=1, i' \neq i}^N L_{d,i'} \Phi_{i',i} w_{i'} + \frac{k_s}{4\pi} L_{i_c} \Phi_{i_c,i} w_{i_c} + \frac{\alpha_{i+\frac{1}{2}} L_{d,i+1} - \alpha_{i-\frac{1}{2}} L_{d,i-1}}{2r w_i'} \quad (2.24)$$

$$g_i = L_c(r = 1, z \in [-d_c, d_c]) \delta(\mathbf{s} - \mathbf{s}_c) + \frac{R_d}{\pi} \sum_{\mathbf{n} \cdot \mathbf{s}' < 0} w_{i'} L_{d,i'}(r = 1, z \in [-d_c, d_c], \mathbf{s}') |\mathbf{n} \cdot \mathbf{s}'| \quad (2.25)$$

$$g_i = \frac{R_d}{\pi} \sum_{\mathbf{n} \cdot \mathbf{s}' < 0} w_{i'} L_{d,i'}(r = 1, z \notin [-d_c, d_c], \mathbf{s}') |\mathbf{n} \cdot \mathbf{s}'| \quad (2.26)$$

$$g_i = \frac{R_d}{\pi} \sum_{\mathbf{n} \cdot \mathbf{s}' < 0} w_{i'} L_{d,i'}(r = R, z, \mathbf{s}') |\mathbf{n} \cdot \mathbf{s}'| \quad (2.27)$$

$$g_i = \frac{R_d}{\pi} \sum_{\mathbf{n} \cdot \mathbf{s}' < 0} w_{i'} L_{d,i'}(r, z = |Z|, \mathbf{s}') |\mathbf{n} \cdot \mathbf{s}'| \quad (2.28)$$

Iterations are necessary to compute Eqs. 2.20 and 2.21, $L_{d,i+1}$ and $L_{d,i-1}$ in the third term on the RHS of Eq. 2.24 is evaluated based on results generated from the previous iteration.

According to (23; 24; 25) the approximate solution of Eqs. 2.20 and 2.21 can be written in the form of:

$$\hat{L}_{d,i}(r, z, c) = \sum_{j=1}^{K+K_B} \lambda_j \varphi(\|\mathbf{r} - \xi_j\|, c) \quad (2.29)$$

where $\lambda = [\lambda_1, \lambda_2, \dots, \lambda_K, \lambda_{K+1}, \dots, \lambda_{K+K_B}]$ is the vector of unknown coefficients that needs to be determined, $\|\mathbf{r} - \xi_j\|$ is the distance matrix, which is determined by positions of collocation points $\mathbf{r} = (r, z)$ and positions of collocation centers $\xi = (\xi_1, \xi_2)$. For 2D cylindrical problems, both collocation points and collocation centers are defined by their radial and axial positions. In Eq. 2.29, $\varphi(\|\cdot\|)$ represents the radial basis function and c is its shape parameter (26; 27), K is the number of collocation centers, including both centers that are laid out in the interior domain I and those that are laid out on the boundaries \mathbf{B} , K_B is the number of “extra” collocation centers that are laid out of the computation domain for the purpose of minimizing the boundary residual errors.

Collocate Eqs. 2.20 and 2.21 on all the collocation points, the resulting collocation matrix is:

$$(\tilde{A}_{\mathbf{L}_i})_{ij} = \mathbf{L}_i \varphi(\|\mathbf{r}_i - \xi_j\|, c) \quad (2.30)$$

$$\mathbf{r}_i \in \mathbf{I} \cup \mathbf{B}, \xi_j \in \Xi$$

$$(\tilde{A}_{\mathbf{B}})_{ij} = \varphi(\|\mathbf{r}_i - \xi_j\|, c) \quad (2.31)$$

$$\mathbf{r}_i \in \mathbf{B}, \xi_j \in \Xi$$

where $\mathbf{I} \cup \mathbf{B}$ is the set of collocation point while Ξ is the set of collocation centers.

Consequently, the matrix form of Eqs.2.20 and 2.21 is:

$$\begin{bmatrix} \tilde{A}_{\mathbf{L}_i} \\ \tilde{A}_{\mathbf{B}} \end{bmatrix} [\lambda] = \begin{pmatrix} f_i \\ g_i \end{pmatrix} \quad (2.32)$$

The most commonly used radial basis functions include the multiquadric radial basis function (RBF-MQ), the inverse multiquadric radial basis function (RBF-IMQ), the Gaussian radial basis function, the thin plate spline radial basis function (TPS-RBF), Wendland's compactly support radial basis functions (CSRBF), and Wu's compactly support radial basis function. For present work, the Gaussian radial basis function is adopted as the basis function:

$$\varphi_j(\mathbf{r}) = e^{-(c\|\mathbf{r}-\xi_j\|)^2} \quad (2.33)$$

Consequently, elements of the matrix in Eq.2.32 can be computed according to:

$$\begin{aligned} \mathbf{L}_i \varphi(\|\mathbf{r} - \xi\|, c) &= \mathbf{L}_i \varphi(\mathbf{r}, c) = \mathbf{L}_i \varphi(r, z, c) = \mathbf{L}_i e^{-(c\mathbf{r})^2} \\ &= e^{-(c\mathbf{r})^2} \left[(k_a + k_s - \frac{k_s \phi_{i,i}}{4\pi}) + \frac{\mu_i c^2}{2r} - 2\mu_i c^2 (r - \xi_1) - 2\eta_i c^2 (z - \xi_2) \right] \end{aligned} \quad (2.34)$$

Substitute Eq.2.34 into Eq.2.32 to achieve the coefficient vector λ . Then, replace the vector of collocation point \mathbf{r} in Eq.2.29 with the vector of evaluation points \mathbf{r}^* , and the solution at the evaluation positions can therefore be reached. The following are steps to follow when applying this technique to solve the RTE:

Step 1: Compute direction cosines ξ , η and μ and prepare sets for collocation points, collocation centers and evaluation points.

Step 2: Iteration starts. Define initial values for $\hat{L}_{d,i}$ ($i = 1, 2, \dots, N$) for all the collocation points.

Step 3: Construct collocation matrix according to Eqs. 2.30, 2.31, and 2.34. Construct force functions f_i and g_i for all collocation points according to Eqs. 2.24, 2.25, 2.26, 2.27 and 2.28 . If iteration index is 1, $\hat{L}_{d,i+1}$ and $L_{d,i-1}$ in Eq. 2.24 are determined based on the initial guesses and if iteration index is larger than 1, $\hat{L}_{d,i+1}$ and $L_{d,i-1}$ are from the previous iteration.

Step 4: Collocate according to Eqs. 2.30-2.32 to get the undetermined coefficient vector λ and then use the newly derived λ to update $\hat{L}_{d,i}$, force functions f_i and g_i for all the collocation points, following Eqs. 2.29, 2.24, 2.25, 2.26, 2.27 and 2.28 separately. Step 4 literally prepares for the next round of iteration.

Step 5: Use the derived λ to update $\hat{L}_{d,i}$ for all the evaluation points. Compare the new values of $\hat{L}_{d,i}$ at evaluation points with those from the previous iteration by calculating the L2 norm of errors. The iteration is terminated if the norm falls below the tolerance, otherwise, increase the iteration index by 1 and return to Step 3.

2.4 Results and discussion

The layout of LITT experiment investigated in this paper is presented in Fig. 2.1. The biological tissue that has been used to make the phantom cylinder is the human prostate, including both the human prostate in its native state and the human prostate in the coagulated state. The spatial distributions of interstitial fluence rate in the LITT experiment have been computed using both the radial basis function collocation method, and the finite volume method. The generated results are presented in Figs. 2.2 and 2.3. In both figures, solid lines represent results generated by the radial basis function collocation method, dashed lines represent results generated by the finite volume method and circles represent results generated by Monte

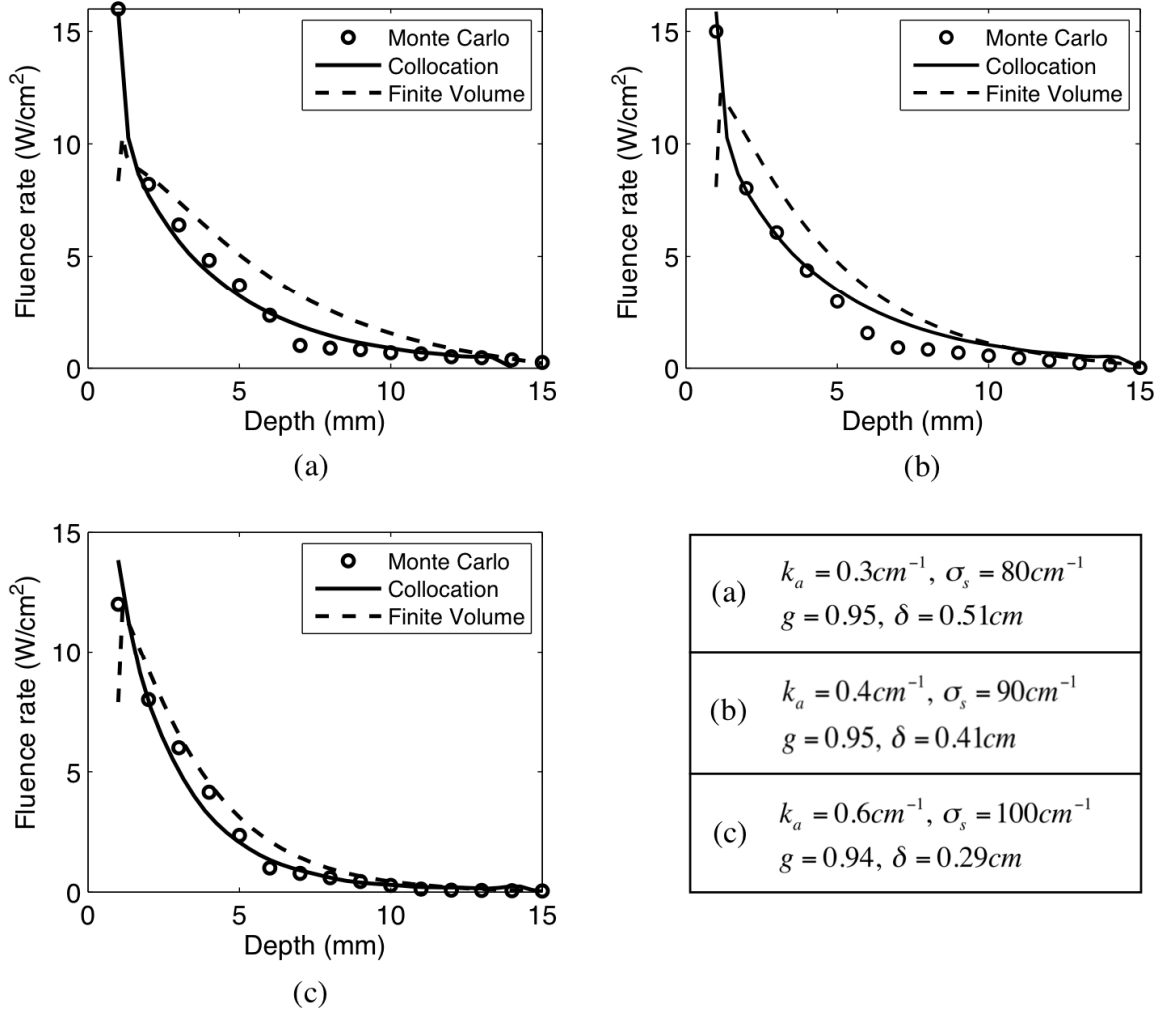


FIGURE 2.2: Interstitial fluence rate (Wcm^{-2}) in the $z = 0$ plane for native human prostate. (a) 1064nm Nd: YAG laser adopted as energy source; (b) 980nm diode laser adopted as laser source; and (c) 850nm diode laser adopted as laser source. Results of Monte Carlo method are reconstructed according to data from (21)

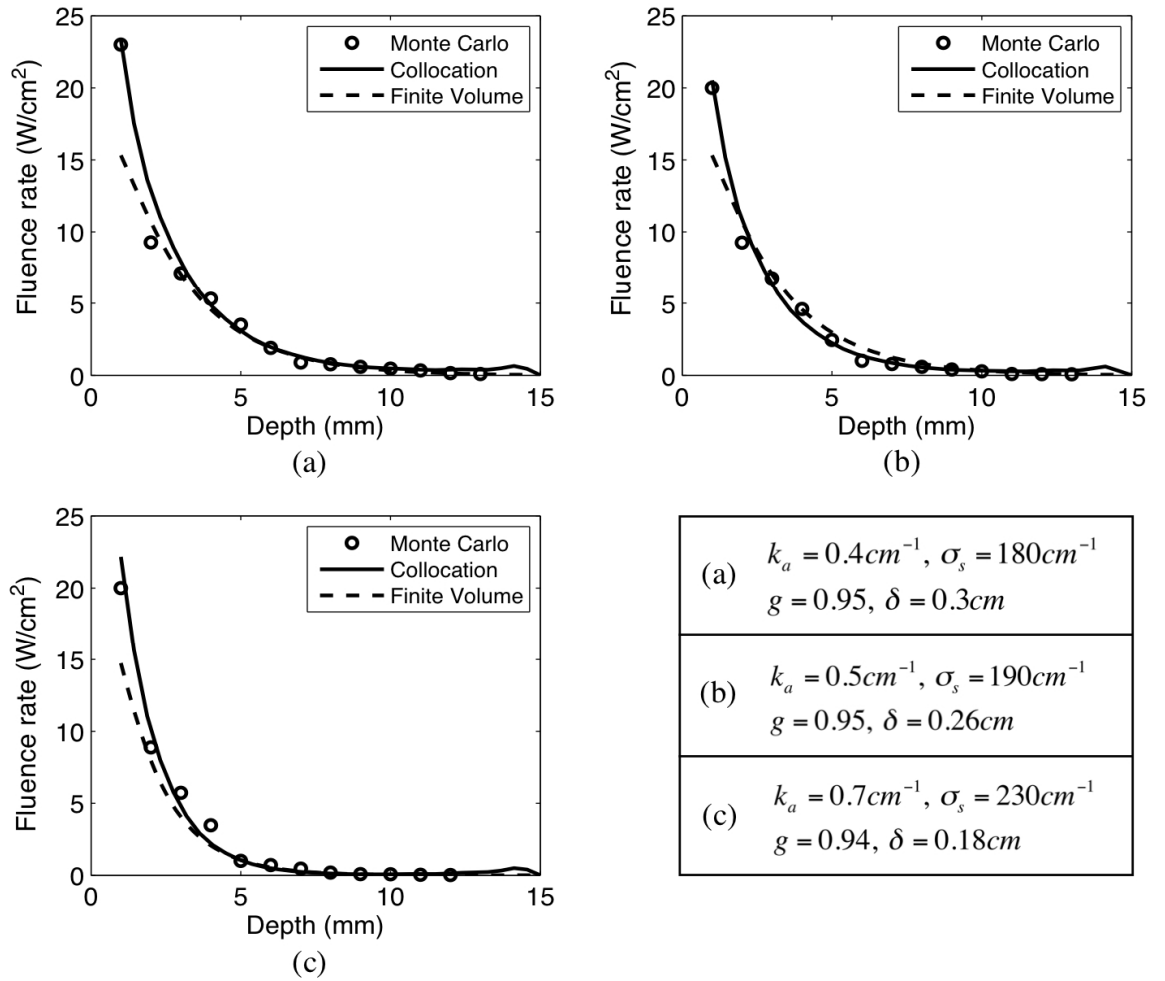


FIGURE 2.3: Interstitial fluence rate (Wcm^{-2}) in the $z = 0$ plane for coagulated human prostate. (a) 1064nm Nd: YAG laser adopted as energy source; (b) 980nm diode laser adopted as laser source; and (c) 850nm diode laser adopted as laser source. Results of Monte Carlo method are reconstructed according to data from (21)

Carlo method, which is taken from (21). Fig.2.2a shows how the interstitial fluence rate degrades along the depth direction in the $z = 0$ plane within the native stated prostate phantom. The laser used as illumination is Nd:YAG laser with a wavelength of $1064nm$. For this wavelength, native human prostate has an absorption coefficient of $0.3cm^{-1}$, a scattering coefficient of $80cm^{-1}$ and an anisotropy factor of 0.95. According to Fig. 2.2a, results generated by the radial basis function collocation method agree well with those generated by the Monte Carlo method, except for in the region where the depth distance is from $x = 7mm$ to $x = 9mm$, the radial basis function collocation method slightly over-predicts the fluence rate. The region that is within one mean free path from the surface of the diffusion applicator is usually defined as the near-boundary region, where the widely used diffusion approximation is known to be inaccurate. According to Fig. 2.2a, the radial basis function collocation method accurately predicts the fluence rate in the near-boundary region. The finite volume method, however, significantly under-predicts the fluence rate in the near-boundary region, while it over-predicts the fluence rate beyond the near-boundary region. For this case, the accuracy of the finite volume method is not very satisfactory.

Replace the Nd:YAG laser ($1064nm$) with a diode laser of the wavelength $980nm$ and repeat the numerical procedures, Fig. 2b shows how interstitial fluence rate degrades along penetration depth in the $z = 0$ plane. For this wavelength, native human prostate has an absorption coefficient of $0.4cm^{-1}$, a scattering coefficient of $90cm^{-1}$ and an anisotropy factor of 0.95 (21). According to Fig. 2.2b, the radial basis function collocation method agrees with the Monte Carlo method even better compared to Fig. 2.2a. There is no obvious discrepancy between the solid line, representing results from the radial basis function collocation method and the circles, representing results from the Monte Carlo method. Meanwhile, the finite volume method seems to still under-predict fluence rate in the near-boundary region and

over-predict fluence rate beyond this region.

Fig. 2.2c shows how the interstitial fluence rate degrades along penetration depth in the $z = 0$ plane when using the diode laser of wavelength $850nm$. For this wavelength, native human prostate has an absorption coefficient of $0.6cm^{-1}$, a scattering coefficient of $100cm^{-1}$ and an anisotropy factor of 0.94 (21). For this situation, results generated by both the radial basis function collocation method and the finite volume method agree with those generated by the Monte Carlo method, with the radial basis function collocation method still providing better approximations. The finite volume method still tends to slightly over-predict the fluence rate, however, the discrepancy is minimized compared to the previous two cases.

Fig. 2.3 shows how interstitial fluence rate degrades along the penetration depth in the $z = 0$ plane in the coagulated human prostate tissue phantom. Fig. 2.3a corresponds to the situation when Nd:YAG laser with wavelength of $1064nm$ is used as the laser source. For this wavelength, coagulated human prostate has an absorption coefficient of $0.4cm^{-1}$, a scattering coefficient of $180cm^{-1}$ and an anisotropy factor of 0.95 (21). Notice that under the same wavelength, coagulated prostate has a much larger scattering coefficient than the native prostate, indicating that scattering dominates more in coagulated prostate cylinder will result in stronger back scattering, and because of this stronger back scattering, in coagulated prostate cylinder, a much higher peak fluence rate can be expected: according to Fig. 2.2a, the peak fluence rate is around $15Wcm^{-2}$ while Fig. 2.3a shows the peak fluence rate is around $23Wcm^{-2}$. Fig.2.3a also shows that results generated by the radial basis function collocation method agree with those generated by the Monte Carlo method really well: the solid line almost overlap with circles. Finite volume method still appears to under-predict fluence rate in the near-boundary region, however, beyond

this region, the finite volume method gives good approximations as well.

Fig. 2. 3b and 2.3c shows how coagulated human prostate responds to diode lasers of different wavelengths. For the wavelength of $980nm$, coagulated human prostate has an absorption coefficient of $0.5cm^{-1}$, a scattering coefficient of $190cm^{-1}$ and an anisotropy factor of 0.95 (21). while for wavelength of $980nm$, coagulated human prostate has an absorption coefficient of $0.7cm^{-1}$, a scattering coefficient of $230cm^{-1}$ and an anisotropy factor of 0.94 (21). Both Fig. 2.3b and 2.3c shows that collocation method agrees with Monte Carlo results better while finite volume method under-predicts fluence rate in the near-boundary region but give very decent approximation beyond the near-boundary region. When comparing Figs.2.2 and 2.3, the radial basis function collocation provides satisfactory approximation for all types of situations, including the near-boundary region, where other widely used approximations such as diffusion approximation are known to fail to give good predictions. Similar to the diffusion approximation, the finite volume method tends to under-predict the fluence rate values in the near-boundary region, however, as scattering becomes more dominate, finite volume method gives better approximations.

2.5 Conclusions

In this chapter, an alternative to accurately calculate spatial distribution of interstitial fluence rate is proposed, which is important for LITT treatment plan. Based on comparisons against Monte Carlo method and the finite volume method, it is found that the proposed method is able to provide better accuracy approximations for all types of situations with less computation resources. Particularly, this method manages to predict the fluence rate in the near-boundary region accurately, while other widely used approximation methods such as diffusion approximation, P1 ap-

proximation and delta-P1 approximation are known to be inaccurate.

2.6 Remarks

This chapter is adapted from:

X. Xu, A. Meade, Jr. and Y. Bayazitoglu, “Fluence rate distribution in laser-induced interstitial thermotherapy by meshfree collocation”, *International Journal of Heat and Mass Transfer* 53: 4017-4022, 2010.

Bibliography

- [1] Masters A, Bown SG (1990) “Interstitial laser hyperthermia in the treatment of tumors”, *Lasers in Medical Science* 5: 129-136.
- [2] Wang LH, Jacques SL, Zheng LQ (2005) “MCML-Monte Carlo modeling of light transport in multi-layered tissues”, *Computer Methods and Programs in Biomedicine* 47: 131-146.
- [3] Jode ML(2000) “Monte Carlo simulations of light distributions in an embedded tumor model: studies of selectivity in photo-dynamic therapy”, *Lasers in Medical Science* 15: 49-56.
- [4] Welch AJ, Gardner CM(1997)“Monte Carlo model for determination of the role of heat generation in laser-irradiated tissue”, *Journal of Biomechanical Engineering* 119: 489-495.
- [5] Contini D, Martelli F and Zaccanti G(1997)“Photon migration through a turbid slab described by a model based on diffusion approximation. I. Theory”, *Applied Optics* 36: 458-459.
- [6] Carp SA, Prahl SA, and Venugopalan V(2004)“Radiative transport in the delta-P1 approximation: accuracy of fluence rate and optical penetration depth predictions in turbid semi-infinite media”, *Journal of Biomedical Optics* 9(3): 632-647.
- [7] Kienle A and Patterson MS(1997)“Improved solutions of the steady-state and the

- time resolved diffusion equations for reflectance from semi-infinite turbid medium”, *Journal of optical Society of American A*14: 246-254.
- [8] Vera J and Bayazitoglu Y(2009)“Gold nanoshell density variation with laser power for induced hyperthermia”,*Int. J. Heat Mass Transfer* 52: 564-573.
- [9] Vera J and Bayazitoglu Y(2009)“A note on laser penetration in nanoshell deposited tissue”, *International Journal of Heat Mass Transfer* 52(13/14): 3402-3406.
- [10] Elliot AM, Schwartz JS, Wang J, Shetty AM, Bougoyne C, ONeal D, Hazle J and Stafford RJ (2009) “Quantitative comparison of delta P1 versus optical diffusion approximations for modeling near-infrared gold nanoshell heating”,*Med, Phys* 36(4):1351-1358.
- [11] Chandrasekhar S(1960)“Radiative transfer”, New York: Dover.
- [12] Atluri SN, Shen S(2002)“The meshless local Petrov-Galerkin method”, Tech Science Press.
- [13] Liu GR(2003)“Mesh free methods: moving beyond the finite element method”, CRC Press.
- [14] Tan JY, Liu LH, Li BX(2006)“Least-squares collocation meshless approach for coupled radiative and conductive heat transfer”, *Numerical Heat Transfer, part B: Fundamentals* 49(2): 179-195.
- [15] Liu LH(2006)“Meshless method for radiation heat transfer in graded index medium”, *International Journal of Heat and Mass Transfer* 49(1-2): 219-229.
- [16] Singh IV(2004)“Meshless EFG method in three-dimensional heat transfer problems: A numerical comparison, cost and error analysis”, *Numerical Heat Transfer, part A: Applications* 46(2): 199-220.

- [17] Singh A, Singh IV, Prakash R(2007) “Meshless element free Galerkin method for unsteady nonlinear heat transfer problems”, *International Journal of Heat and Mass Transfer* 50(5-6): 1212-1219.
- [18] Fornefett M, Rohr K, and Stiehl HS(2001) “Radial basis functions with compact support for elastic registration of medical imaging”, *Image and Vision Computing*19: 87-96.
- [19] Carr JC, Fright WR(1997) “Surface interpolation with radial basis functions for medical imaging”, *IEEE Transactions on Medical imaging* 16(1): 96-107.
- [20] Erhart K, Divo E and Kassab A(2008) “An evolutionary-based inverse approach for the identification of non-linear heat generation rates in living tissues using a localized meshless method”, *International journal of Numerical Methods for Heat Fluid Flow*18(3/4): 401-414.
- [21] Muller G, Roggan A(1995) “Laser-induced interstitial thermotherapy”, SPIE Optical Engineering Press, Bellingham.
- [22] Waynant RW(2002) “Lasers in medicine”, CRC press.
- [23] Kansa EJ(1990) “Multiquadrics A scattered data approximation scheme with applications to computation fluid-dynamics-I: surface approximations and partial derivatives estimates”, *Computers and Mathematics with Applications*19: 127-145.
- [24] Kansa EJ(1990) “Multiquadrics A scattered data approximation scheme with applications to computation fluid-dynamcis-II: solution to parabolic, hyperbolic and elliptic partial differential equations”, *Computers and Mathematics with Applications* 19: 147-161.
- [25] Fedoseyev AI, Friedman MJ, and Kansa EJ (2002) “Improved multiquadric

method for elliptic partial differential equations via PDF collocation on the boundary”, *Computers and Mathematical Applications* 43: 439-455.

[26] Rippa S(1999) “An algorithm for selecting a good value for the parameter c in radial basis function interpolation”, *Advances in Computational Mathematics* 11:193-210.

[27] Wertz J, Kansa EJ, and Ling L(2006) “The role of the multiquadric shape parameters in solving elliptic partial differential equations”, *Computers and Mathematics with Applications* 51(8): 1335-1348.

Numerical investigation of nanoparticle-assisted laser-induced interstitial thermotherapy toward tumor and cancer treatments

3.1 Introduction

When applying medical lasers to treat tumors and cancers, in order to promote the transduction from laser photon energy to thermal energy and particularly, in order to improve lasers' discrimination between surrounding healthy tissues and targeted tumors and cancers, so that this treatment is "selective", photothermal agents are generally necessary. For the past decade, the organic dye indocyanine green (ICG) (1) has been used as the photothermal agent, which, unfortunately suffers from serious photo-bleaching. Currently, thanks to the fast development of nano science and technology, photothermal agents that are potentially much more powerful have been developed, namely, nano- particles.

Up to now, many types of nanoparticles have been tested as photothermal agents including nanospheres (2; 3; 4), nanorods (5; 6; 7), nanoshells (8; 9; 10; 11), carbon

nanotubes (12), and nanocages (13; 14). Among these, gold nanorods and silica- gold nanoshells have proven to be particularly promising. The primary advantage of these two types of nanoparticles over the others is the extremely agile tunability of their optical properties (9), specifically their surface plasmonic resonance (SPR) can be easily tuned to locate in the near- infrared spectrum (NIR) (750-1,100 nm), the well known “ therapeutic optical gateway ”. The nanorods and nanoshells can also be engineered to display absorption cross sections four to five orders higher than those of ICG, implying highly efficient NIR light absorption properties. Other advantages include suffering much less from photo- bleaching (15), low toxicity to the human body (16; 17), possibility of being multifunctional (7), facility of bio- conjugation and bio-modification (18) ,and so on.

Relevant literature (7) has suggested that nanoparticle- assisted laser therapy be named as plasmonic photothermal therapy (PPTT), to distinguish it from conventional photo- thermal therapy (PPT) (19). Halas et al. systematically performed experiments to study the biomedical potential of gold-silica nanoshells (8; 9; 10; 11) and reported that when using gold-silica nanoshells with a 110 – *nm* thick silica core and a 10 – *nm* thick gold shell as the photothermal agent, the threshold laser dose to achieve the desired hyperthermia was reduced by 10 to 25-fold, and the achieved hyperthermia was so highly conformal that the surrounding healthy tissue was left intact (8). In their investigation of diagnostic and therapeutic applications of gold nanorods, El-Sayed et al. also have reported successful achievement of “selective” photothermal therapy by using certain types of gold nanorods as the photothermal agent(7).

Though nanoparticles seem to hold considerable potentials, multiple treatment conditions must be carefully manipulated in order to achieve an effective PPTT

treatment. Manipulation of treatment conditions, which interact with each other nonlinearly, include selecting the proper laser wavelength, power and exposure time, selecting the proper type, number, and placement of fibers/ applicators, and selecting the type and concentration of nanoparticles. The process of manipulating the treatment conditions is called a therapy plan, and obviously, reliable preliminary information would be very helpful in constructing a therapy plan. Numerical modeling using sample phantoms is thought to be a most reliable and efficient way of gathering such information. Although there are several publications (20; 21; 22; 23) devoted to numerical modeling PPTT procedures, this field remains scantily explored.

In this chapter, we have numerically investigated phantom-based experiments of PPTT under different conditions. In particular, our work lies in a subfield of PPTT called nanoparticle-assisted laser-induced interstitial thermotherapy (LITT). LITT is a minimally invasive treatment for tumors that differs from other types of laser therapy in that through the treatment procedures, the diffusing laser applicator is placed inside the tumor instead of irradiating from the outside, enabling a more accurate and efficient delivery of energy dose to the targeted site. This characteristic makes LITT a popular option for well-developed, deeply embedded and relatively large tumors. In our study, different types of human tissues have been used to make the phantom and treatment conditions have been varied to test their therapeutic effects. The goal of the investigation is threefold: (i) to numerically test the feasibility of PPTT, (ii) to investigate the therapeutic effects of different treatment conditions, and thirdly, (iii) to test the usefulness of numerical guidance for a therapy plan.

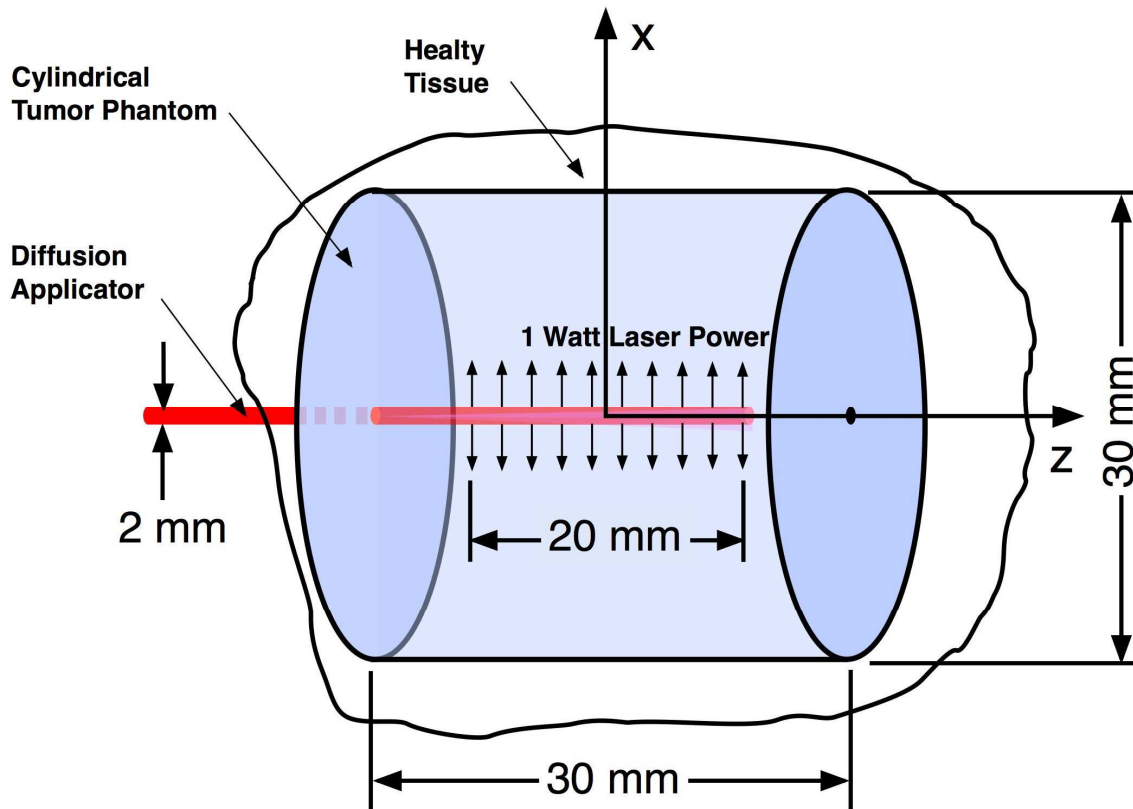


FIGURE 3.1: Layout of LITT experiment

3.2 Mathematical and computational models

Although most biological tissues are low absorbent to the NIR spectrum, the incubated nanoparticles could be engineered to be intense absorbers of NIR lights. These particles could possibly convert the laser photon energy to thermal energy and transport (diffuse) the thermal heat out to the surrounding medium within hundreds of picoseconds. Consequently, the numerical simulation of nanoparticle- assisted LITT can be approached as a two-staged procedure (20; 21; 22; 23), optical followed by

thermal modeling. The first stage (optical modeling) simulates the optical responses of biological tissues to laser (usually NIR) exposures by approximating the laser light (the fluence rate) distribution within the nanoparticle-embedded biological tissues. In the second stage (thermal modeling), the thermal responses, and consequent damages of tissues, are simulated by approximating the temperature distribution.

Our phantom-based LITT experiment, consisting of a cylindrical tissue phantom $30mm$ in length and having a radius of $15mm$, is illustrated in Fig. 3.1. A cylindrical diffusion applicator, with a working length of $20mm$ and $1 - mm$ radius, is inserted into the tissue phantom from the left. The laser beams exit the surface of the diffusion applicator along the working length and impinge the tissue medium.

Within the tissue, the radiant intensity $L(\mathbf{r}, \mathbf{s})$ is comprised of two parts: (i) the remnant of collimation irradiance $L_c(\mathbf{r}, \mathbf{s})$, and (ii) the diffusion radiant intensity $L_d(\mathbf{r}, \mathbf{s})$ that is induced by the collimation. The transportation of $L_d(\mathbf{r}, \mathbf{s})$ is governed by the radiant transport equation (24; 25):

$$\frac{dL_d(\mathbf{r}, \mathbf{s})}{d\mathbf{s}} + (k_\alpha(\mathbf{r}) + k_s(\mathbf{r}))L_d(\mathbf{r}, \mathbf{s}) = \frac{k_s(\mathbf{r})}{4\pi} \int_{4\pi} \Phi(\mathbf{s}, \mathbf{s}')d\omega' + S_c(\mathbf{r}, \mathbf{s}) \quad (3.1)$$

where \mathbf{r} indicates the position and \mathbf{s} indicates the direction, $k_\alpha(\mathbf{r})$ and $k_s(\mathbf{r})$ are local absorption and scattering coefficients, respectively, $\Phi(\mathbf{s}, \mathbf{s}')$ indicates the scattering phase function [34] and $S_c(\mathbf{r}, \mathbf{s})$ [Wmm^{-3}] indicates the source term induced by collimated irradiation:

$$S_c(\mathbf{r}, \mathbf{s}) = \frac{k_s(\mathbf{r})}{4\pi} \int_{4\pi} \Phi(\mathbf{s}, \mathbf{s}')L_c(\mathbf{r}, \mathbf{s}')d\omega' \quad (3.2)$$

According to Fig. 3.1, Eq. 3.1 is subjected to the following boundary conditions:

$$L_d(r = 1, z \in [-10, 10], \mathbf{s}) = L_c(r = 1, z \in [-10, 10])\delta[\mathbf{s} - \mathbf{s}_c] + \frac{R_d}{\pi} \int_{\mathbf{n} \cdot \mathbf{s}' < 0} L_d(r = 1, z \in [-10, 10], \mathbf{s}') |\mathbf{n} \cdot \mathbf{s}'| d\omega' \quad (3.3)$$

$$L_d(r = 1, z \notin [-10, 10], \mathbf{s}) = \frac{R_d}{\pi} \int_{\mathbf{n} \cdot \mathbf{s}' < 0} L_d(r = 1, z \notin [-10, 10], \mathbf{s}') |\mathbf{n} \cdot \mathbf{s}'| d\omega' \quad (3.4)$$

$$L_d(r = 15, z, \mathbf{s}) = \frac{R_d}{\pi} \int_{\mathbf{n} \cdot \mathbf{s}' < 0} L_d(r = 15, z, \mathbf{s}') |\mathbf{n} \cdot \mathbf{s}'| d\omega' \quad (3.5)$$

$$L_d(r, z = \pm 15, \mathbf{s}) = \frac{R_d}{\pi} \int_{\mathbf{n} \cdot \mathbf{s}' < 0} L_d(r, z = \pm 15, \mathbf{s}') |\mathbf{n} \cdot \mathbf{s}'| d\omega' \quad (3.6)$$

where r is the radial position, z is the axial position ($\mathbf{r} = (r, z)$) and R_d is the reflectivity of tissue.

According to the Beer-Lambert law, collimated lights decay exponentially as they propagate through the tissue medium:

$$L_c = q_0 \exp(-(k_\alpha + k_s)r) \delta(\mathbf{s} - \mathbf{s}_c) \quad (3.7)$$

where q_0 indicates the total laser photon flux, \mathbf{s}_c is the direction of collimated light.

As previously mentioned, when the laser light propagates through nanoparticle-incubated biological tissues, it is absorbed and scattered not only by the host tissue but also by the nanoparticles, therefore k_α and k_s in Eq. 3.1 and Eq. 3.7, are overall parameters that take into account contributions from both the biological tissue (20; 21; 22; 23) and the embedded nanoparticles:

$$k_\alpha = k_{\alpha,np} + k_{\alpha,t} \quad (3.8)$$

$$k_s = k_{s,np} + k_{s,t} \quad (3.9)$$

where the subscript np indicates properties of nanoparticles and the subscript t indicates properties of the biological tissue. Before PPTT procedures, nanoparticles need to be delivered to the tumor site first, which is usually achieved by direct injections to blood vessels. Nanoparticles would preferential accumulate on tumor sites through the blood circulation because of the leaky vasculature characteristics of tumors.

For spherical nanoparticles such as nanoshells and nanorods, $k_{\alpha,np}$ and $k_{s,np}$ can be quantified in terms of the absorption efficiency Q_{abs} and the scattering efficiency Q_{sca} (20; 21; 22):

$$k_{\alpha,np} = \pi r_0^2 Q_{abs} N_T \quad (3.10)$$

$$k_{sca,np} = \pi r_0^2 Q_{sca} N_T \quad (3.11)$$

where N_T is the number of nanoparticles per unit volume, for nanoshells r_0 indicates the radius of the core and for nanorods r_0 indicates the effective radius, Q_{abs} and Q_{sca} could be computed using Mie theory (26; 27; 28).

Numerical tools are generally necessary to solve Eq. 3.1 and Eqs.3.3 - 3.6. Under cylindrical coordinate system, the discrete form of the Eq. 3.1 is:

$$\frac{\mu}{r} \frac{\partial}{\partial r} (r L_d) - \frac{1}{r} \frac{\partial}{\partial \Psi} (\eta L_d) + \xi \frac{\partial L_d}{\partial z} + (k_\alpha + k_s) L_d = \frac{k_s}{4\pi} \int_{4\pi} L_d \Phi(\mathbf{s}, \mathbf{s}') d\omega' + S_c \quad (3.12)$$

where directional cosines μ , η , and ξ can be represented using polar angle θ and azimuthal angle ψ :

$$\mu = \sin(\theta)\cos(\psi) \quad (3.13)$$

$$\eta = \sin(\theta)\sin(\psi) \quad (3.14)$$

$$\xi = \cos(\theta) \quad (3.15)$$

The central difference scheme was applied to the derivative of ψ in Eq. 3.12, and the integrals in Eqs.3.3 - 3.6 and Eq. 3.12 were approximated by numerical quadratures. The resulting equations are well suited to numerical techniques such as the finite volume method:

$$\begin{aligned} \frac{\mu_i}{r} L_{d,i} + \mu_i \frac{\partial L_{d,i}}{\partial r} - \frac{\alpha_{i+\frac{1}{2}} L_{d,i+1} - \alpha_{i-\frac{1}{2}} L_{d,i-1}}{2r w_i'} + \xi_i \frac{\partial L_{d,i}}{\partial z} + (k_\alpha + k_s) L_{d,i} = \\ \frac{k_s}{4\pi} \sum_{i'=1, i' \neq i}^N L_{d,i'} \Phi_{i',i} w_{i'} + \frac{k_s}{4\pi} L_c \Phi_{i_c,i} w_{i_c} \end{aligned} \quad (3.16)$$

For $i=1,2,\dots,N$

$$\begin{aligned} L_d(r = 1, z \in [-10, 10], \mathbf{s}) = L_c(r = 1, z \in [-10, 10]) \delta[\mathbf{s} - \mathbf{s}_c] + \\ \frac{R_d}{\pi} \sum_{\mathbf{n} \cdot \mathbf{s}' < 0} w_{i'} L_{d,i'}(r = 1, z \in [-10, 10], \mathbf{s}') |\mathbf{n} \cdot \mathbf{s}'| \end{aligned} \quad (3.17)$$

$$L_d(r = 1, z \notin [-10, 10], \mathbf{s}) = \frac{R_d}{\pi} \sum_{\mathbf{n} \cdot \mathbf{s}' < 0} w_{i'} L_{d,i'}(r = 1, z \notin [-10, 10], \mathbf{s}') |\mathbf{n} \cdot \mathbf{s}'| \quad (3.18)$$

$$L_d(r = 15, z, \mathbf{s}) = \frac{R_d}{\pi} \sum_{\mathbf{n} \cdot \mathbf{s}' < 0} w_{i'} L_{d,i'}(r = 15, z, \mathbf{s}') |\mathbf{n} \cdot \mathbf{s}'| \quad (3.19)$$

$$L_d(r, z = \pm 15, \mathbf{s}) = \frac{R_d}{\pi} \sum_{\mathbf{n} \cdot \mathbf{s}' < 0} w_{i'} L_{d,i'}(r, z = \pm 15, \mathbf{s}') |\mathbf{n} \cdot \mathbf{s}'| \quad (3.20)$$

Term coefficients $\alpha_{i+\frac{1}{2}}$ and $\alpha_{i-\frac{1}{2}}$ in Eq. 3.16 obey the following recursion formula:

$$\alpha_{i+\frac{1}{2}} - \alpha_{i-\frac{1}{2}} = 2w_i' \mu_i \quad (3.21)$$

$$\alpha_{\frac{1}{2}} = \alpha_{N+\frac{1}{2}} = 0 \quad (3.22)$$

With the solution of Eqs. 3.16 -3.20, the distribution of $L_d(\mathbf{r}, \mathbf{s})$ can be determined and the local fluence rate $\Psi(\mathbf{r})$ can then be computed through integration of the directional radiant intensity $L(\mathbf{r}, \mathbf{s})$ over the whole solid space:

$$\Psi(\mathbf{r}) = \int_{4\pi} L(\mathbf{r}, \mathbf{s}) d\omega = \int_{4\pi} [L_d(\mathbf{r}, \mathbf{s}) + L_c(\mathbf{r}, \mathbf{s})] d\omega \quad (3.23)$$

However, the information that needs to be passed from optical to thermal modeling is thermal energy, which is transduced from laser photo energy, and theoretically can be computed as:

$$Q_s(\mathbf{r}) = k_\alpha(\mathbf{r}) \Psi(\mathbf{r}) \quad (3.24)$$

Later, $Q_s(\mathbf{r})$ will show as the source term in the bio-heat transportation equation.

As previously indicated, when nanoparticles are used as the photothermal agent, the incubated nanoparticles work as point-wise photon absorbers, converting the photon energy into heat and diffusing it out to its surrounding medium within hundreds of picoseconds. Generally, it has been agreed that from the macro perspective, the bio-heat equation is still applicable for describing this process and can be written in cylindrical coordinate system as:

$$\rho c \frac{\partial T(\mathbf{r}, t)}{\partial t} = \frac{1}{r} \frac{\partial}{\partial r} (rk \frac{\partial T(\mathbf{r}, t)}{\partial r}) + \frac{\partial}{\partial z} (k \frac{\partial T(\mathbf{r}, t)}{\partial z}) - v_B (T(\mathbf{r}, t) - T_{Arterial}) + Q_s(\mathbf{r}) \quad (3.25)$$

where t corresponds to the time, ρ , c , and k correspond to the density, specific heat, and thermal conductivity of the medium, respectively, T corresponds to the temperature, v_B indicates the rate of blood perfusion, and $Q_s(\mathbf{r})$ is the heat source term that has been computed in optical modeling.

At the boundaries, the tissue phantom is assumed to be cooled by natural convection:

$$k \frac{\partial T}{\partial r} \Big|_{r=15} = h(T - T_\infty) \quad (3.26)$$

$$k \frac{\partial T}{\partial z} \Big|_{z=\pm 15} = h(T - T_\infty) \quad (3.27)$$

where h indicates the convection coefficient and T_∞ indicates temperature of the environment.

3.3 Results and discussion

Table 3.1: Optical properties of types of human tissues under different wavelengths

Tissues	Wavelength(nm)	Abs coef(1/mm)	Sca coef(1/mm)	Sca albedo	Anisotropy(g)
prostate	850	0.4	10	0.9615	0.92
breast	633	0.02	39.4	0.9955	0.9
brain	633	0.026	5.7	0.9995	0.9

As previously discussed, treatment effects of PPTT procedures nonlinearly depend on multiple treatment conditions. In order to investigate this dependence, hyperthermia temperature distributions were simulated for various combinations of

treatment conditions.

Through this study, the laser power is fixed to be $1W$ with a resulting collimated radiant intensity of $0.8Wcm^{-2}$ emitting from the applicator surface. The other treatment conditions were varied: two different lasers have been used, one is a diode laser with a wavelength of $850nm$ and the other is a diode laser with a wavelength of $633nm$. As discussed in the introduction, the laser wavelength must match the wavelength under which the plasmonic resonance peak of nanoparticles occurs in order to ensure an efficient treatment. Consequently, two different types of gold-silica nanoshells were selected as the photothermal agent. For the $850nm$ diode laser, the silica-gold nanoshell with a silica core of $40nm$ and a gold shell of $30nm$ was used (from now on, this type of nanoshell is referred to as the $[40, 70]nm$ nanoshell, with $40nm$ corresponds to the inner radius of the nanoshell and $70nm$ corresponds to the outer radius).

According to (26), the $[40, 70]nm$ nanoshell has an absorption cross section $C_{abs} = 7.2712E - 14 m^2$ and a scattering cross section $C_{sca} = 6.54408E - 15 m^2$. The peak of plasmonic resonance of this type of nanoshell occurs at around $843nm$. For the $633 - nm$ diode laser, a silica-gold nanoshell with a silica core of $16nm$ and a gold shell of $5nm$ was used (from now on, this type of nanoshell is referred to as the $[16, 21]nm$ nanoshell with $16nm$ corresponds to the inner radius of the nanoshell and $21nm$ corresponds to the outer radius. According to (29; 30), the $[16, 21]nm$ nanoshell has an absorption cross section $C_{abs} = 4.7822E - 14 m^2$ and a scattering cross section $C_{sca} = 7.47314E - 16 m^2$. The plasmonic resonance peak of the $[16, 21]nm$ nanoshells occurs at around $631nm$. To test the relationship between exposure time and the achieved hyperthermia, the laser illumination time were set to be 30, 60, and 90s. The concentration values of $0 ml^{-1}$, $2E9 ml^{-1}$ and $4E9 ml^{-1}$

were tested for both type of nanoshells. Finally, in order to investigate the influences from host tissues, three different types of human tissues have been used to make the phantom cylinder, including human prostate, human brain, and human breast. The optical and thermal properties of these tissues can be found in Tables 3.1 and Table 3.2, respectively.

Table 3.2: Thermal properties of types of human tissues

Tissue types	Specific heat (J/gK)	Heat conductivity (W/Kcm)	Density (g/cm^3)
Human prostate	3.74	0.00529	1.05
Human breast	3.92	0.00499	0.99
Human brain	3.6	0.00515	1.035

The optical modeling results are shown in Fig. 3.2, Fig.3.3 and Fig.3.4. Figure 3.2 illustrate the results for the human prostate phantom incubated with $[40, 70]nm$ nanoshells and exposed to the $850-nm$ diode laser. Concentrations of the nanoshells were set to be 0, $2E9$, and $4E9 ml^{-1}$. Figure 3.2(left) presents the interstitial fluence rate distribution along the radius in the $z = 0$ plane. The figure indicates that nanoshells prevent the laser light from both diffusing out and penetrating deep into the tissue. The more nanoshells are incubated, the stronger this effect appears to be. When the phantom is clean of nanoshells, the fluence rate peak is approximately $2.5 Wcm^{-2}$, which drops to $1.5 Wcm^{-2}$ and $1.2 Wcm^{-2}$ when the nanoshell concentration is increased to $2E9 ml^{-1}$ and $4E9 ml^{-1}$, respectively. The physics behind the results presented in Fig. 3.2(left) is relatively straightforward. As laser light propagates in nanoparticle-incubated tissues, the light is absorbed/scattered by both the host tissue and the nanoparticles. Since therapeutic nanoparticles are engineered to be preferentially absorbing, lights extinct before they can actually diffuse out or propagate deeper. When planning a treatment, this calls for caution: NIR lasers are popular in medicine largely because most biological tissues are low absorbent to

this spectrum, and this very characteristic enables NIR lights to propagate deep into the tissue. However, when photothermal agents are used, this advantage is seriously weakened. This implies that the enhancement in energy transduction is achieved somehow at the sacrifice of laser penetration depth. Further research is required on how photon-thermal agents should be manipulated so that the best therapy can be achieved.

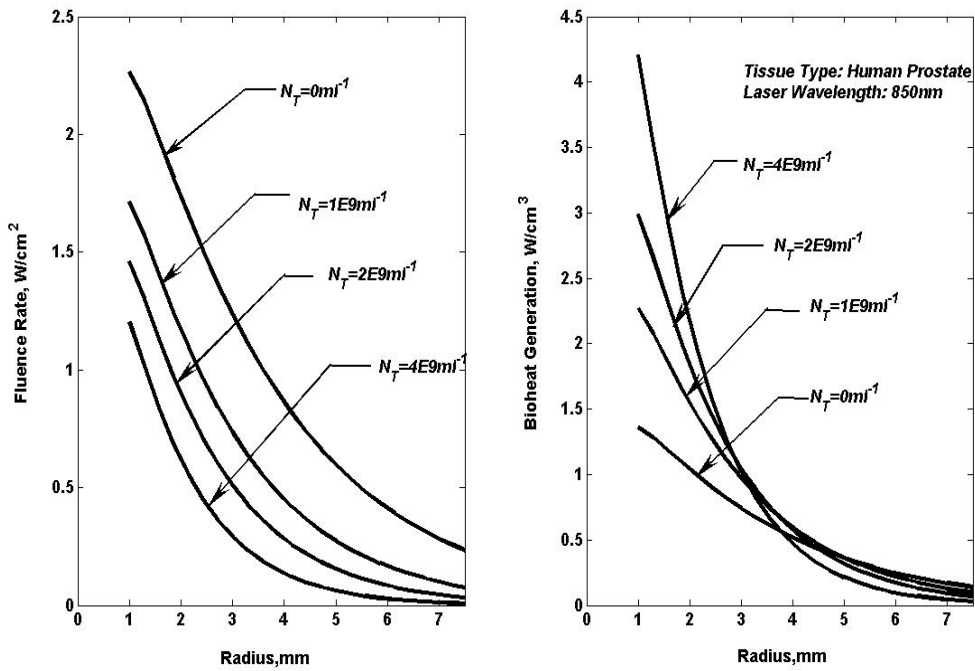


FIGURE 3.2: Fluence rate and bioheat distribution along the radius in the $z = 0$ plane for the prostate cylinder

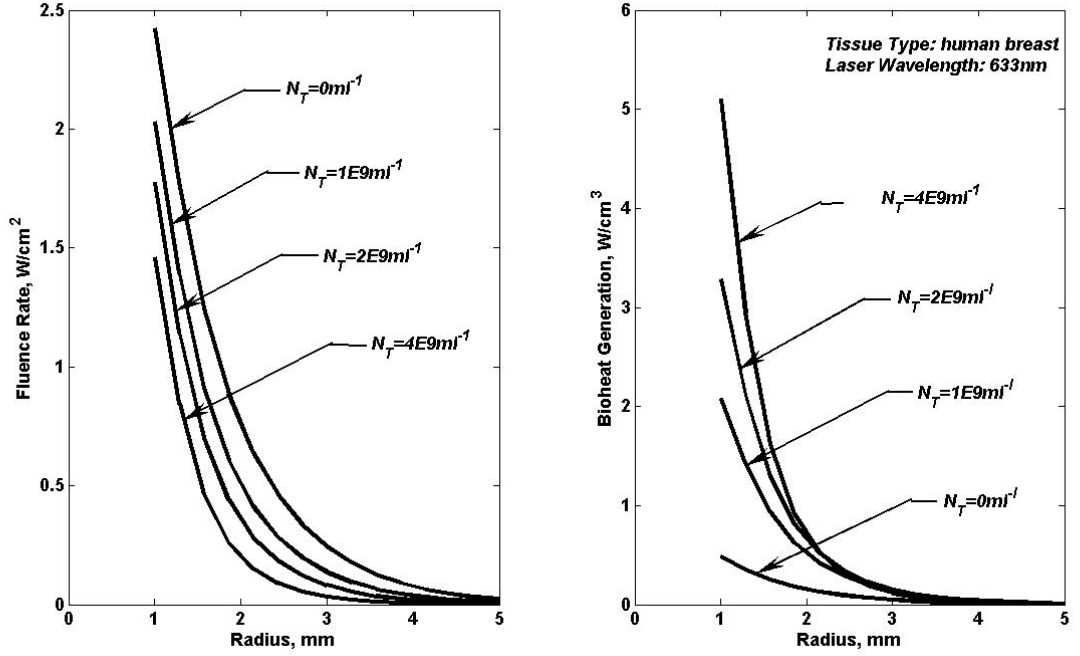


FIGURE 3.3: Fluence rate and bioheat distribution along the radius in the $z = 0$ plane for the breast cylinder

The phenomena presented in Fig. 3.2(left) can also be seen for the remaining two tissues incubated with $[16, 21]nm$ nanoshells and illuminated by a $633 - nm$ laser. Figure 3.3(left) and 3.3(right) present the interstitial fluence rate distributions along the radius in the $z = 0$ plane of the human breast and human brain phantom respectively. According to Fig. 3.2e, the fluence rate peak is $2.8 Wcm^{-2}$ when the brain phantom is clean of nanoshells, and drops to $1.5 Wcm^{-2}$ and $1.2 Wcm^{-2}$ when the concentrations of nanoshells increase to $2E9 ml^{-1}$ and $4E9 ml^{-1}$ respectively.

With the human breast phantom, Fig. 3.3(left) indicates that the fluence rate peak drops from $2.5 Wcm^{-2}$, when clean of nanoshells, to $1.75 Wcm^{-2}$ and then to 1.5

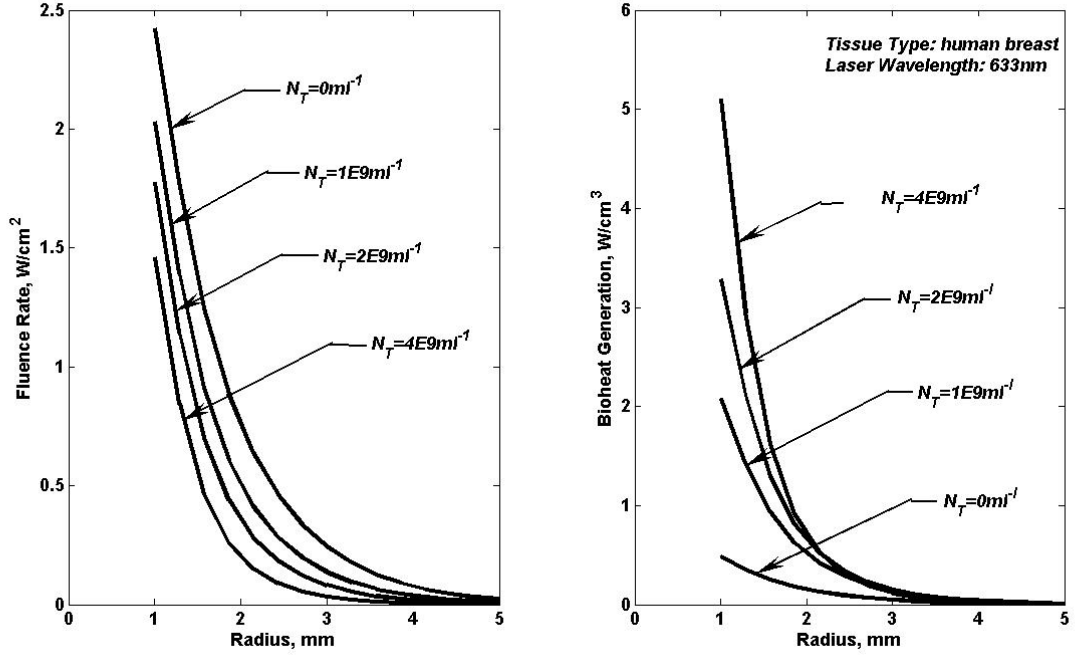


FIGURE 3.4: Fluence rate and bioheat distribution along the radius in the $z = 0$ plane for the brain cylinder

Wcm^{-2} with the increasing nanoparticle concentrations. Fig.3.2(right), Fig.3.3(right), and Fig.3.4(right) present bio-heat profiles along the radius in the $z = 0$ plane within the human prostate, breast, and brain tissue phantom, respectively. Bio-heat generation, which is a measure of the transduction between laser photon energy and thermal heat, can be computed by multiplying the local fluence rate with the local absorption coefficient. All three figures show that bio-heat profiles develop higher peak values and steeper slopes with increasing nanoparticle concentrations. This suggests that transductions from photon energy to thermal energy remain enhanced despite the fluence rate inefficiency.

If PPTT is to be used in conjunction with other therapies such as radiotherapy and chemotherapy, the targeted tissue might only need to be heated up to a temperature between 42 and 44 °C. However, if PPTT is intended to be an individual treatment, the targeted tissue needs to be heated up to a higher temperature between 47 and 55 °C . Specifically, if ablative tissue damage is intended, targeted tissues need to be heated up to above 55 °C. Whether targeted tissues could be heated up to the desired temperature within a short period of time is also important for an effective treatment.

Figure 3.5 presents the temperature distribution along the radius in the $z = 0$ plane within the human prostate phantom. According to Fig.3.5, tissue that is free of nanoparticles can only be heated slowly. For example, after 30s of illumination, the temperature peak increases to 42 °C from the original temperature of 37 °C, while after 90s of illumination, the temperature peak increases further to 46 °C. This is far below the temperature of 55 °C, under which ablative tissue damage is suppose to occur. When nanoshells are incubated into the tissue to a concentration of $2E9\text{ ml}^{-1}$, a temperature peak of 47 °C is achieved after only 30s of illumination. The peak climbs to 53 °C after 60s of illumination and 57 °C after 90s of exposure. The diameter of the region in which the temperature is above 47 °C, after 90s of exposure, is approximately 10mm. With the nanoshell concentration being $4E9\text{ ml}^{-1}$, a temperature peak of 50 °C is achieved after 30s of illumination. The peak climbs to illumination and 59 °C after 90s of exposure. However, the diameter of the region in which the temperature is above 47 °C actually shrinks slightly when compared to the $2E9\text{ ml}^{-1}$ concentration.

Figure 3.6 presents the temperature distribution along the radius in the $z = 0$ plane within the brain phantom. A trend similar to that shown in Fig.3.5 is seen.

Without nanoshells, the temperature peak remains below $50\text{ }^{\circ}\text{C}$ after 90 s of illumination. When the incubated nanoshell concentration is $2E9\text{ ml}^{-1}$, tissues can be heated up to be above $55\text{ }^{\circ}\text{C}$ in 60 s and after 90 s of exposure, the diameter of the region above $47\text{ }^{\circ}\text{C}$ is as large as 10 mm . Increasing nanoshell concentrations further to $4E9\text{ ml}^{-1}$ helps very little promoting the hyperthermia. The temperature peak increases from 2 to $3\text{ }^{\circ}\text{C}$, while the size of the “hot” region shrinks by approximately 1.5 mm .

Figure 3.7 presents the temperature distribution along the radius in the $z = 0$ plane of the breast cylinder. Unlike the prostate and brain tissue, the desired hyperthermia cannot be achieved in the breast phantom under the present treatment conditions since the temperature peak climbs to only $47\text{ }^{\circ}\text{C}$, even after 90 s of irradiance with an incubated nanoshell concentration as high as $4E9\text{ ml}^{-1}$. To achieve the desired hyperthermia for this tissue phantom, alternatives include using a higher laser power, using a different laser wavelength, extending the irradiance time, and increasing the concentration of photothermal agents, must be explored.

Figure 3.8 presents temperature contours in half of the phantoms of human prostate, brain, and breast, after 90 s of illumination and a nanoshell concentration of $4E9\text{ ml}^{-1}$. The temperature distributions in the human prostate (Fig. 3.8) and brain phantom (Fig.3.10) are very similar despite the difference in the optical properties of host tissues and nanoparticles incubated as photothermal agents. However, Fig. 3.9 shows that the induced hyperthermia is much weaker in the breast phantom.

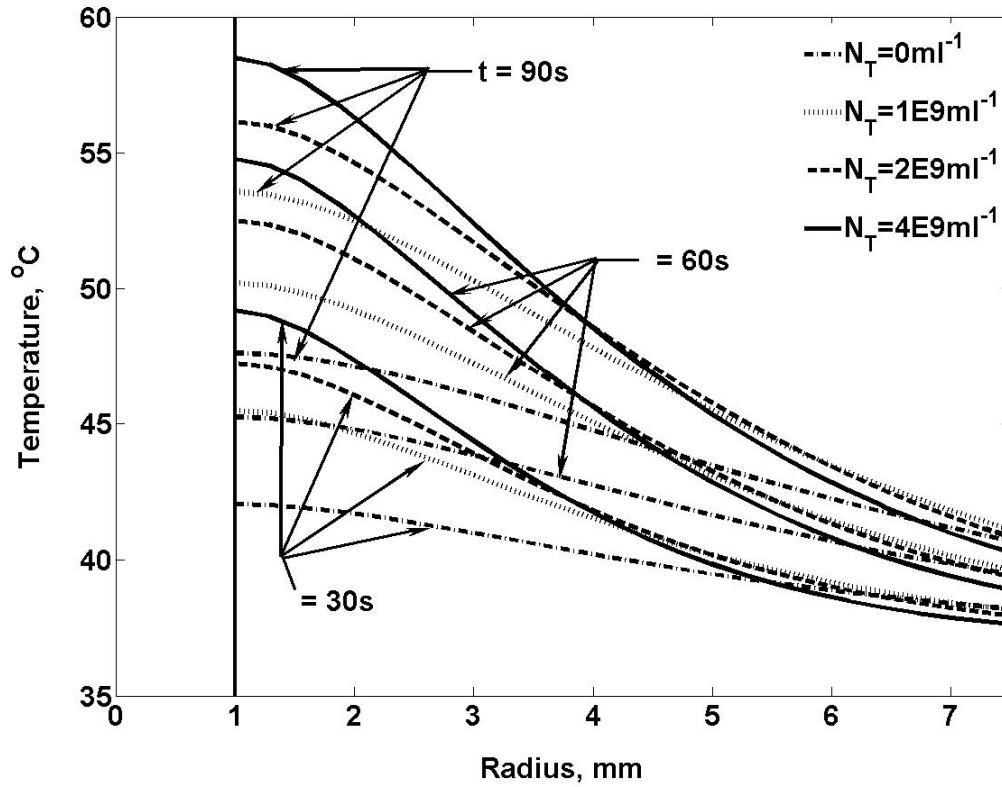


FIGURE 3.5: Transitions of temperature distributions along the radius in the $z = 0$ plane in the human prostate phantom

3.4 Conclusions

In this chapter, the novel nanoparticle-assisted LITT for tumor/cancer treatments process was numerically investigated, with the goal of accumulating knowledge and deepening the understanding of this novel therapy. The whole numerical simulation has been handled as a two-staged procedure, optical modeling and thermal modeling. Detailed physical and mathematical models have been used for both stages and the solutions were approximated by the finite volume technique.

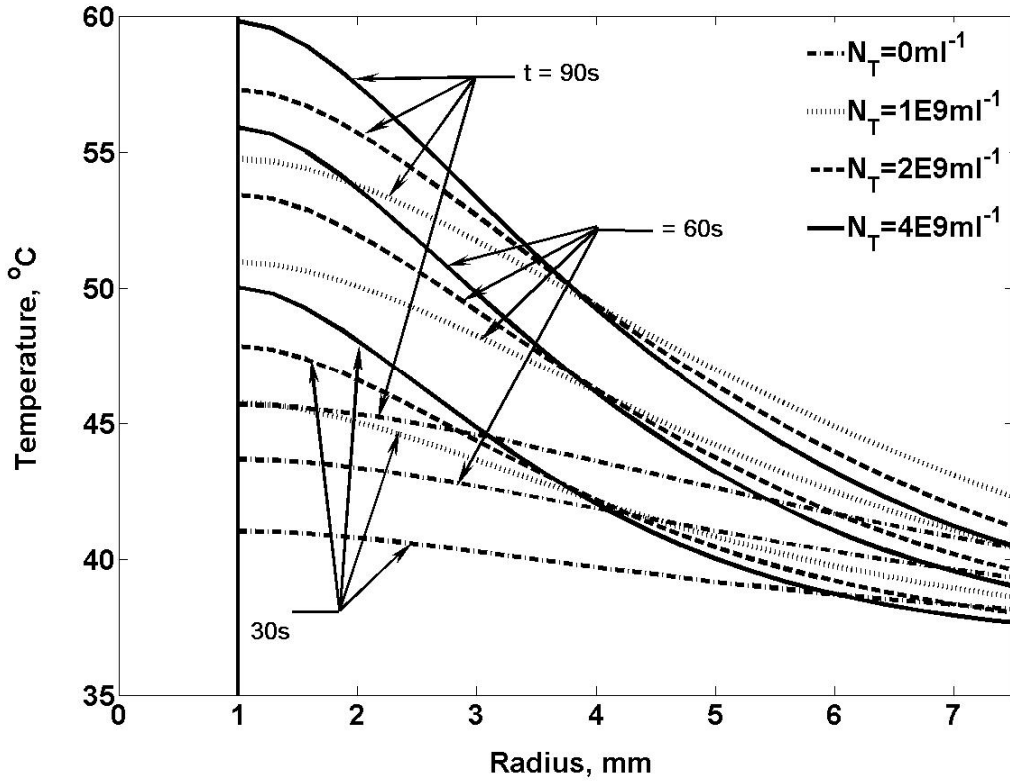


FIGURE 3.6: Transitions of temperature distributions along the radius in the $z = 0$ plane in the human brain phantom

In the investigation of the interactions among treatment conditions, numerical simulations have been produced and results have been presented and analyzed. Based on our results, the following conclusions were drawn:

- 1) Incubated nanoparticles prevent laser light from both diffusing out and propagating deep into the tissue; the higher the nanoparticle concentration, the more

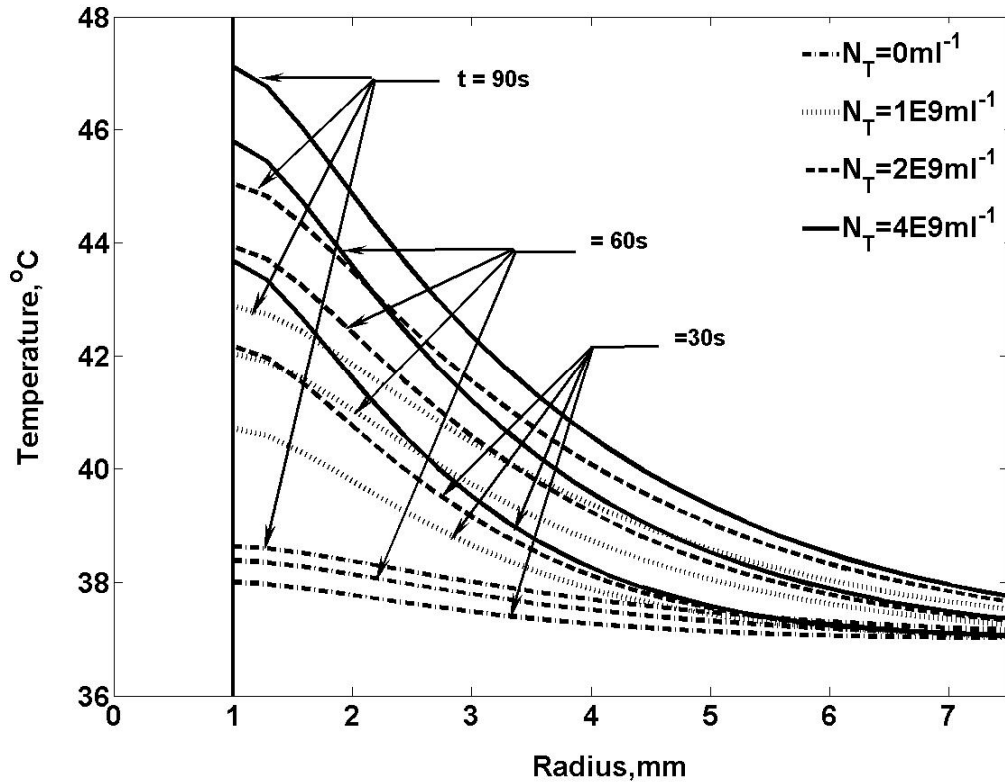


FIGURE 3.7: Transitions of temperature distributions along the radius in the $z = 0$ plane in the human breast phantom

significant this effect is. This presents a challenge to deliver laser doses to the targeted site effectively and is worthy of more study;

2) Nanoparticles that are preferentially absorbing would enhance the local transduction from photon energy to thermal energy. The enhancement in local absorption of photon energy is so significant that inefficient fluence rates will be balanced out. For all the situations investigated in this study, bioheat generation has been greatly enhanced by using nanoparticles as the photo-thermal agent;

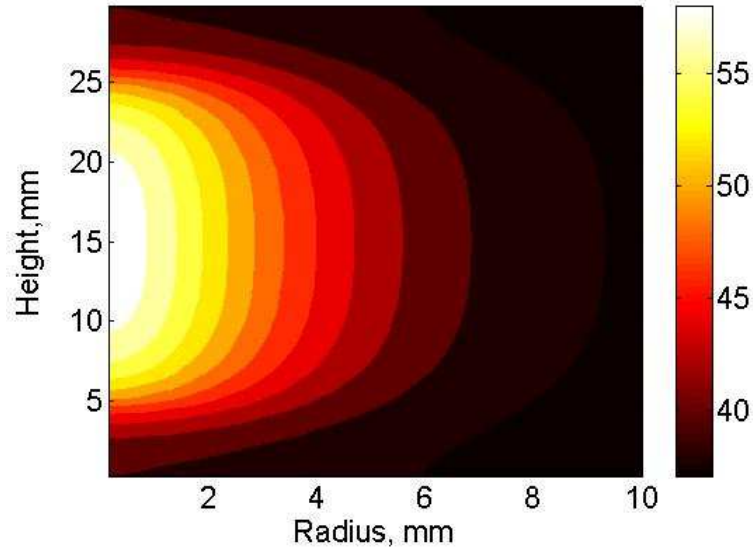


FIGURE 3.8: Temperature distribution after 90s of illumination in half of the human prostate phantom (nanoshell concentration is $4E9ml^{-1}$)

3) The use of a moderate amount of nanoparticles as photothermal agents promotes hyperthermia in that it allows heating the targeted tissue to the desired temperature range in a short period of time. Our simulations indicate that this cannot be achieved without using nanoparticles, although the other conditions are the same. However, with constant illumination, an increase in nanoparticle concentration beyond a certain range has an insignificant impact on hyperthermia. It is believed that this work will help determine an optimal level of concentration of photothermal agents in future therapy.

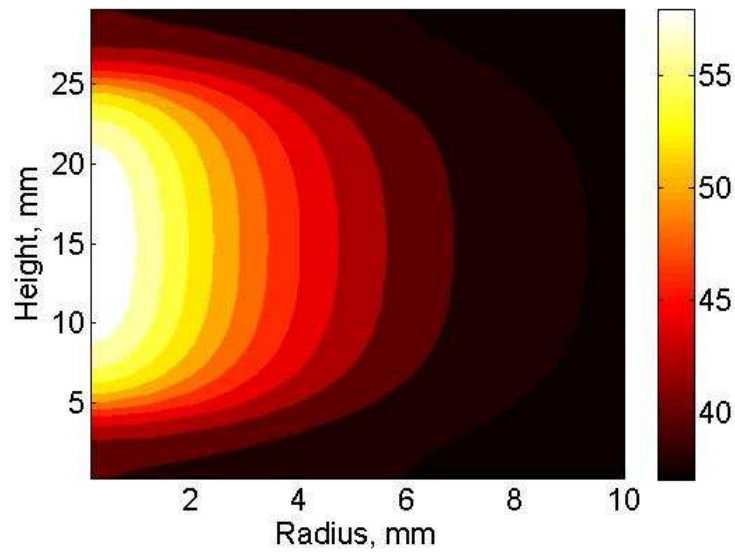


FIGURE 3.9: Temperature distribution after 90s of illumination in half of the human brain phantom (nanoshell concentration is $4E9ml^{-1}$)

3.5 Remarks

This chapter is adapted from:

X. Xu, A. Meade, Jr. and Y. Bayazitoglu, “Numerical Investigation of Nanoparticle Assisted Laser-induced Interstitial Thermo-therapy for Tumor and Cancer Treatments,” *Lasers in Medical Science*, 26(2), 213-222, 2011.

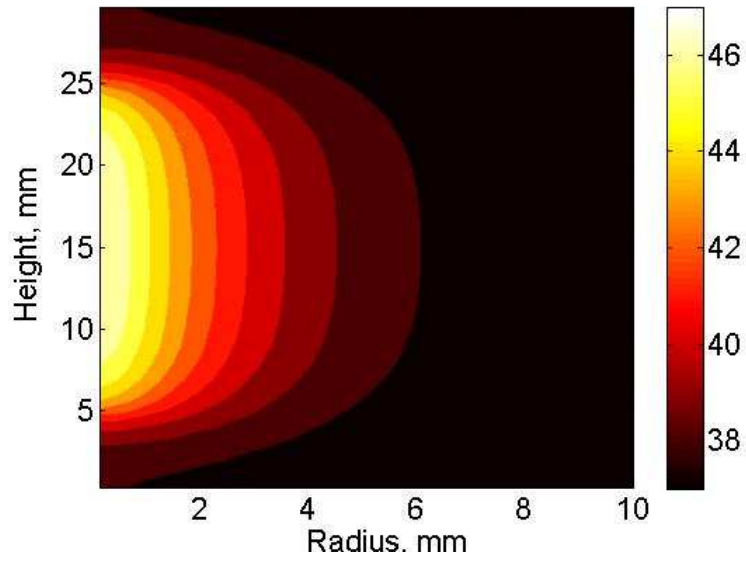


FIGURE 3.10: Temperature distribution after 90s of illumination in half of the human breast phantom (nanoshell concentration is $4E9ml^{-1}$)

Bibliography

- [1] Chen WR, Adams RL, Higgins AK, Bartels KE and Nordquist RE(1996) “Photothermal effects on murine mammary tumors using indocyanine green and an 808-nm diode laser: an in vivo efficacy study”, *Cancer letters* 98(2):169-173.
- [2] Pitsillides CM, Joe EK, Wei X, Anderson RR and Lin CP(2003) “Selective cell targeting with light-absorbing microparticles and nanoparticles”, *Biophysical Journal* 84: 4023-4032.
- [3] Zharov VP, Galitovsky V and Viegas M(2003) “Photothermal detection of local thermal effects during selective nanophoto-thermolysis with nanoparticles”, *Applied physics letter* 83(24): 4897-4899.
- [4] Hainfeld JF, Slatkin DN and Smilowitz HM(2004) “The use of gold nanoparticles to enhance radiotherapy in mice”, *Physics in Medicine and Biology* 49: 309-315.
- [5] Huff TB, Tong L, Zhao Y, Hansen MN, Cheng JX and Wei A (2007) “Hyperthermia effects of gold nanorods on tumor cells”, *Nanomedicine* 2(1): 125-132.
- [6] Takahashi H, Niidome T, Nariai A, Niidome Y and Yamada S (2006) “Photothermal reshaping of gold nanorods prevents further cell death”, *Nanotechnology* 17: 4431-4435.
- [7] Huang X, El-Sayed IH, Qian W and El-Sayed MA (2006) “Cancer cell imaging

- and photothermal therapy in the near-infrared region by using gold nanorods”, *Journal of the American Chemical Society* 128(6): 2115-2120.
- [8] Hirsch LR, Stafford RJ, Bankson JA, Sershen SR, Rivera B, Price RE, Hazle JD, Halas NJ and West JL(2003) “Nanoshell-mediated near-infrared thermal therapy of tumors under magnetic resonance guidance”, *Proceeding of National Academy of Science* 100(23): 13549-13554.
- [9] Loo C, Lin A, Hirsch L, Lee M, Barton J, Halas N, West J and Drezek R(2004) “Nanoshell-enabled photonics-based imaging and therapy of cancer”, *Technology in Cancer Research Treatment* 3(1): 33-40.
- [10] O’Neal DP, Hirsch LR and Halas NJ (2004) “Photo-thermal tumor ablation in mice using near infrared-absorbing nanoparticles”, *Cancer letters* 209(2):171-176.
- [11] Loo C, Lowery A, Halas NJ, West JL and Drezek R(2005) “Immunotargeted nanoshells for integrated cancer imaging and therapy”, *Nano Lett* 5: 709-711.
- [12] Shi Kam NW, O’Connell M, Wisdom JA and Dai H(2005) “Carbon nanotubes as multifunctional biological transporters and near-infrared agents for selective cancer cell destruction”, *Proceeding of National Academy of Science* 102(33): 11600-11605.
- [13] Chen J, Wiley B, Li ZY, Campbell D, Saeki F, Cang H, Au L, Lee J, Li X and Xie Y(2005) “Gold nanocages: engineering their structure for biomedical applications”, *Advanced Materials* 17: 2255-2261.
- [14] Hu M, Petrova H, Chen J, McLellan JM, Siekkinen AR, Marquez M, Li X, Xia Y and Hartland GV (2006) “Ultrafast laser studies of the photothermal properties of gold nanocages”, *Journal of physical chemistry B* 110(4): 1520-1524.
- [15] Connor EE, Mwamuka J, Gole A, Murphy CJ and Wyatt MD (2005) “Gold

- nanoparticles are taken up by human cells but do not cause acute cytotoxicity”, *Small* 1: 325-327.
- [16] Khan JA, Pillai B, Das TK, Singh Y and Maiti S (2007) “Molecular effects of uptake of gold nanoparticles in HeLa cells”, *Chembiochem* 8: 1237-1240.
- [17] Shukla R, Bansal V, Chaudhary M, Basu A, Bhonde RR and Sastry M (2005) “Biocompatibility of gold nanoparticles and their endocytotic fate inside the cellular compartment: a microscopic overview”, *Langmuir* 21: 10644-10654.
- [18] Katz E and Willner I (2004) “Integrated nanoparticle biomolecule hybrid systems: synthesis, properties, and applications”, *Angewandte Chemie International Edition* 43: 6042-6108.
- [19] Xu X, Meade, A, Bayazitoglu Y (2010) “Fluence rate distribution in laser-induced interstitial thermotherapy by meshfree collocation”, *International Journal of Heat and Mass Transfer* 53: 40174022.
- [20] Feng Y, Rylander MN, Bass J, Oden JT and Diller K (2005) “Optimal design of laser surgery for cancer treatment through nanoparticle-mediated hyperthermia therapy”, *NSTI-Nanotech* 1: 39-42.
- [21] Feng Y, Fuentes D, Hawkins A, Bass J, Rylander MN, Eillot A, Shetty A, Stafford RJ and Oden JT (2009) “Nanoshell-mediated laser surgery simulation for prostate cancer treatment”, *Engineering with Computers* 25 : 3-13.
- [22] Tjahjono I. and Bayazitoglu Y (2008) “Near-Infrared light heating of a slab by embedded nanoparticles”, *International Journal of Heat and Mass Transfer* 51:1505-1515.
- [23] Bayazitoglu Y(2009) “Nanoshell Assisted Cancer Thermal Theraphy: Numerical

Simulations”, *Proceedings of the 2nd ASME Micro/Nanoscale Heat Mass Transfer: An International Conference, Shanghai*.

- [24] Jacques SG, Chandrasekar S(1990) “Radiative transfer”, Oxford university press, London, England.
- [25] Ishimaru A(1978) “Wave propagation and scattering in random medium”, Academic Press, New York.
- [26] Prashant KJ, Lee KS, El-Sayed IH and El-Sayed MA (2006) “Calculated absorption and scattering properties of gold nanoparticles of different size, shape and composition: applications in biological imaging and biomedicine”, *Journal of physical chemistry B* 110: 7238-7248.
- [27] Link S and El-Sayed MA(2003) “Optical properties and ultrafast dynamics of metallic nanocrystals”, *Annual Review of Physical Chemistry* 54: 331-366.
- [28] Mie G (1908) “Beitrge zur Optik trber Medien, speziell kolloidaler Metallsungen. Leipzig”, *Annals of Physics* 330: 377445.
- [29] Vera J and Bayazitoglu Y(2009)“Gold nanoshell density variation with laser power for induced hyperthermia”,*Int. J. Heat Mass Transfer* 52: 564-573.
- [30] Vera J and Bayazitoglu Y(2009)“A note on laser penetration in nanoshell deposited tissue”, *International Journal of Heat Mass Transfer* 52(13/14): 3402-3406.

Feasibility of selective nanoparticle-assisted photothermal treatment for an embedded liver tumor

4.1 Introduction

Up to now, almost all reported in vivo studies of nanoparticle- assisted photothermal therapy (PPTT) were conducted on subcutaneous tumors growing immediately below the skin of live animals (1; 2; 3; 4). For subcutaneous tumors, types of mechanisms can induce nanoparticles to bypass the tumors surrounding medium and preferentially accumulate inside at them. This phenomenon is usually referred to as the nano- particles selective tumor targeting. Among all the mechanisms, the most fundamental one is passive accumulation, which is caused by enhanced permeability and retention effect (ERP). In 1986, ERP was firstly defined by H. Maeda (5) and has been studied intensely (6; 7; 8; 9) ever since.

Although the feasibility of PPTT on subcutaneous tumors has been repeatedly confirmed (1; 2; 3; 4; 13) , whether this novel therapy could be pushed further

to treat organ tumors remains scantily explored. One opinion that popularly exists among the bio-nano community is that although nanoparticles could intelligently discriminate a subcutaneous tumor from its surrounding medium, their ability of discriminating an organ tumor from the surrounding healthy organ tissues is weaker. Noticeably, many nanoparticles would be retained by the health organ tissues that surround organ tumors, failing to reach the targeted tumors.

This preceding opinion has been confirmed by many *in vivo* nanoparticle bio-distribution studies (1; 4; 10; 11). In a publication which recently appeared, Goodrich et al. (1) reported that 17 hours after injecting a dose of 14×45 nm gold nanorods (14 nm in radius and 45 nm in length) to the tail veins of live mice, around 71 percentage of the total injected nanorod dose accumulated in the liver organ, about 4% of the dose accumulated in the spleen, and about 1 percentage of the injected dose was found in the kidney and lymph nodes. No substantial amount of nanorods had been found in other tissue structures and organs, including bones, lung, kidney, and muscles. In another publication, Li et al. (2) reported that 4 hours after injecting a dose of gold nanoshells with a mean diameter of 43.5 ± 2.3 nm and a mean shell thickness of 34 nm to the tail vein of live mice, about 9.2% of the whole injected nanoparticle dose was found in the clearance organ liver, while about 5% of the dose was found in the spleen. The kidney and lung tissues retained 12% and 8% of the whole dose, respectively. In theory, the loss of nanoparticles to the untargeted tissue medium is very unfavorable for PPTT procedures. A direct consequence might be that the “selectivity” of the therapy, which is the advantage being boasted of PPTT over conventional photothermal therapy (PTT), would be impaired. Since systematic experimental studies of extending PPTT to treat organ tumor are still pending, the present investigation was therefore devoted to numerically explore such possibilities, focusing on the investigation of the achievability

of “selective” therapeutic effects when nanoparticles tumor recognition is relative low. The fundamental assumption that the surrounding medium of tumors is clean of nanoparticles, which has been adopted by almost all published PPTT numerical simulations (12; 14; 18; 19; 20; 21; 22; 23; 24), was discarded. Different situations of nanoparticles low discrimination between the organ tumor and its surrounding medium were instead modeled. Particularly, the embedded liver tumor was our research interest here because as the clearance organ, liver tissues have uniquely strong retention ability to nanoparticles (1; 4). Consequently, treating liver tumors would be particular challenging for PPTT.

4.2 Mathematical and computational models

The simulation of PPTT procedures can be divided into two stages (18; 19; 20; 21; 22; 23; 24), similar as that of PTT procedures (25; 26). The first stage is optical simulation, simulating laser light transportations within the biology tissues. The transportation of laser lights could be described using the radiant transport equation (RTE). Depending on whether a pulsed laser or a continuous wave laser is used as the irradiance source, the RTE could either be of the transient form or of the steady form. The numerical goal for this stage is to approximate the distribution of fluence rate. The second stage is thermal simulation, simulating the thermal responses of the biology tissues to the laser exposure. Thermal simulation is governed by the bio-heat equation (14; 18; 19; 20; 21; 22; 23). The present study adopted the finite volume method (FVM) for both the optical and bio-heat simulation. The method was previously used for laser therapy modeling and was validated against the Monte Carlo simulation and another numerical technique, namely, the meshfree collocation. Related details could be found in the (27). The same method with necessary modifications has also been used in another PPTT study and related details could be found in (15).

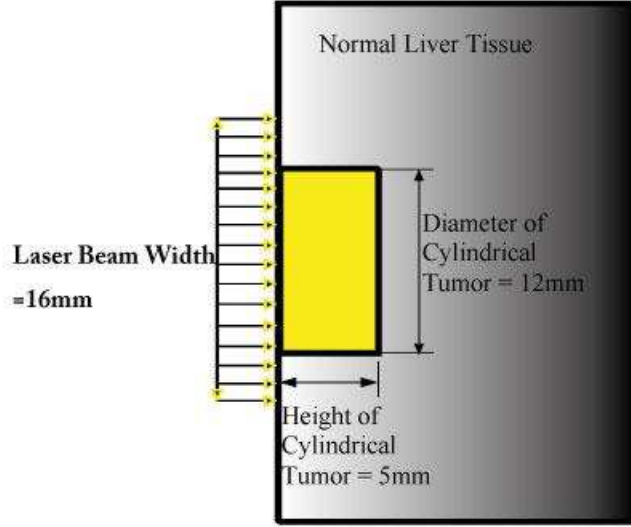


FIGURE 4.1: The layout of the PPTT experiment (not up to scale)

Table 4.1: Optical properties for the liver tumor and normal liver tissues

Tissue type	$\lambda(nm)$	$k_{\lambda}(mm^{-1})$	$k_s(mm^{-1})$	g	$k_s'(mm^{-1})$	δ
Liver tumor	633	0.14	28.0	0.9426	1.51	1.20
Normal liver	633	0.38	28.0	0.952	1.34	0.72

The experiment design for the simulation is presented in Fig. 4.1. The same experiment design has been used by M. Jode (28) to investigate the selectivity of photodynamic therapy (PDT). The optical properties of tumor tissues and normal liver tissues (listed in Table 1) are also found in the same reference. In Fig. 4.1, the liver tumor was of the shape of a cylinder and was superficially embedded. Except for the top surface, it was surrounded fully by normal liver tissues. The diameter

of the tumor was 12 mm and the height was 5mm. A 16mm wide laser beam was applied from the outside of the tumor to irradiate it. The beam of laser lights was emitted from a 633-nm heliumneon laser and the intensity of the laser beam was $1 W/cm^2$. Based on our previous experiences with PPTT tumor treatments (15), laser irradiance with such an intensity should be strong enough to induce effective hyperthermia. It could be computed that the volume of the tumor was about $565 mm^3$. Tumors of such a size are on the small side for the surgery treatment to be performed very accurately, especially when they fatally grow on the organ liver. Therefore, treatments such as PPTT and PDT might be more favorable. After laser lights propagate into the tissue, the lights are absorbed and diffused out by the tissue. The radiant intensity $L(\mathbf{r}, \mathbf{s})$ within the tissues therefore is comprised with two parts: (1) the remnant of collimation $L_c(\mathbf{r}, \mathbf{s})$ and (2) the induced diffusion radiant intensity $L_d(\mathbf{r}, \mathbf{s})$:

$$L(\mathbf{r}, \mathbf{s}) = L_c(\mathbf{r}, \mathbf{s}) + L_d(\mathbf{r}, \mathbf{s}) \quad (4.1)$$

According to Beers law, $L_c(\mathbf{r}, \mathbf{s})$ could be expressed as the decay of collimation ϕ_0 :

$$L_c = \phi_0 \exp(-(k_\alpha(\mathbf{r}) + k_s(\mathbf{r}))z) \delta(\mathbf{s} - \mathbf{s}_c) \quad (4.2)$$

where z indicates the penetration depth of the laser, \mathbf{s}_c indicates the propagating direction of collimation, ϕ_0 indicates the total laser radiant flux, and $k_\alpha(\mathbf{r})$ and $k_s(\mathbf{r})$ are the local absorption and scattering coefficient, respectively.

The transportation of the diffusion radiant intensity $L_d(\mathbf{r}, \mathbf{s})$ within the tissue medium is governed by the RTE:

$$\frac{\partial L_d(\mathbf{r}, \mathbf{s}, t)}{\partial t} + \frac{\partial L_d(\mathbf{r}, \mathbf{s}, t)}{\partial \mathbf{s}} + (k_\alpha(\mathbf{r}) + k_s(\mathbf{r}))L_d(\mathbf{r}, \mathbf{s}) = \frac{k_s(\mathbf{r})}{4\pi} \int_{4\pi} \Phi(\mathbf{s}, \mathbf{s}')L_d(\mathbf{r}, \mathbf{s}', t)d\omega' + S_c(\mathbf{r}, \mathbf{s}, t) \quad (4.3)$$

Since a continuous waved laser is used as the irradiance, the first term in Eq. 4.3 could be eliminated. In Eq. 4.3, $\mathbf{r} = (r, z)$ is the position vector, \mathbf{s} is the direction vector, $\Phi(\mathbf{s}, \mathbf{s}')$ represents the scattering phase function, and $S_c(\mathbf{r}, \mathbf{s})$ indicates the source term induced by collimation:

$$S_c(\mathbf{r}, \mathbf{s}) = \frac{k_s(\mathbf{r})}{4\pi} \int_{4\pi} \Phi(\mathbf{s}, \mathbf{s}')L_c(\mathbf{r}, \mathbf{s}')d\omega' \quad (4.4)$$

In Eqs. 4.24.4, the absorption coefficient $k_\alpha(\mathbf{r})$ and the scattering coefficient $k_s(\mathbf{r})$ are overall parameters that count contributions from both the host tissue and embedded nanoparticles (18; 19; 20; 21; 22; 23; 15):

$$k_\alpha(\mathbf{r}) = k_{\alpha,np}(\mathbf{r}) + k_{\alpha,t}(\mathbf{r}) \quad (4.5)$$

$$k_s(\mathbf{r}) = k_{s,np}(\mathbf{r}) + k_{s,t}(\mathbf{r}) \quad (4.6)$$

where the subscript “t” indicates that the corresponding optical properties are for tissues while the subscript “np” indicates that the corresponding optical properties are for nanoparticles.

The boundary condition for Eq. 4.3 is tentative. If there is any collimation light entering from the location \mathbf{r}_b , the boundary condition is:

$$L_d(\mathbf{r}_b, \mathbf{s}) = (1 - R_{sp})\phi_0\delta[\mathbf{s} - \mathbf{s}_c] + \frac{R_d}{\pi} \int_{\mathbf{n} \cdot \mathbf{s}' < 0} L_d(\mathbf{r}_b, \mathbf{s}') |\mathbf{n} \cdot \mathbf{s}'| d\omega' \quad (4.7)$$

otherwise,

$$L_d(\mathbf{r}_b, \mathbf{s}) = \frac{R_d}{\pi} \int_{\mathbf{n} \cdot \mathbf{s}' < 0} L_d(\mathbf{r}_b, \mathbf{s}') |\mathbf{n} \cdot \mathbf{s}'| d\omega' \quad (4.8)$$

where R_{sp} indicates Fresnel specular reflection and R_d indicates the internal reflectivity of local medium.

While Eq. 4.2 gives a direct solution to $L_c(\mathbf{r}, \mathbf{s})$, $L_d(\mathbf{r}, \mathbf{s})$ could be approached by numerically solving Eqs.4.3 and 4.4 and Eqs. 4.7 and 4.8 using FVM.

Many different nanostructures have been tested for PPTT, including nanospheres (2), nanorods (1; 31; 32), nanoshells (33; 34; 35; 36; 3), carbon nanotubes (37), and nanocages (38; 39). Among them, goldsilica nanoshells and gold nanorods are particularly promising mainly because their plasmon resonance could be easily tuned to be located in the near-infrared spectrum and their plasmonic resonance could be tuned to be four to five orders higher than that of organ dyes (30; 40), which were used as photo-thermal agent prior to nanoparticles. Other merits of goldsilica nanoshells and gold nanorods include low toxicity (41; 42), less photobleaching, and multifunctionality (32?) such as playing the dual roles of the photothermal agent and the optical contrast agent.

The goldsilica nanoshell is adopted as the photothermal agent for PPTT procedures. The silica core of the nanoshell has a radius of 16 nm, and the gold shell thickness is 5nm. In the following text, this type of nano-shell would be referred to as the $R[16, 21]nm$ nanoshell. Therapeutic performances of the $R[16, 21]nm$ nanoshells as the photothermal agent have previously been investigated in studies (15; 18; 19).

Based on the Mie calculation (29), the $R[16, 21]nm$ nanoshells are preferentially

absorbing, with the absorption cross-section C_{abs} ($4.7822E - 14 m^2$) being almost two orders higher in magnitude than its scattering cross-section C_{sca} ($7.47314E - 16 m^2$). Also, the plasmonic resonance peak of the $R[16, 21]nm$ nanoshell appears at the wavelength of $631nm$, matching perfectly with the wavelength of the laser irradiance.

The absorption and scattering coefficients $k_{\alpha,np}$ and $k_{s,np}$ could be quantified in terms of the absorption efficiency Q_{abs} and scattering efficiency Q_{sca} (18; 19; 20; 21; 22; 15):

$$k_{\alpha,np} = \pi r_0^2 Q_{abs} N_T \quad (4.9)$$

$$k_{s,np} = \pi r_0^2 Q_{sca} N_T \quad (4.10)$$

N_T in Eq. 4.9 is the number of nanoparticles per unit volume (in other terms, concentration); for spherical structures such as nanoshells, r_0 is the core radius; and for other non-spherical structures, r_0 should be the effective radius. The absorption efficiency Q_{abs} and the scattering efficiency Q_{sca} were evaluated using Mie series (29; 30).

In order to simulate different discriminations of nano-shells for the liver tumor and normal liver tissues, values of nanoshell retention ratio (which is defined as the nanoshell concentration in the targeted tumor versus the nanoshell concentration in the normal tissue) have been varied from 0 : 0 (corresponding to the situation of conventional PTT, no photothermal agents used) to 1/1, 2/1, 4/1, and eventually to 8/1. Here “1” corresponds to a concentration of $1E16 shells/m^3$. The higher the nanoshell retention value, the better nanoshells recognize the liver tumor from the surrounding medium.

Solving Eq. 4.2 to get $L_c(\mathbf{r}, \mathbf{s})$ and solving Eqs. 4.3 and Eqs.4.7 to get $L_d(\mathbf{r}, \mathbf{s})$, then the fluence rate $\Psi(\mathbf{r})$ can then be computed by integrating the radiant intensity $L(\mathbf{r}, \mathbf{s})$ over the solid angle space:

$$\Psi(\mathbf{r}) = \int_{4\pi} L(\mathbf{r}, \mathbf{s}) = \int_{4\pi} [L_c(\mathbf{r}, \mathbf{s}) + L_d(\mathbf{r}, \mathbf{s})]d\omega' \quad (4.11)$$

Further, the transduction from the photon energy to thermal heat could be evaluated as:

$$Q_s(\mathbf{r}) = k_\alpha(\mathbf{r})\Psi(\mathbf{r}) \quad (4.12)$$

$Q_s(\mathbf{r})$ will appear as the source term in the bio-heat transportation equation.

When exposed to laser irradiance, the embedded nano- shells work point-wisely as photon absorbers, converting the photon energy into thermal heat within hundreds of picoseconds and dissipating the generated thermal heat out to their surrounding medium (12; 14). The time scale of thermal heat generation is many orders smaller in magnitude compared to the time scale of thermal heat transportation within the biology tissues, which is controlled by the thermal conductivity of the tissue medium. Therefore, time elapses for the thermal heat generation can be neglected.

Under the cylindrical coordinate system, the heat transportation equation is:

$$\rho c \frac{\partial T(\mathbf{r}, t)}{\partial t} = \frac{1}{r} \frac{\partial}{\partial r} (rk \frac{\partial T(\mathbf{r}, t)}{\partial z}) + \frac{\partial}{\partial z} (k \frac{\partial T(\mathbf{r}, t)}{\partial z}) - v_B(T(r, t) - T_{Arterial}) + Q_s(\mathbf{r}, t) \quad (4.13)$$

Where t indicates the time, ρ indicates the density of the medium, c indicates the specific heat of the medium, T corresponds to the temperature, k is the thermal

conductivity of the medium, and v_B is the blood perfusion rate. According to (16), for both the tumor and healthy liver tissues, the density ρ is $1,090 \text{ kg/m}^3$, and the heat conductivity k is 0.45 W/mK . The specific heat c is $3,400 \text{ J/kgK}$ for liver tumor and $3,370 \text{ J/kgK}$ for the healthy liver tissues.

For the layout depicted in Fig. 4.1, the thermal boundary condition could be described as:

$$k \frac{\partial T}{\partial z} \Big|_{z=0} = h(T - T_\infty) \quad (4.14)$$

Where h represents the convection coefficient and T_∞ represents the environment temperature and was set to be $25 \text{ }^\circ\text{C}$.

4.3 Results and discussion

Based on the mathematical models described in an earlier section, numerical simulations have been run to model the therapeutic effects of the experiment. Results of the fluence rate distribution, the conversion from photon energy to thermal heat, and the distribution of hyperthermia temperature within the study object are presented and discussed in this section.

The optical penetration depth (δ) is an important factor to judge a laser delivery procedure. It also provides important information to predict the inducible hyperthermia. Approximately, for turbid tissue medium, δ could be calculated as $\delta = \frac{1}{3[k_\alpha + k_s(1-g)]}$. For the wavelength of 633 nm , the liver tumor has an absorption coefficient of 0.14 mm^{-1} , a scattering coefficient of 28.0 mm^{-1} , and an anisotropy factor of 0.946 (28); is therefore computed to be 1.2 mm . For the same wavelength, the absorption, scattering coefficient, and anisotropy factor for the healthy liver tis-

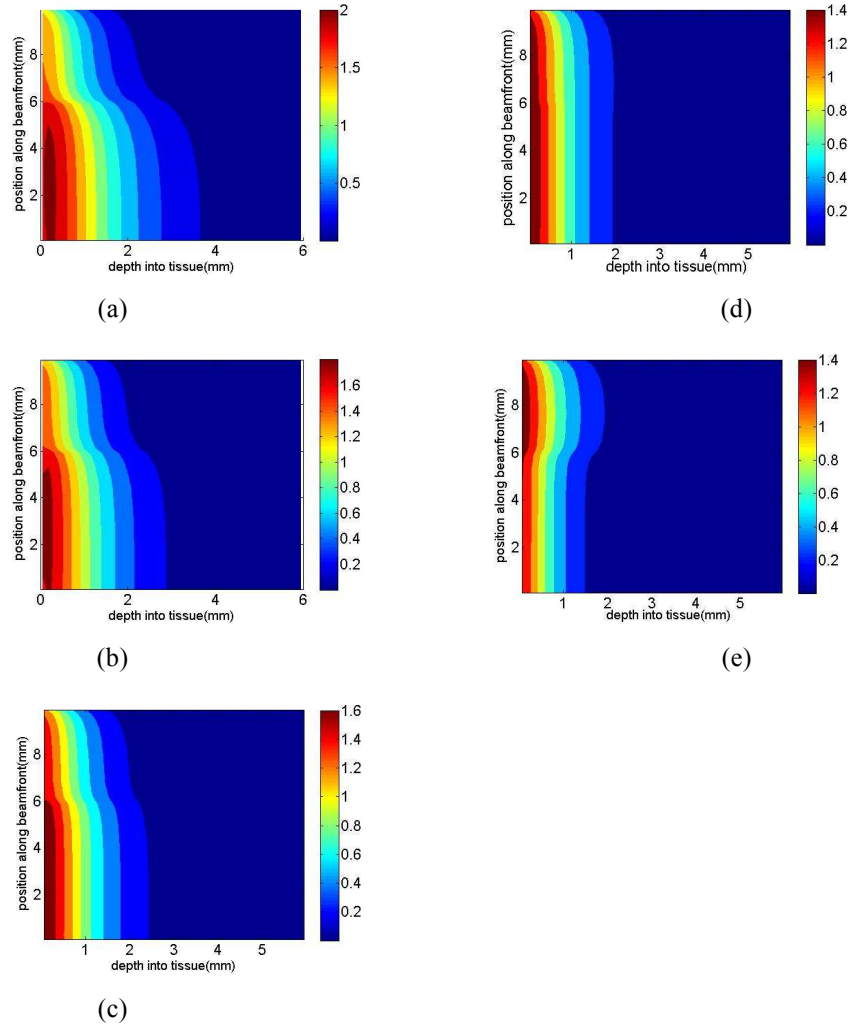


FIGURE 4.2: The distribution of the fluence rate (W/cm^2) within the study object (the liver tumor and surrounding normal liver tissues) when a the retention ratio = $0 : 0$, b the retention ratio = $1/1$, c the retention ratio = $2/1$, d the retention ratio = $4/1$, e the retention ratio = $8/1$

sue are 0.38 mm^{-1} , 28.0 mm^{-1} , and 0.952 , respectively (28). It could be computed that δ for the healthy liver tissue is 0.72 mm . It is noticed that because of differences in optical properties, δ for the liver tumor is almost twice that for the normal liver tissues, which is therapeutically favorable.

The destruction depth of the exposed tissues nonlinearly depends on the laser penetration depth δ , the fluence rate distribution (which is also related to δ), the concentration of embedded nanoparticles, and laser exposure time. Typically, the tissue destruction depth could be four to five times larger than the optical penetration depth δ (17). Since the embedded nanoparticles usually impose extra resistances for laser lights to penetrate deeper, PPTT is more demanding for good laser delivery techniques compared to PTT.

The transitions of fluence rate distribution with the nano-shell retention ratio are presented in Fig.4.2. Because of the symmetrical characteristics of the present problem, only half of the geometry is shown. Figure 4.2a corresponds to the situation when retention ratio was $0 : 0$. According to Fig.4.2a, if no nanoshells were used, laser lights (in terms of fluence rate) decayed more rapidly in the normal liver tissue than they did in the liver tumor. The differences in the optical decay rates within the two tissues lead to significant distortions of the iso-fluence rate curves at the junction of the two tissues, the position of which was $r_0 = 6 \text{ mm}$

Figure 4.2b presents the laser light distribution when the nanoshell retention ratio was $1 : 1$, implying that nanoshells did not recognize the liver tumor from the normal tissues at all. Figure 4.2b indicates that under this situation, the reduction of δ is less significant for the normal liver tissue. The analyzed reason is: compared to the normal liver tissue, the liver tumor has a smaller absorption coefficient; therefore,

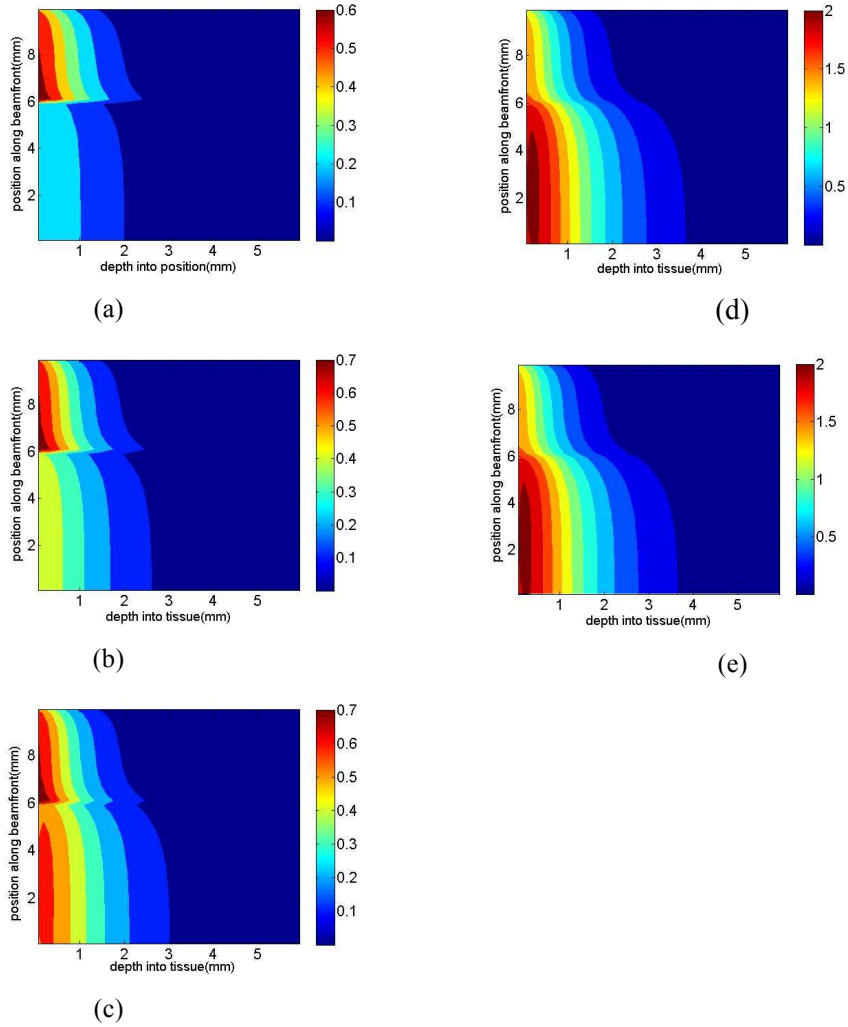


FIGURE 4.3: The distribution of the thermal heat generation (W/cm^2) within the study object (the tumor and surrounding normal liver tissues) when a the retention ratio = $0 : 0$, b the retention ratio = $1/1$, c the retention ratio = $2/1$, d the retention ratio = $4/1$, e the retention ratio = $8/1$

the extra absorption introduced by nanoshells has a greater affect on the liver tumor. Because of the differences of nanoshell impact on the two tissues, distortions of the iso- fluence rate contours at the junction have been smoothed out compared to what is presented in Fig. 4.2a.

The nanoshell retention ratio was continuously increased to 2/1, 4/1, and 8/1 to simulate the improving tumor discriminations of nanoshells. The corresponding fluence rate distributions are presented in Fig. 4.2ce, respectively. It can be seen that when the nanoshell retention ratio was 4/1, the distortions of the iso-fluence rate contours on the tissue junction almost disappeared. According to Fig. 4.2d, it looked like the laser lights propagated in one homogeneous medium instead of two different tissues with very different optical properties. When the retention ratio was increased to 8/1, the laser light decayed faster in the liver tumor than in the normal liver tissues. The distortions of iso-fluence rate con- tours that disappeared in the Fig. 4.2d came back, only with the distorted direction changed.

Besides reductions in the penetration depth δ , Fig.4.2ae also shows that the fluence rate peaks dropped consecutively from 2 to 1.4 W/cm^2 with the increasing nanoshell retention ratio. A deep laser penetration and an intensive fluence rate distribution are both therapeutically desired for PPTT. Yet, Fig. 4.2ae shows that both have been impaired because of the embedded nanoshells. Optically, PPTT is in a less favorable position compared to PTT. Is the thermal enhancement induced by nanoshells strong enough to balance out the optical inefficiencies? To answer this question, the conversion from the photon energy to the thermal heat within the study object was evaluated and then the temperature distribution was simulated. Figure 4.3a presents the thermal heat generation when no nanoshells have been used. Figure 4.3a shows that relative to what was in the liver tumor, the conversion from laser

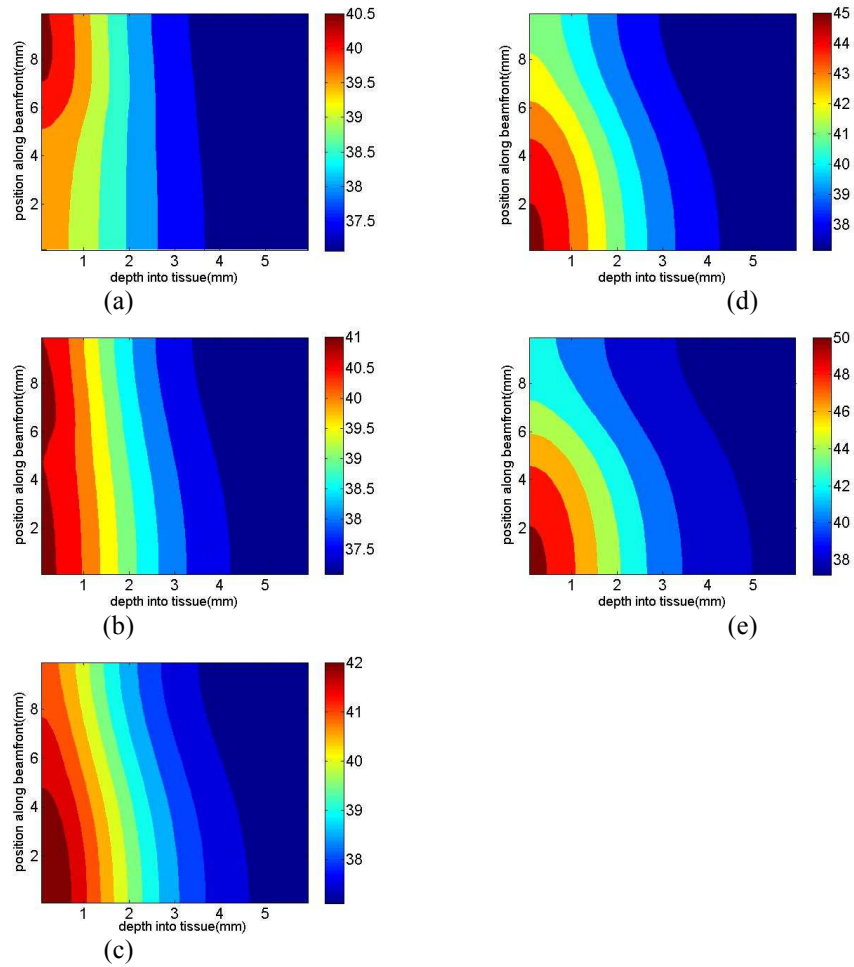


FIGURE 4.4: The temperature field ($^{\circ}\text{C}$) within the study object after 30s of laser exposure when *a* the retention ratio = 0 : 0, *b* the retention ratio = 1/1, *c* the retention ratio = 2/1, *d* the retention ratio = 4/1, *e* the retention ratio = 8/1

photon energy to bio-heat was much more intense in the normal tissues. Therefore, if the irradiance lasts long enough, it is predictable that normal liver tissues will be destroyed before the liver tumor. Therefore, the conventional PTT is not a feasible therapy for the present liver tumor case at 633 *nm*. Even after the nanoshell retention ratio was increased to 2/1 (corresponding to Fig. 4.3c), the thermal heat generation in the normal tissues was still stronger. Only after the nanoshell retention ratio was increased to 4/1 did the thermal heat generation in the tumor start to exceed that in the normal tissues.

PPTT could either work independently as a primary treatment or work as an adjuvant tool for other therapies such as surgery and chemotherapy. When applied as a primary treatment, tumor tissues need to be heated up to a temperature range of 47 to 55 °C. Particularly, if tumor ablation is desired, tumor tissues need to be heated up to be over 55 °C. If PPTT is applied as an adjuvant treatment, a low hyperthermia of 41-43 °C is enough to weaken the tumor cells such that the effectiveness the primary therapy could be significantly enhanced [45]. Whether the targeted tumor could be heated up to the desired temperature immediately is also a very important factor to judge the therapeutic effects.

Figures 4.4 and 4.5 present the temperature fields of the study object after exposure for 30 and 90 s, respectively, corresponding to the different nanoshell retention ratio values. It can be seen that if no nanoshells were used (Figs. 4.4a and 4.5a), after 90 s of laser irradiance, only a narrow banded region in the normal tissue site has been heated up to the temperature 43 °C, while the temperature peak in the tumor is less than 42 °C. Again, the conclusion that conventional PTT is not a feasible therapy for the present liver tumor case at 633 *nm* was confirmed. If nanoshells could not recognize the liver tumor from normal liver tissues (consequently, the re-

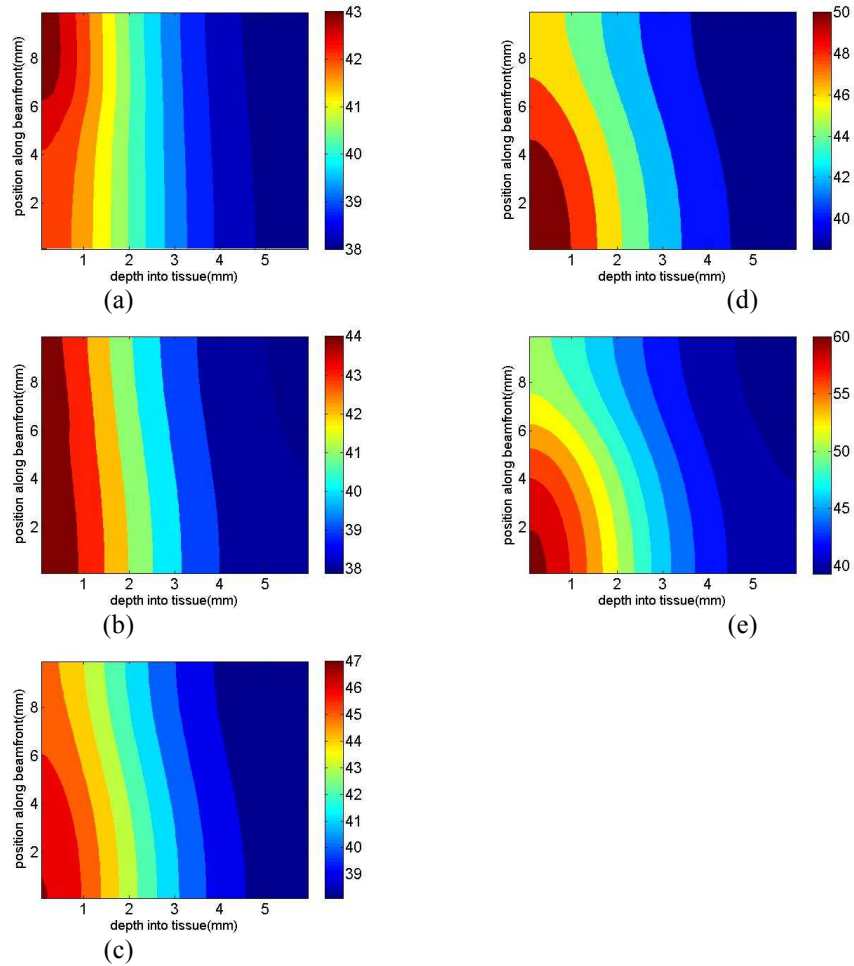


FIGURE 4.5: The temperature field ($^{\circ}\text{C}$) within the study object after 90 s of laser exposure when *a* the retention ratio = 0 : 0, *b* the retention ratio = 1/1, *c* the retention ratio = 2/1, *d* the retention ratio = 4/1, *e* the retention ratio = 8/1

tention ratio is 1 : 1), the laser was non-selective in its thermally induced therapeutic effect. When the nanoshell retention ratio was increased to 2/1, after 90 s of laser irradiance, about one fifth of the entire tumor achieved a temperature that is above 47 °C; meanwhile, the temperature peak in the normal liver tissue was still lower than 43 °C. An increasing nanoshell retention ratio corresponds to a better tumor discrimination of nanoshells. Figures 4.4d and 4.5d shows that when the retention ratio was as high as 4/1, the achieved therapeutic effects were desirable: around one third of the whole tumor was heated up to temperatures above 50 °C, while the temperature peak in the normal tissue was lower than 45 °C, and only a marginal region was heated up to such a temperature. If the retention ratio was increased further to 8/1, after 90 s of exposure (Fig. 4.5e), tumor ablations happened in more than half of the entire tumor. However, a region in the surrounding normal tissue suffered from serious damages as well. As long as being selective is the major focus, the therapeutic effect when the nanoshell retention ratio was 8/1 was not as desirable as that when the retention ratio is 4/1, or even when it was 2/1.

4.4 Conclusions

PPTT is a novel therapy plan that has been repeatedly confirmed as feasible for subcutaneous tumor treatments. The present investigation numerically explored the feasibility of extending this therapy further to treat organ tumors, particularly tumors growing in the liver. Based on the simulations, the following conclusions were drawn:

1. PPTT is more demanding for laser delivery compared to PTT.
2. For the current case of liver tumor at 633 nm, when the nanoshell retention

ratio was less than $4/1$ (with 1 corresponding to a concentration of $1E16$ shells/ m^3), the intensity of thermal heat generation in normal liver tissues was unfavorably stronger. The retention ratio value of $4/1$ was the turning point, for which the values of bio-heat generation intensity in the liver tumor and in normal liver tissues were comparable. Only when the retention ratio was higher than $4/1$ did the intensity of thermal heat generation in the tumor exceed that in normal liver tissues.

3. As long as the “selective” therapeutic effect is the key focus, the therapeutic effect of PPTT under the nano-shell retention value $8/1$ was not better than it was when the retention ratio was $4/1$, or even $2/1$. Our simulations showed that the relation between the nanoshell tumor discrimination and the PPTT therapeutic effects was strongly nonlinear. Improving nanoshell tumor recognition does not promise more selective PPTT therapeutic effects. We therefore suggest that detailed preliminary numerical simulations should be conducted to gain some insights of therapeutic effects before a real experimental investigation is performed.

4.5 Remarks

This chapter is adapted from:

X. Xu, A. Meade Jr and Y. Bayazitoglu, “Feasibility of Selective Nanoparticle Assisted Photothermal Treatment for an Embedded Liver Tumor,” *Lasers in Medical Science* 2012, Accepted and to appear.

Bibliography

- [1] Goodrich G, Bao L, Gill-Sharp K, Sang K, Wang L and Payne J (2010) “Photothermal therapy in a murine colon cancer model using near-infrared absorbing gold nanorods”, *Journal of Biomedical Optics* 15(1): 018001-1 018001-7.
- [2] Lu W, Xiong C, Zhang G, Huang Q, Zhang R, Zhang J and Li C (2009) “Targeted photothermal ablation of murine melanomas with melanocyte-stimulating hormone analog - conjugated hollow gold nanospheres”, *Clinical Cancer Research* 15: 876-886.
- [3] Lal S, Clare S and Halas N (2008) “Nanoshell-enabled photothermal cancer therapy: impending clinical impact”, *Accounts of Chemical Research* 41(12): 1842-1851.
- [4] Terentyuk G, Maslyakova G, Suleymanova L, Khlebtsov N, Khlebtsov G, Akchurin G, Maksimova I and Tuchin V (2009) “Laser-induced tissue hyperthermia mediated by gold nanoparticles: toward cancer phototherapy”, *Journal of Biomedical Optics* 14(2): 021016-1 021016-9.
- [5] Matsumura Y and Maeda H (1986) “A new concept of macromolecular therapies in cancer chemotherapy: mechanism of tumor tropic accumulation of proteins and the antitumor agent SMANCS”, *Cancer Research* 6: 6387-6392.
- [6] Maeda H, Wu J, Sawa T, Matsumura Y and Hori K(2000) “ Tumor vascular per-

- meability and the EPR effect in macromolecular therapeutics: a review”, *Journal of Controlled Release* 65: 271-284.
- [7] Maeda H(2001) “The enhanced permeability and retention (EPR) effect in tumor vasculature: the key role of tumor-selective macromolecular drug targeting”, *Advances in Enzyme Regulation* 41: 189-207.
- [8] Maeda H, Fang J and Inutsuka T and Kitamoto Y (2003) “Vascular permeability enhancement in solid tumor: various factors, mechanisms involved and its implications”, *International Immunopharmacology* 3: 319-328.
- [9] Iyer A, Khaled G, Fang J and Maeda H(2006) “Exploiting the enhanced permeability and retention effect for tumor targeting”, *Drug Discovery Today* 11: 812-818.
- [10] Perrault S and Chan W (2010) “In vivo assembly of nanoparticle components to improve targeted cancer imaging”, *Proceeding of the National Academy of Sciences* 107(25): 11194-11199.
- [11] Ruoslahti E, Bhatia S and Sailor M (2010) “Targeting of drugs and nanoparticles to tumors”, *The Journal of Cell Biology* 188(6): 759-768.
- [12] Sassaroli E, Li K and O'Neill B (2009) “Numerical investigation of heating a gold nanoparticle and the surrounding microenvironment by nanosecond laser pulse for nanomedicine applications”, *Physics in Medicine and Biology* 54: 5541-5560.
- [13] Davis M, Chen Z and Shin D(2008) “Nanoparticle therapeutics: an emerging treatment modality for cancer”, *Nature Review* 7: 771-781.
- [14] Huang X, Jain P, El-Sayed I and El-Sayed M (2006) “Determination of the minimum temperature required for selective photothermal destruction of cancer cells with the use of immunotargeted gold nanoparticles”, *Photochemistry and Photobiology* 82: 412-417.

- [15] Xu X, Meade AJ, Bayazitoglu Y (2011) “Numerical investigation of nanoparticle-assisted laser-induced interstitial thermotherapy toward tumor and cancer treatment”, *Lasers in Medical Science* 26: 213-222.
- [16] Struesson C, Andersson-Engels S, Svanberg S(1995) “A numerical model for the temperature increase in surface-applied laser-induced thermo therapy with applications to tumor blood flow estimations. Laser-induced interstitial thermotherapy”, SPIE: Bellingham.
- [17] Svaasand L, Gomer C and Morinelli E (1990) “On the physical rationale of laser induced hyperthermia”, *Lasers in Medical Science* 15: 121-128.
- [18] Vera J and Bayazitoglu Y(2009)“Gold nanoshell density variation with laser power for induced hyperthermia”,*Int. J. Heat Mass Transfer* 52: 564-573.
- [19] Vera J and Bayazitoglu Y(2009)“A note on laser penetration in nanoshell deposited tissue”, *International Journal of Heat Mass Transfer* 52(13/14): 3402-3406.
- [20] Eillot AM, Schwartz JS, Wang J, Shetty AM, Bougoyne C, ONeal D, Hazle J and Stafford RJ (2009) “Quantitative comparison of delta P1 versus optical diffusion approximations for modeling near-infrared gold nanoshell heating”,*Med, Phys* 36(4):1351-1358.
- [21] Feng Y, Rylander MN, Bass J, Oden JT and Diller K (2005) “Optimal design of laser surgery for cancer treatment through nanoparticle-mediated hyperthermia therapy”, *NSTI-Nanotech* 1: 39-42.
- [22] Feng Y, Fuentes D, Hawkins A, Bass J, Rylander MN, Eillot A, Shetty A, Stafford RJ and Oden JT (2009) “Nanoshell-mediated laser surgery simulation for prostate cancer treatment”, *Engineering with Computers* 25 : 3-13.

- [23] Tjahjono I. and Bayazitoglu Y (2008) “Near-Infrared light heating of a slab by embedded nanoparticles”, *International Journal of Heat and Mass Transfer* 51:1505-1515.
- [24] Bayazitoglu Y(2009) “Nanoshell Assisted Cancer Thermal Therapy: Numerical Simulations”, *Proceedings of the 2nd ASME Micro/Nanoscale Heat Mass Transfer: An International Conference, Shanghai*.
- [25] Masters A, Bown SG (1990) “Interstitial laser hyperthermia in the treatment of tumors”, *Lasers in Medical Science* 5: 129-136.
- [26] Welch AJ, Gardner CM(1997)“Monte Carlo model for determination of the role of heat generation in laser-irradiated tissue”, *Journal of Biomechanical Engineering*119: 489-495.
- [27] Xu X, Meade, A, Bayazitoglu Y (2010) “Fluence rate distribution in laser-induced interstitial thermotherapy by meshfree collocation”, *International Journal of Heat and Mass Transfer* 53: 40174022.
- [28] Jode ML(2000) “Monte Carlo simulations of light distributions in an embedded tumor model: studies of selectivity in photo-dynamic therapy”, *Lasers in Medical Science* 15: 49-56.
- [29] Mie G (1908) “Beitrge zur Optik trber Medien, speziell kolloidaler Metallsungen. Leipzig”, *Annals of Physics* 330: 377445.
- [30] Prashant KJ, Lee KS, El-Sayed IH and El-Sayed MA (2006) “Calculated absorption and scattering properties of gold nanoparticles of different size, shape and composition: applications in biological imaging and biomedicine”, *Journal of physical chemistry B* 110: 7238-7248.

- [31] Takahashi H, Niidome T, Nariai A, Niidome Y and Yamada S (2006) “Photothermal reshaping of gold nanorods prevents further cell death”, *Nanotechnology* 17: 4431-4435.
- [32] Huang X, El-Sayed IH, Qian W and El-Sayed MA (2006) “Cancer cell imaging and photothermal therapy in the near-infrared region by using gold nanorods”, *Journal of the American Chemical Society* 128(6): 2115-2120.
- [33] Hirsch LR, Stafford RJ, Bankson JA, Sershen SR, Rivera B, Price RE, Hazle JD, Halas NJ and West JL(2003) “Nanoshell-mediated near-infrared thermal therapy of tumors under magnetic resonance guidance”, *Proceeding of National Academy of Science* 100(23): 13549-13554.
- [34] Loo C, Lin A, Hirsch L, Lee M, Barton J, Halas N, West J and Drezek R(2004) “Nanoshell-enabled photonics-based imaging and therapy of cancer”, *Technology in Cancer Research Treatment* 3(1): 33-40.
- [35] O’Neal DP, Hirsch LR and Halas NJ (2004) “Photo-thermal tumor ablation in mice using near infrared-absorbing nanoparticles”, *Cancer letters* 209(2):171-176.
- [36] Loo C, Lowery A, Halas NJ, West JL and Drezek R(2005) “Immunotargeted nanoshells for integrated cancer imaging and therapy”, *Nano Lett* 5: 709-711.
- [37] Shi Kam NW, O’Connell M, Wisdom JA and Dai H(2005) “Carbon nanotubes as multifunctional biological transporters and near-infrared agents for selective cancer cell destruction”, *Proceeding of National Academy of Science* 102(33): 11600-11605.
- [38] Chen J, Wiley B, Li ZY, Campbell D, Saeki F, Cang H, Au L, Lee J, Li X and Xie Y(2005) “Gold nanocages: engineering their structure for biomedical applications”, *Advanced Materials* 17: 2255-2261.

- [39] Hu M, Petrova H, Chen J, McLellan JM, Siekkinen AR, Marquez M, Li X, Xia Y and Hartland GV (2006) “Ultrafast laser studies of the photothermal properties of gold nanocages”, *Journal of physical chemistry B* 110(4): 1520-1524.
- [40] Link S and El-Sayed MA(2003) “Optical properties and ultrafast dynamics of metallic nanocrystals”, *Annual Review of Physical Chemistry* 54: 331-366.
- [41] Connor EE, Mwamuka J, Gole A, Murphy CJ and Wyatt MD (2005) “Gold nanoparticles are taken up by human cells but do not cause acute cytotoxicity”, *Small* 1: 325-327.
- [42] Shukla R, Bansal V, Chaudhary M, Basu A, Bhonde RR and Sastry M (2005) “Biocompatibility of gold nanoparticles and their endocytotic fate inside the cellular compartment: a microscopic overview”, *Langmuir* 21: 10644-10654.

A numerical investigation of nanoshells as the exogeneous optical contrast agent for early cancer diagnosis

5.1 Introduction

In modern medicine, nanoparticles have found applications in both the diagnostic and therapeutic procedures (1; 2; 3; 4; 5; 6; 7; 8; 9; 10; 11; 12; 13; 14; 15; 16; 17; 18; 19; 20; 21; 22; 23; 24; 25; 26; 27; 28; 29; 30; 31; 32; 33; 34; 35; 36). For therapeutic applications, nanoparticles are usually engineered to be the photo-thermal agent to promote the selectivity of the photo-thermal therapy. In Chapter 3 and Chapter 4, such applications have been numerically exploited. The most promising diagnostic application for nanoparticles might be being used as the exogenous optical contrast agent for optical imaging technique. The optical imaging technique is basically a scattering based imaging technique, heavily relying on how laser lights are absorbed and scattered when they propagate through the object that is being imaged. Imaging approaches such as the optical confocal microscopy (37; 38; 39), optical coherence tomography (40; 41; 42; 43) and spectroscopy (44; 45; 46) all fall

into this category. Compared to other more well-developed imaging modalities such as magnetic resonance imaging (MRI), radiology and positron emission tomography (PET), the optical imaging technique is advantageous in that it could capture images within micrometer resolution, improving the imaging resolutions ever achieved by 1 to 2 orders (43). This merit makes optical imaging approaches stand out among all the imaging modalities for early-staged cancer detection, particularly because the disease signature of precancerous tissues is usually too subtle for other alternatives.

The underlying motivation of applying the optical imaging technique to early-staged cancer diagnosis is that because of the differences in optical properties of normal tissues and precancerous tissues, the consequent contrasts in optical signatures could possibly be captured. Attracted by this idea, during the past decade, more and more efforts have been devoted to developing the optical imaging technique toward the early-staged cancer diagnosis. Simultaneously, producing highly efficient exogenous optical contrast agent for the optical imaging technique has also been brought up to the calendar. At the beginning, organic dyes such as the toluidine blue (47) and Lugol's iodine (48) were the major if not only candidates as optical contrast agent until the fast developing nano technology brought forward possible much stronger candidates, namely, the nanoparticles.

Nanoparticles could be much more efficient optical contrast agents compared to organic dyes in that their plasmonic resonance could easily be tuned to be 4 to 5 orders higher than that of organic dyes. Experimental explorations on engineering nanoparticles to be used for optical imaging procedures have been undergoing for a few years now (9; 11; 13; 15; 28; 29; 30; 31; 32; 33; 34; 35; 36; 37; 38; 39; 40; 41; 42; 43; 44) and different nanostructures have been tested for such purpose. For example, El-Sayed et al have used gold nanorods with an aspect ratio of 3.9 as the optical contrast agent

for their in vivo cancer cell imaging experiments (9; 33). Loo et al have targeted the R[60, 10] nm silica-gold nanoshell (nanoshell with a 60nm silica core and 10nm thick gold shell) with anti-HER2 as the optical contrast agent for in vitro cancer cell imaging experiments (28; 29; 30). Both groups have reported that the optical contrasts have been significantly enhanced by nanoparticles.

While experimental investigations “qualitatively” explore the feasibility of using nanoparticles as exogenous optical contrast agents, it is believed that numerical investigations could be a useful tool to “quantify” how nanoparticles alter the optical signatures. By now, for nanoparticle therapeutic application researches, numerical simulations have already been well recognized as a subsidiary tool for experimental explorations (1; 2; 3; 49; 50; 51; 52), playing an important role in optimal experiment/therapy plan, or even therapy monitoring. It is therefore quite nature to expect that for nanoparticle diagnostic application researches, numerical investigations could play a similar role, providing useful information and insights on how to engineer nanoparticles to be optimal optical contrast agent for specific imaging procedures.

Unfortunately, up to now, such researches efforts are extremely rare. To my information, only Lin and Halas (28) have performed some preliminary numerical investigations on the interactions of lasers and nanoshells for the benefit of engineering nanoshells toward disease diagnosis. Their investigation relied on the open sourced MCML (Monte Carlo modeling of photon transport in multi-layered tissues) package (53) to simulate laser light propagation within biological tissues, which could only handle semi-infinite, planar tissue layouts. Another limitation of MCML is that it assumes the laser source is a continuous waved (CW) one while in reality, short pulsed laser, particularly ultra-short pulsed laser whose radiance lasts from picoseconds to

nanoseconds are much more preferred for disease diagnosis in that optical signals that are revolving with time could carry more information of the optical properties of the tissue medium that the laser lights are traveled within.

Based on such a background, in this chapter, how nanoparticles, specifically, the silica-gold nanoshell could alter the optical signatures, specifically, the diffuse reflectance signature, of biological tissues would be exploited. In the present investigation, instead of modeling the laser lights as discontinuous photons using the stochastic Monte Carlo approach, the laser light propagation was described using the integral-differential radiative transfer equation (RTE), which is the alternative and mathematical equivalence of Monte Carlo light tracing. Also, different from what are for Chapter 2, 3 and 4, an ultra-short laser instead of a continuous waved laser would be used as the optical source.

The goal of the investigation is to explore the feasibility and efficiency of nanoshells as the exogenous optical contrast agent for early-staged cancer diagnosis. Around this goal, the following problems would be discussed: (1) How nanoshells of different optical properties would affect the diffuse reflectance signature; (2) Nanoshells with what kind of optical properties would make good exogenous optical contrast agent; (3) How other imaging factors such as the nanoshell concentration, optical properties of the precancerous tissues and surrounding normal tissues would affect the diffuse reflectance and how these factors could be manipulated toward better imaging.

5.2 Mathematical modeling

For diagnostic applications, short pulsed lasers, particularly, ultra-short pulsed lasers are much more favored signal sources compared to CW lasers. The reason is that

the captured optical signatures, namely the diffuse reflectance and the transmissivity, from a pulsed laser source would revolve with the time, conveying more information about the optical properties of the object that is under imaging.

The transient radiative transport equation (RTE) could be used to describe the interactions between laser lights that emit from a pulsed laser and the turbid tissue medium that is under imaged:

$$\frac{1}{c} \frac{\partial L(\mathbf{r}, \mathbf{s})}{\partial t} + \frac{\partial L(\mathbf{r}, \mathbf{s})}{\partial \mathbf{s}} + (k_{\alpha}(\mathbf{r}) + k_s(\mathbf{r}))L(\mathbf{r}, \mathbf{s}) = \frac{k_s(\mathbf{r})}{4\pi} \int_{4\pi} \Phi(\mathbf{s}, \mathbf{s}')L(\mathbf{r}, \mathbf{s}')d\omega' \quad (5.1)$$

Where $L(\mathbf{r}, \mathbf{s})$ indicates the radiant intensity, \mathbf{r} and \mathbf{s} are the position and direction vector respectively, c corresponds to the velocity with which laser lights propagate through the turbid medium, t indicates the time, ω indicates the solid angle, the kernel $\Phi(\mathbf{s}, \mathbf{s}')$ corresponds to the phase function, $k_{\alpha}(\mathbf{r})$ and $k_s(\mathbf{r})$ indicate the local absorption and scattering coefficient of the medium. If any exogenous optical contrast agents have been used, $k_{\alpha}(\mathbf{r})$ and $k_s(\mathbf{r})$ should count the influences from both the tissue medium and the exogenous optical contrast agent:

$$k_{\alpha}(\mathbf{r}) = k_{\alpha,tissue}(\mathbf{r}) + k_{\alpha,exogenous}(\mathbf{r}) \quad (5.2)$$

$$k_s(\mathbf{r}) = k_{s,tissue}(\mathbf{r}) + k_{s,exogenous}(\mathbf{r}) \quad (5.3)$$

As mentioned above, the silica-gold nanoshell was adopted as the exogenous optical contrast agent. For nanoshells, the absorption and scattering coefficient could be evaluated using their absorption efficiency Q_{abs} and scattering efficiency Q_{sca} respectively (1; 2; 3; 49; 50; 51):

$$k_{\alpha,exogenous} = C_{abs}N_T = \pi r_0^2 Q_{abs}N_T \quad (5.4)$$

$$k_{s,exogenous} = C_{sca}N_T = \pi r_0^2 Q_{sca}N_T \quad (5.5)$$

Where C_{abs} and C_{sca} are the absorption cross section and scattering cross section separately, N_T is the number of nanoshells per unit volume and r_0 indicates the radius of the silica core. Notice that for spherical particles such as nanoshells and nanospheres, Q_{abs} and Q_{sca} could be computed using Mie theory (54).

The fundamental idea of using nanoshells as the exogenous optical contrast agent is that by varying the core radius r_0 and core radius-to-shell thickness, the absorption cross section C_{abs} and the scattering cross section C_{sca} of nanoshells are agilely tunable. And by manipulating C_{abs} , C_{sca} and N_T , $k_{\alpha,exogenous}(\mathbf{r})$ and $k_{s,exogenous}(\mathbf{r})$ are controllable, and consequently the overall optical properties $k_{\alpha}(\mathbf{r})$ and $k_s(\mathbf{r})$ could be controlled as well. The goal is to manipulate $k_{\alpha}(\mathbf{r})$ and $k_s(\mathbf{r})$ in Eq. (5.1) such that consequently a desired distribution of $L(\mathbf{r}, \mathbf{s})$ could be achieved.

Depending on whether any laser lights emitting from a specific position, the boundary condition for Eq. (5.1) could be written as:

$$L_b(x_b, y_b, z_b, \mathbf{s}, t) = \epsilon q_0 \delta(\mathbf{s} - \mathbf{s}_c) \delta(t - t_p) + \frac{1 - \epsilon}{\pi} \int_{\mathbf{n} \cdot \mathbf{s}' < 0} L(x_b, y_b, z_b, \mathbf{s}', t) |\mathbf{n} \cdot \mathbf{s}'| d\omega' \quad (5.6)$$

Where the subscript b indicates the boundary, q_0 is the radiant flux of the emitting laser lights, t_p is the laser irradiance pulse, ϵ indicates the emissivity of the boundary and δ is the Dirac delta function.

Using the discrete ordinate method to discretize the integrals in Eq. (5.1), the integral-differential formed Eq. (5.1) could then be represented by a set of partial differential equations:

$$\begin{aligned} \frac{1}{c} \frac{\partial L(x, y, z, s_{mn}, t)}{\partial t} + \mu_{mn} \frac{\partial}{\partial x} L(x, y, z, s_{mn}, t) + \eta_{mn} \frac{\partial}{\partial y} L(x, y, z, s_{mn}, t) + \\ \xi_{mn} \frac{\partial}{\partial z} L(x, y, z, s_{mn}, t) + (k_{\alpha(x,y,z)} + k_s(x, y, z)) L(x, y, z, s_{mn}, t) = \quad (5.7) \\ \frac{k_s(x, y, z)}{4\pi} \sum_{m'=1}^M \sum_{n'=1}^M w_{m'n'} L(x, y, z, s_{m'n'}, t) \Phi(s_{mn}, s_{m'n'}) d\omega_{m'n'} \end{aligned}$$

Where μ_{mn} , η_{mn} and ξ_{mn} are direction cosines of the propagation direction s_{mn} of laser lights:

$$\mu_{mn} = \sin(\theta_m) \cos(\varphi_n) \quad (5.8)$$

$$\eta_{mn} = \sin(\theta_m) \sin(\varphi_n) \quad (5.9)$$

$$\xi_{mn} = \cos(\theta_m) \quad (5.10)$$

Notice that the subscripts m and n are the indices for the discretization of polar and azimuthal angle space respectively, i.e. $\theta_m \in [0, \pi]$ indicates the m -th discretized polar angle and $\varphi_n \in [0, 2\pi]$ indicates the n -th discretized azimuthal angle, $\omega_{m'n'}$ indicates the discretized solid angle defined by $\theta_{m'}$ together with $\varphi_{n'}$ and $w_{m'n'}$ is the weight associated with quadrature. In this investigation, we assume that both the polar and azimuthal space were divided into M subspaces.

For turbid medium such as biological tissues, $\Phi(s_{mn}, s_{m'n'})$ in Eq. (5.6) is usually represented by the Henyey-Greenstein scattering function:

$$\Phi(s_{mn}, s_{m'n'}) = \frac{1}{4\pi} \frac{1 - g^2}{1 + g^2 - 2g \cos(\gamma_{mn, m'n'})} \quad (5.11)$$

For $m, m', n, n' = 1, \dots, M$

Where $g \in [-1, 1]$ is the anisotropy factor, which is an indicator to define whether a scattering process is forward or backward, i.e., if $g > 0$, then the scattering process is preferentially forward, if $g = 0$, then the scattering process is isotropic and if $g < 0$, then the scattering process is preferentially backward. For biological tissues, usually the value of g is usually in the range of $[0.7, 1]$. Finally, $\gamma_{mn, m'n'}$ indicates the angle between the incident direction s_{mn} and outgoing direction $s_{m'n'}$. Consequently,

$$\cos(\gamma_{mn, m'n'}) = \mu_{mn} \cdot \mu_{m'n'} + \eta_{mn} \cdot \eta_{m'n'} + \xi_{mn} \cdot \xi_{m'n'} \quad (5.12)$$

The radiant intensity $L(x, y, z, s_{mn}, t)$ in Eq. (5-6) could be split into two parts, i.e. the attenuated incident radiant intensity $L_c(x, y, z, s_{mn}, t)$ and the diffuse radiant intensity $L_d(x, y, z, s_{mn}, t)$ induced by $L_c(x, y, z, s_{mn}, t)$:

$$L(x, y, z, s_{mn}, t) = L_c(x, y, z, s_{m_c n_c}, t) \delta[s_{mn} - s_{m_c n_c}] + L_d(x, y, z, s_{mn}, t) \quad (5.13)$$

Where δ indicates the Dirac delta function and $s_{m_c n_c}$ indicates the incident direction.

According to the Beer's law, the incident intensity of laser lights $L_c(x, y, z, s_{mn}, t)$ decays exponentially as the lights propagate within the tissue medium:

$$L_c(x, y, z, s_{mn}, t) = q_0 \exp(-(k(\alpha)(x, y, z) + k_s(x, y, z))z) \delta[s_{mn} - s_{m_c n_c}] [H(t - \frac{z}{c}) - H(t - t_p - \frac{z}{c})] \quad (5.14)$$

Where q_0 indicates the laser power, $H(t)$ is the Heaviside step function and t_p indicates the laser temporal duration. To simplify the problem, the laser pulse is assumed to be of the square shaped while for real, the pulses are normally Gaussian shaped.

Substitute Eq. (5.13) and Eq. (5.14) back into Eq. (5.7) and after some simple implementations, the expression of the diffusion radiation intensity $L_d(x, y, z, s_{mn}, t)$ is derived as:

$$\begin{aligned}
& \frac{1}{c} \frac{\partial L_d(x, y, z, s_{mn}, t)}{\partial t} + \mu_{mn} \frac{\partial L_d(x, y, z, s_{mn}, t)}{\partial x} + \eta_{mn} \frac{\partial L_d(x, y, z, s_{mn}, t)}{\partial y} + \\
& \xi_{mn} \frac{\partial L_d(x, y, z, s_{mn}, t)}{\partial z} + (k_\alpha(x, y, z) + k_s(x, y, z)) L_d(x, y, z, s_{mn}, t) = \\
& \frac{k_s(x, y, z)}{4\pi} \sum_{m'=1}^M \sum_{n'=1}^M w_{m'n'} L_d(x, y, z, s_{m'n'}, t) \Phi(s_{mn}, s_{m'n'}) + \\
& \frac{k_s(x, y, z)}{4\pi} w_{m_c n_c} L_c(x, y, z, s_{m_c n_c}, t) \Phi(s_{mn}, s_{m_c n_c})
\end{aligned} \tag{5.15}$$

Notice that Eq. (5.15) involves multi scales, for easier implementation, we can nondimensionalize Eq. (5.15). Define the scaling factors t^* , x^* , y^* , and z^* as the following:

$$t^* = (k_\alpha + k_s)ct \tag{5.16}$$

$$x^* = xt \tag{5.17}$$

$$y^* = yt \tag{5.18}$$

$$z^* = zt \tag{5.19}$$

After some simple implementation, the scaling version of Eq. (5.15) could then written as:

$$\begin{aligned}
& \frac{\partial L_d(x^*, y^*, z^*, s_{mn}, t^*)}{\partial t} + \mu_{mn} \frac{\partial L_d(x^*, y^*, z^*, s_{mn}, t^*)}{\partial x^*} + \eta_{mn} \frac{\partial}{\partial y} L_d(x^*, y^*, z^*, s_{mn}, t^*) + \\
& \quad \xi_{mn} \frac{\partial}{\partial z} L_d(x^*, y^*, z^*, s_{mn}, t^*) + L_d(x^*, y^*, z^*, s_{mn}, t^*) = \\
& \quad \frac{\omega(x^*, y^*, z^*)}{4\pi} \sum_{m'=1}^M \sum_{n'=1}^M w_{m'n'} L_d(x^*, y^*, z^*, s_{m'n'}, t^*) \Phi(s_{mn}, s_{m'n'}) + \\
& \quad \frac{\omega(x^*, y^*, z^*)}{4\pi} w_{m_c n_c} L_c(x^*, y^*, z^*, s_{m_c n_c}, t^*) \Phi(s_{mn}, s_{m_c n_c})
\end{aligned} \tag{5.20}$$

Where $\omega(x^*, y^*, z^*) = \frac{k_s(x^*, y^*, z^*)}{k_s(x^*, y^*, z^*) + k_a(x^*, y^*, z^*)}$ is the local scattering albedo.

Correspondingly, the scaling version of the boundary condition equation Eq. (5.6) is:

$$\begin{aligned}
& L_d(x_b^*, y_b^*, z_b^*, s_{mn}, t^*) = \\
& \epsilon q_0 \delta[s_{mn} - s_{m_c n_c}] + \frac{1 - \epsilon}{\pi} \int_{\mathbf{n} \cdot \mathbf{s}' < 0} L_d(x_b^*, y_b^*, z_b^*, s_{m'n'}, t^*) |\mathbf{n} \cdot \mathbf{s}_{m'n'}| d\omega_{m'n'}
\end{aligned} \tag{5.21}$$

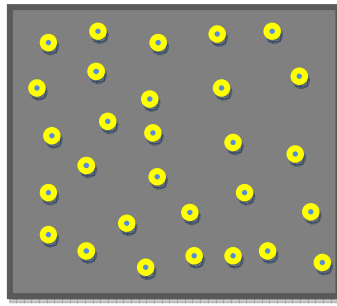
and the scaling version of Eq.(5.14) for the attenuated incident radiant intensity is rewritten as:

$$L_c(x^*, y^*, z^*, s_{m_c n_c}, t^*) = q_0 \exp(-z^*) [H(t^* - z^*) - H(t^* - t_p^* - z^*)] \tag{5.22}$$

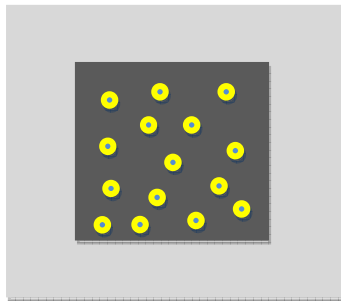
The solving of Eq. (5.20)-(5.21) requires numerical approximation.

5.3 Results and discussion

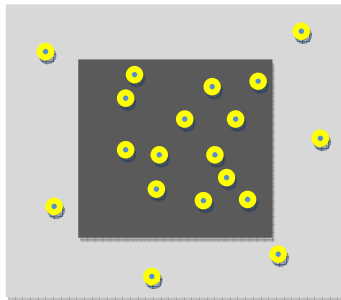
In total seven generics of nanoshells have been tested as the exogenous optical contrast agent, including the $R[50, 10]nm$ (nanoshells with a 50 nm silica core and



(a)



(b)



(c)

FIGURE 5.1: Schematic illustrations: (a) Nanoshells embedded in bulky precancerous tissues; (b) Nanoshells embedded in precancerous tissue that is enclosed by normal tissues; (c) Nanoshells embedded in precancerous tissue that is enclosed by normal tissues, nanoshells found in both tissues

Table 5.1: Optical properties under the wavelength 830nm for nanoshells of different size and core/shell ratio

Nanoshell Types	Ext. Eff.	Sca/Abs	Sca. Eff.	Abs. Eff.	C_{Sca}	C_{Abs}
$R[50, 10]nm$	4.047	0.38	1.11	2.93	$8.75E - 11$	$2.30E - 10$
$R[40, 15]nm$	2.62	0.701	1.08	1.54	$5.43E - 11$	$7.74E - 11$
$R[55, 25]nm$	4.4414	3.199	3.38	1.06	$3.22E - 10$	$1.01E - 10$
$R[40, 40]nm$	3.738	6.27	3.22	0.514	$1.62E - 10$	$2.58E - 11$
$R[75, 40]nm$	3.7	8.98	3.33	0.371	$5.88E - 10$	$6.55E - 11$
$R[104, 23]nm$	3.68	3.34	2.83	0.848	$9.63E - 10$	$2.88E - 10$
$R[154, 24]nm$	4.074	3.132	3.088	0.986	$2.30E - 09$	$7.35E - 10$

a 10nm thick gold shell), $R[40, 15]nm$, $R[55, 25]nm$, $R[40, 40]nm$, $R[75, 40]nm$, $R[104, 23]nm$ and $R[154, 24]nm$ nanoshells. Notice that in order to avoid considering the inter-nanoshell effects, only nanoshells with relative small overall size have been selected here. Optical properties including the extinction efficiency, the ratio of scattering efficiency-to-absorption efficiency, the absorption and scattering efficiency and the absorbing and scattering cross section for the seven generics of nanoshells are listed in Table 5.1. Specifically, the information of extinction efficiency and the ratio of scattering efficiency-to-absorption efficiency is taken from the reference (55), based on which the rest information were derived by ourselves through some simple calculations following Eq. (5.4) and Eq. (5.5). Notice that among all the seven generics, $R[50, 10]nm$ and $R[40, 15]nm$ nanoshells are preferentially absorbing with their absorption cross section higher than their scattering cross section while the rest five generics are all preferentially scattering.

Three phantom models have been covered here: model (a) The laser lights directly illuminated the precancerous tissue bulk with nanoshells embedded within (as Fig. 5.1(a) schematically illustrated); model (b) The precancerous tissue bulk was enclosed from the outside by the normal tissue bulk, nanoshells were assumed to be confined totally in the precancerous tissue bulk (as Figure. 5.1(b) schematically

illustrated). Such an assumption only holds when nanoshells show perfect discriminations between the precancerous tissue and the normal tissue; model (c) The tissue layout was the same as (b), but nanoshells were found in both the precancerous tissue bulk and the enclosing normal tissues bulk. However, the nanoshell concentration in the normal tissue bulk was assumed to be ten times lower (as Figure.5.1(c) schematically illustrated). The model (c) accounts for situations that nanoshells could not perfectly recognize the precancerous tissue from the normal tissue. During the recent few years, reports of in-vivo bio-distribution of nanoparticles(21) kept on emerging, revealing that nanoshells only show strong discrimination ability for subcutaneous cancers while for organ cancers including cancers in the liver, spleen, lung and the kidney, such discrimination ability of nanoshells were noticeable weaker. The model (c) was therefore specifically targeted for such situations.

The laser lights illuminating the phantoms were assumed to be from a $830nm$ ultra-short laser whose pulse persisted during the time range $0 \leq t^* \leq 1$ and after the time point $t^* = 1$, the pulse elapsed. The references (56; 57) have given ranges of optical properties of precancerous tissues under different wavelengths. Based on the given information, it was assumed that for the wavelength of $830nm$, the absorption coefficient of the precancerous tissues was 0.05 cm^{-1} , and the scattering coefficient was 50 cm^{-1} . And for the enclosing normal tissue in model (b) and (c), the absorption and scattering coefficient were assumed to be 1.5 cm^{-1} and 50 cm^{-1} respectively. It has been made sure that the optical properties of both the precancerous tissue and the normal tissues are in the range given in the references (56; 57). For both the precancerous tissue and normal tissue, the anisotropy factor was assumed to be 0.9 and the refractive index was fixed to be 1.37.

In order to investigate how the nanoshell concentration affects the diffuse re-

flectance signature, the concentration of nanoshells embedded in the precancerous tissue bulk was increased sequentially from $1E9$ nanoshells/ml to $1E10$ nanoshells/ml and then to $1E11$ nanoshells/ml . Notice that in order to avoid considering the inter-nanoshell effects, no high concentration values were used here.

Firstly, we discuss how nanoshells alter the diffuse reflectance signature in phantom model (a). Since the optical signal was from an ultra-short laser, consequently, the diffuse reflectance signature revolved with the time as well. Fig. 5.2(left) compared the time-revolved diffuse reflectance (in absolute value) before and after a concentration of $1E9$ nanoshells/ml nanoshells were embedded in the precancerous tissue bulk. Fig. 5.2(right) presented the relative alterations in the diffuse reflectance after the adding of nanoshells, computed by dividing the differences of diffuse reflectance before and after the addition of the nanoshells by the values of diffuse reflectance before the addition of nanoshells, computed by dividing the differences of diffuse reflectance before and after the addition of the nanoshells by the values of diffuse reflectance before the addition of nanoshells.

According to Fig.5.2, the diffuse reflectance increased monotonously during the laser pulse duration ($0 \leq t^* \leq 1$) and degrading monotonously beyond the time point $t^* = 1$. The degrading was much gradual compared to the increase before $t^* = 1$, which could be explained by the fact that the precancerous tissue is turbid and the multi-scattering phenomenon specifically for turbid medium render the diffuse reflectance from decreasing very fast even though the laser pulse elapsed.

Read from Fig.5.2, all seven generics of nanoshells have only altered the diffuse reflectance marginally when the nanoshell concentration was $1E9$ nanoshells/ml . Relatively speaking, when the laser pulse elapsed, the impacts of nanoshells on the

diffuse reflectance were more obvious compared to what was during the laser pulse duration. Before adding any nanoshells, the diffuse reflectance peak was about 0.49. However, all seven generics of nanoshells diminished the diffuse reflectance, at different levels though, despite the fact that five of the seven generics of nanoshells are preferentially scattering with their scattering cross section several times higher than their absorption cross section.

Particularly, the $R[40,40]nm$ nanoshell diminished the diffuse reflectance the least (-0.05% ~ -0.1%) while the $R[154,24]nm$ nanoshell diminished the diffuse reflectance the most (-1.5% ~ -3.2%). (The numbers inside the parenthesis were the approximate range of the relative alternations in the diffuse reflectance after the addition of nanoshells, the symbol minus indicates that the diffuse reflectance was reduced by nanoshells) Notice that both the $R[154,24]nm$ nanoshell and the $R[40,40]nm$ nanoshells are preferentially scattering. Particularly, the $[154,24]nm$ nanoshells has the highest scattering cross section among all seven generics of nanoshells while the $[40,40]nm$ nanoshell has the lowest scattering cross section among the five generics of nanoshells that are preferentially scattering. If we rank the nanoshells in the order of increasing impacts on the diffuse reflectance, the ranking would be $R[40,40]nm$ (-0.05% ~ -0.1%), $R[75,40]nm$ (-0.15% ~ -0.3%), $R[40,15]nm$ (-0.17% ~ -0.35%), $R[55,25]nm$ (-0.2% ~ -0.5%), $R[50,10]nm$ (-0.5% ~ -1.1%), $R[104,23]nm$ (-0.55% ~ -1.35%) and $R[154,24]nm$ (-1.5% ~ -3.2%).

Fig. 5.3 and Fig. 5.4 presented the time-resolved diffuse reflectance and the relative changes in diffuse reflectance when the concentration for the nanoshells was increased from $1E9$ nanoshells/ml to $1E10$ nanoshells/ml and then further to $1E11$ nanoshells/ml. It was seen that with more nanoshells being embedded, the impacts of nanoshells on the diffuse reflectance increased noticeably as well. However,

two facts remained unchanged: firstly, the diffuse reflectance was diminished by nanoshells, regardless of the nanoshell generics; secondly, the impacts of nanoshells on the diffuse reflectance were more obvious after the laser pulse elapsed.

When the nanoshell concentration was $1E10$ nanoshells/ml , the $R[40, 40]nm$ nanoshells remained to be the generic of nanoshell that diminished the diffuse reflectance the least ($-0.5\% \sim -1\%$) percent while the $R[154, 24]$ nanoshell remained to be the one that diminished the diffuse reflectance the most ($-9\% \sim -20\%$) . In the order of increasing impacts on the diffuse reflectance, the seven generics of nanoshells could be ranked as $R[40, 40]nm$ ($-0.5\% \sim -1\%$) , $R[75, 40]nm$ ($-1.5\% \sim -2.2\%$) , $R[40, 15]nm$ ($-1.8\% \sim -3.8\%$) , $R[55, 25]nm$ ($-2\% \sim -4\%$) , $R[50, 10]nm$ ($-4\% \sim -8\%$) , $R[104, 23]nm$ ($-4.2\% \sim -8.2\%$) and $R[154, 24]nm$ ($-9\% \sim -20\%$) . It could be seen that this ranking is the same as what was when the nanoshell concentration was $1E9$ nanoshells/ml .

Fig.5.4 however showed something different from Fig. 5.2 and Fig. 5.3. Firstly, it was noticed that for the nanoshell concentration $1E11$ nanoshells/ml , nanoshells have altered the diffuse reflectance greatly compared to the previous two nanoshell concentrations. Secondly, according to Fig.5.4, although the $R[40, 40]nm$ nanoshell remained to be the one that brought down the diffuse reflectance least ($-4\% \sim -10\%$), the $R[50, 10]nm$ nanoshell replaced the $R[154, 23]nm$ nanoshell to become the nanoshell that diminished the diffuse reflectance most ($-30\% \sim -50\%$) . Particularly, notice that the $R[50, 10]nm$ nanoshell was one of the two generics of nanoshells that are preferentially absorbing with its absorbing cross section being more than two times higher than its scattering cross section. Rank the nanoshells in the order of increasing impacts on the diffuse reflectance, the ranking was $R[40, 40]nm$ ($-4\% \sim -10\%$) , $R[75, 40]nm$ ($-5\% \sim -12\%$) , $R[55, 25]nm$ ($-11\% \sim -23\%$), $R[40, 15]nm$ (-12%

$\sim -25\%$), $R[104, 23]nm$ ($-16\% \sim -32\%$), $R[154, 24]nm$ ($-20\% \sim -40\%$), $R[50, 10]nm$ ($-30\% \sim -50\%$). Notice that this ranking is very different from the rankings when the nanoshell concentration were $1E9$ nanoshells/ml and $1E10$ nanoshells/ml .

One existing opinion about using nanoshells as the optical contrast agent is that nanoshells that are preferentially scattering generally would augment the diffuse reflectance because of the enhancement in scattering they could bring, and since nanoshells used for such purposes usually have a very high scattering efficiency compared to their absorption efficiency, it is somehow justified to neglect the absorption the nanoshells would bring to the tissue medium. What Fig.5.2, Fig.5.3 and Fig.5.4 have presented obviously contradicted this opinion.

Based on Fig.5.2, Fig.5.3 and Fig.5.4, it is analyzed and argued that if using the nanoshells as the optical contrast agent, whether the diffuse reflectance signature would be enhanced or reduced by nanoshells is not decided by whether the nanoshells are preferentially absorbing or scattering, or even the scattering efficiency-to-absorption efficiency ratio of nanoshells. As Fig.5.2-5.4 have illustrated, nanoshells that are preferentially scattering with their scattering cross section orders higher than their absorption cross section are as capable of reducing the diffuse reflectance as nanoshells that are preferentially absorbing. It is suggested based on Fig.5.2-5.4 that after adding the nanoshells to the tissue medium, if the scattering albedo of the overall medium is higher than the scattering albedo of the precancerous tissue alone, then the diffuse reflectance signature would be enhanced, otherwise it would be reduced. The more the scattering albedo is altered by adding the nanoshells, the bigger the impact of nanoshells on the diffuse reflectance is.

It is therefore proposed that the modified scattering albedo should be used as the

index to judge whether the diffuse reflectance would increase or decrease by adding nanoshells, which is formulated as:

$$\omega^* = \frac{k_{s,tol}}{k_{s,tol} + k_{\alpha,tol}} = \frac{k_{s,tissue} + k_{s,exogeneous}}{k_{s,tissue} + k_{s,exogeneous} + k_{\alpha,tissue} + k_{\alpha,exogeneous}} \quad (5.23)$$

And the rule is if

$$\omega^* > \omega = \frac{k_{s,tissue}}{k_{s,tissue} + k_{\alpha,tissue}} \quad (5.24)$$

Then the diffuse reflectance would be enhanced, otherwise, reduced. The bigger the value of $\omega^* - \omega$ is, the bigger the nanoshells impact on the diffuse reflectance would be.

In order to verify this argument, the scattering albedo of the overall medium before and after each generic of nanoshells were added is computed and the changes of the scattering albedo is listed in Table.5.2(corresponding to nanoshell concentration $1E9$ nanoshells/ml) Table.5.3(corresponding to nanoshell concentration $1E10$ nanoshells/ml) and Table.5.4(corresponding to nanoshell concentration $1E11$ nanoshells/ml). It could easily be seen from the three tables. that after adding each generic of nanoshells, the consequent ω^* is smaller than the original ω , the higher the nanoshell concentration is, the bigger the decrease in ω^* was.

Since the precancerous tissues usually have a very small absorption coefficient, particularly relative to their scattering coefficient, ω for the precancerous tissue is usually very high. Therefore, although it is possible to tune the absolute value of nanoshell scattering cross section to be orders higher than their absorption cross section, it would still be challenging to engineering nanoshells such that after adding

Table 5.2: Under the wavelength of $830nm$, the overall optical properties of the tissue medium when the embedded nanoshells concentration is $1E9$ nanoshells/ml

nanoshells	Overall sca. coef.	Overall abs. coef.	ω	$\Delta\omega$
R[50,10]nm	50.0875	0.28	0.994441	-0.00456
R[40,15]nm	50.0543	0.1274	0.997461	-0.00154
R[55,25]nm	50.322	0.151	0.997008	-0.00199
R[40,40]nm	50.162	0.0758	0.998491	-0.00051
R[75,40]nm	50.588	0.1155	0.997722	-0.00128
R[104,23]nm	50.963	0.338	0.993411	-0.00559
R[154,24]nm	52.3	0.785	0.985212	-0.01379

Table 5.3: Under the wavelength of $830nm$, the overall optical properties of the tissue medium when the embedded nanoshells concentration is $1E10$ nanoshells/ml

nanoshells	Overall sca. coef.	Overall abs. coef.	ω	$\Delta\omega$
R[50,10]nm	50.875	2.35	0.955848	-0.04315
R[40,15]nm	50.543	0.824	0.983959	-0.01504
R[55,25]nm	53.22	1.06	0.980472	-0.01853
R[40,40]nm	51.62	0.308	0.994069	-0.00493
R[75,40]nm	55.88	0.705	0.987541	-0.01146
R[104,23]nm	59.63	2.93	0.953165	-0.04584
R[154,24]nm	73	7.4	0.90796	-0.09104

Table 5.4: Under the wavelength of $830nm$, the overall optical properties of the tissue medium when the embedded nanoshells concentration is $1E11$ nanoshells/ml

nanoshells	Overall sca. coef.	Overall abs. coef.	ω	$\Delta\omega$
R[50,10]nm	58.75	23.05	0.718215	-0.28079
R[40,15]nm	55.43	7.79	0.87678	-0.12222
R[55,25]nm	82.2	10.15	0.890092	-0.10891
R[40,40]nm	66.2	2.63	0.96179	-0.03721
R[75,40]nm	108.8	6.6	0.942808	-0.05619
R[104,23]nm	146.3	28.85	0.835284	-0.16372
R[154,24]nm	280	73.55	0.791967	-0.20703

which, $\omega^* > \omega$ holds.

By now, I have discussed how nanoshells alter the diffuse reflectance signature for model (a), what is about model (b)? The time-revolved diffuse reflectance under different nanoshell concentrations for which were presented as Fig.5.5, Fig5.6 and Fig.5.7. Notice that although the absorption coefficient of the enclosing normal tissue is 20 times that of the precancerous tissue, it is still really small relative to its scattering efficient. In other words, for both tissues, the scattering heavily dominated the extinction and the scattering albedo of the normal tissue (0.98) is still really close in value to that of the precancerous tissue (0.99) . Consequently, before adding any nanoshells, the diffuse reflectance for both models were close to each other.

However, if compare Fig.5.5-5.7 to Fig.5.2-5.4, it could be seen that the impacts of nanoshells on the diffuse reflectance for model (b) were much stronger than what was for model (a). And due to the nonlinear interactions of the enclosing normal tissue and the laser lights, it can no longer be simply predicted the impact of nanoshells on the diffuse reflectance by checking the change in the overall scattering albedo brought by nanoshells. For example, for model (b), when the nanoshell concentration was $1E11$ nanoshells/ml , if we rank the seven generics of nanoshells in the order of increasing influences on the diffuse reflectance, the ranking would be the $R[40, 15]nm$ (-20 % ~ -35%) , $R[40, 40]nm$ (-30% ~ -50%) , $R[50, 10]nm$ (-40% ~ -65%) , $R[55, 25]nm$ (-47% ~ -70%) , $R[75, 40]nm$ (-58% ~ -80%) , $R[104, 23]nm$ (-70 % ~ -90%) and $R[154, 24]nm$ nanoshells (-85% ~ -95%). It could be seen that the $R[104, 23]nm$ and $R[154, 24]nm$ nanoshells almost diminish the diffuse reflectance to zero. Also it was noticed that the ranking of nanoshells here was not the same as what was when the nanoshell concentration was $1E11$ nanoshells/ml for model (a).

We now move further to model (c). For this model(c), nanoshell concentration in the precancerous tissue bulk was assumed to be $1E10$ nanoshells/ml and $1E11$ nanoshells/ml separately, and the nanoshell concentration in the normal tissue bulk was 10 times lower. The time-revolved diffuse reflectance for this model was presented as Fig.5.8 and Fig.5.9. Compare Fig. 5.8 to Fig. 5.6 (for both the nanoshell concentration was $1E10$ nanoshells/ml) and compare Fig. 5.9 to Fig5.7 (for both the nanoshell concentration was $1E11$ nanoshells/ml), it could be seen the diffuse reflectance diminished even more in model(c), compared to model (b), induced by the nanoshells scattered in the normal tissue bulk. However, the impact of the nanoshell concentration was not as obvious for model(c) as it was for model (b). It could also be seen that after the nanoshell concentration was increased from $1E10$ nanoshells/ml to $1E11$ nanoshells/ml, the transitions of the diffuse reflectance was not as obvious as what was for model (b).

5.4 Conclusions

How gold-silica nanoshells alter the diffuse reflectance signature of different tissue phantoms has been numerically investigated for the purpose of exploring how to engineering nanoshells to be good exogenous optical contrast agent for early-staged cancer diagnostic imaging. Seven generics of nanoshells were tested including the $R[50, 10]nm$, $R[40, 15]nm$, $R[55, 25]nm$, $R[40, 40]nm$, $R[75, 40]nm$, $R[104, 23]nm$ and $R[154, 24]nm$ nanoshells. Particularly, the $R[50, 10]nm$ and $R[40, 15]nm$ nanoshells are preferentially absorbing while the rest five generics are preferentially scattering.

Based on the investigation, it is concluded that: (1) By affecting the scattering albedo of the overall medium, nanoshells are able to alter the diffuse reflectance. Nanoshells whose optical properties and concentration are such that after adding

them, the overall scattering albedo is changed dramatically, then it could be expected that the diffuse reflectance would be altered noticeable as well. Particularly, if the overall scattering albedo is larger than that of the precancerous tissue alone, the diffuse reflectance could be expected to be enhanced, otherwise, it would be diminished. Since precancerous tissues usually have a very high scattering albedo for the near infrared spectrum, it would be very challenging to engineering nanoshells such that after adding them, the diffuse reflectance is enhanced. (2) For most real situations, precancerous tissues are usually embedded within the normal tissue bulk, and if the cancers are in the organs instead of being subcutaneous, the enclosing healthy organ tissue would retain a certain amount of nanoshells as well. For such situations, even the conditions related to the nanoshells, including the nanoshell generic and concentration, are all the same, the optical contrasts induced by nanoshells would be still be more obvious compared to when the precancerous tissue is bare to laser lights. In order to count for the nonlinearity of the interactions of the normal tissues, nanoshells retained by the normal tissues and the laser lights, we strongly suggest that for such situations, preliminary numerical investigations should be performed for us to have some insights on how the nanoshells would alter the diffuse reflectance before any real experiments are planned.

5.5 Remarks

This chapter is adapted from:

X. Xu, A. Meade, Jr. and Y. Bayazitoglu, "A numerical investigation of nanoshells as the exogenous optical contrast agent for early cancer diagnostic," in preparation, 2012.

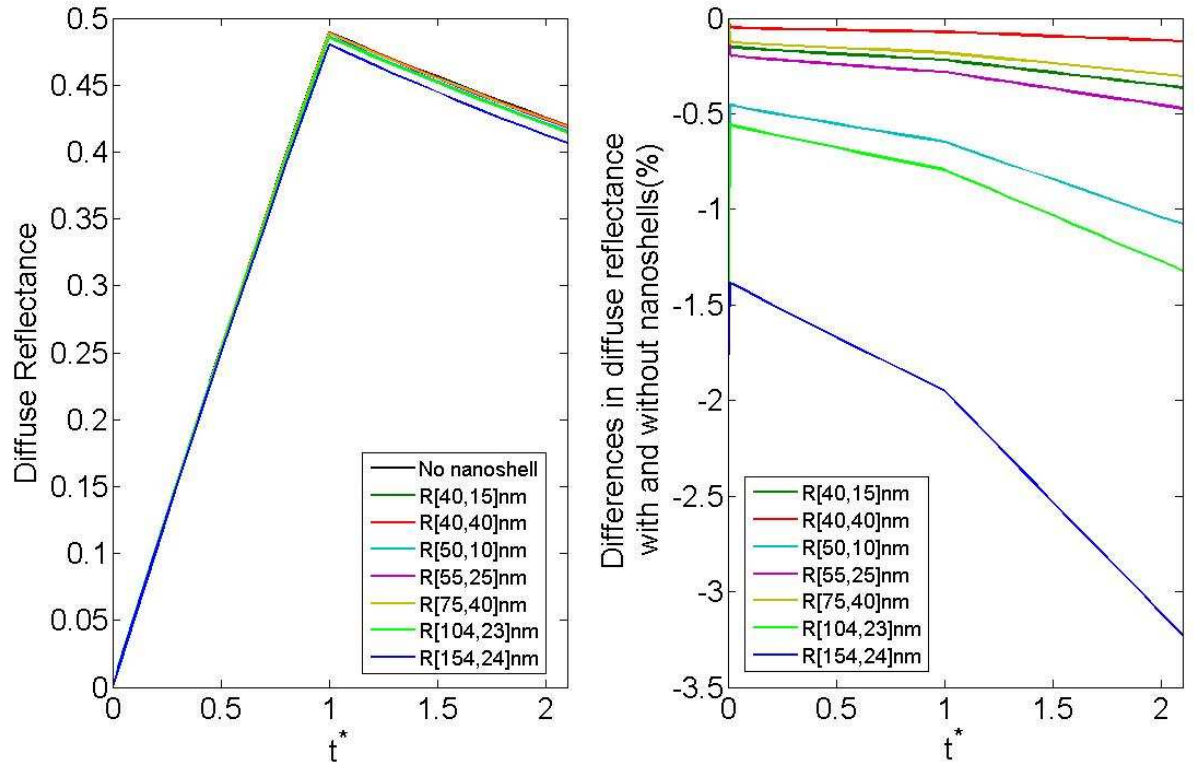


FIGURE 5.2: Transient diffuse reflectance at the laser emitting face when types of nanoshells were embedded in bulky cancerous tissues (absorption coefficient $k_\alpha = 0.05 \text{ cm}^{-1}$, the scattering coefficient $k_s = 50 \text{ cm}^{-1}$) as the optical contrast agent. The embedded nanoshell concentration was $1E9$ nanoshells/ml

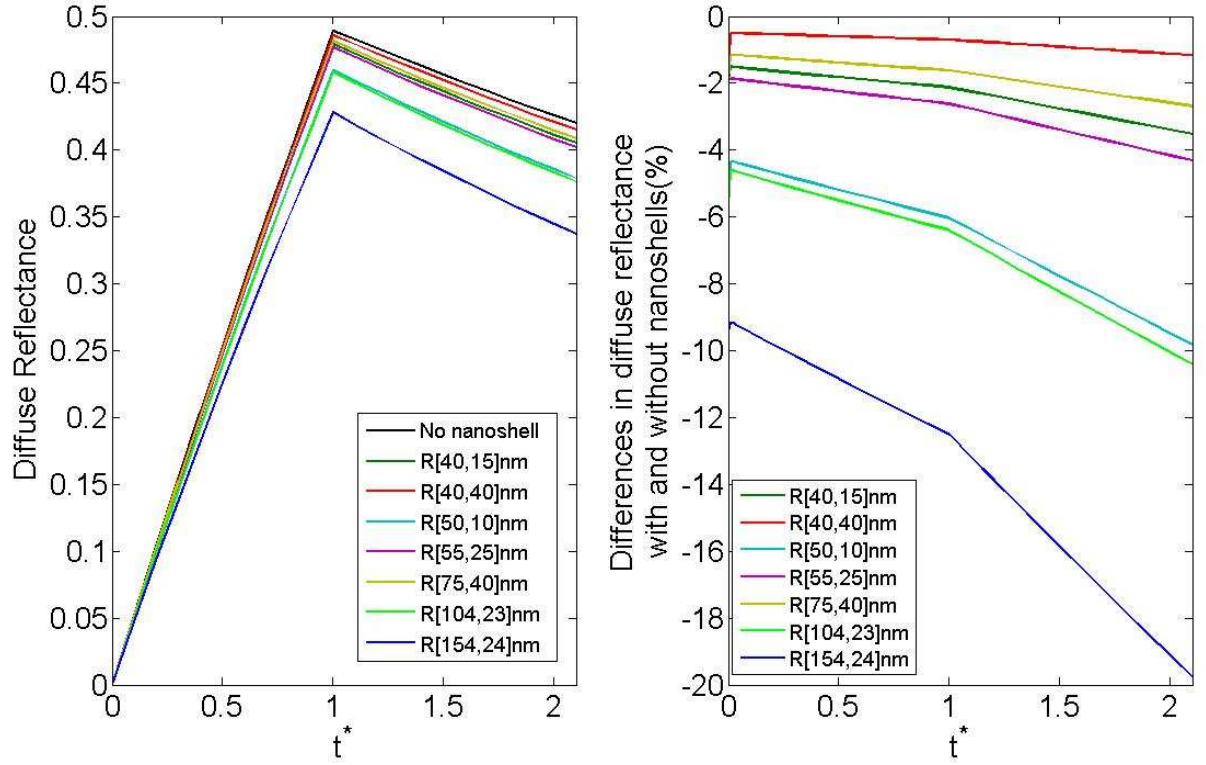


FIGURE 5.3: Transient diffuse reflectance at the laser emitting face when types of nanoshells were embedded in bulky cancerous tissues (absorption coefficient $k_{\alpha} = 0.05 \text{ cm}^{-1}$, the scattering coefficient $k_s = 50 \text{ cm}^{-1}$) as the optical contrast agent. The embedded nanoshell concentration was $1E10$ nanoshells/ml

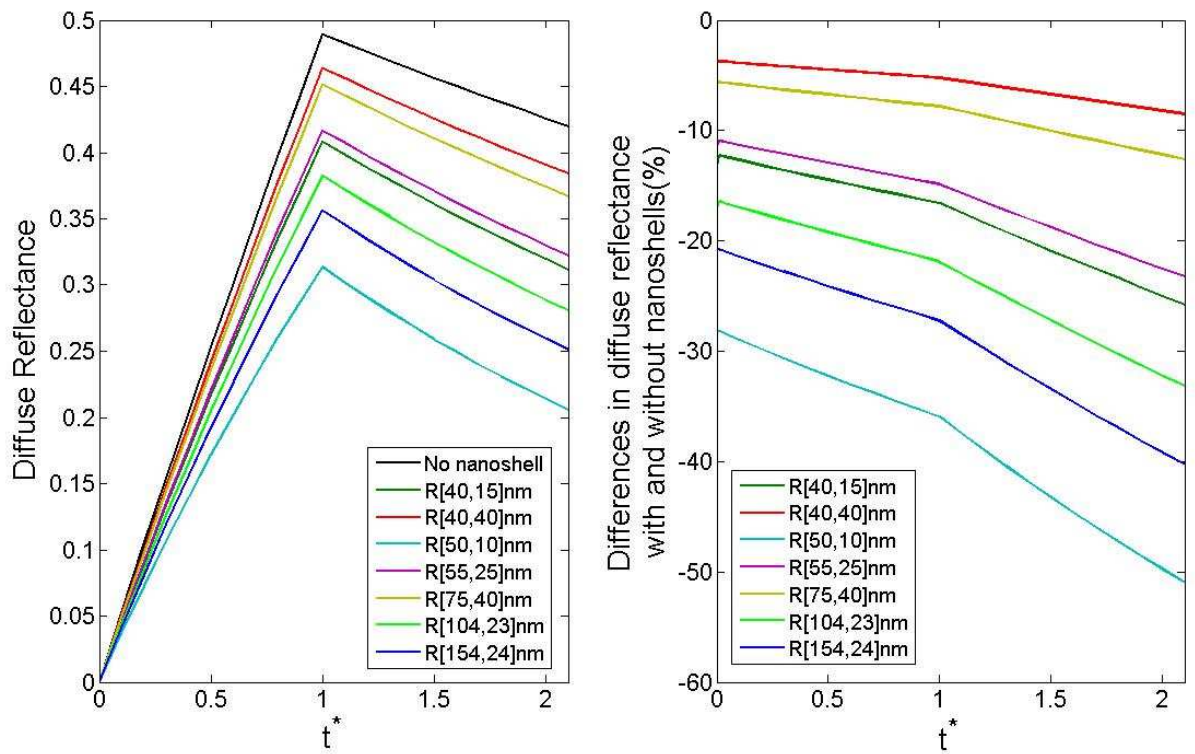


FIGURE 5.4: Transient diffuse reflectance at the laser emitting face when types of nanoshells were embedded in bulky cancerous tissues (absorption coefficient $k_{\alpha} = 0.05 \text{ cm}^{-1}$, the scattering coefficient $k_s = 50 \text{ cm}^{-1}$) as the optical contrast agent. The embedded nanoshell concentration was $1E11$ nanoshells/ml

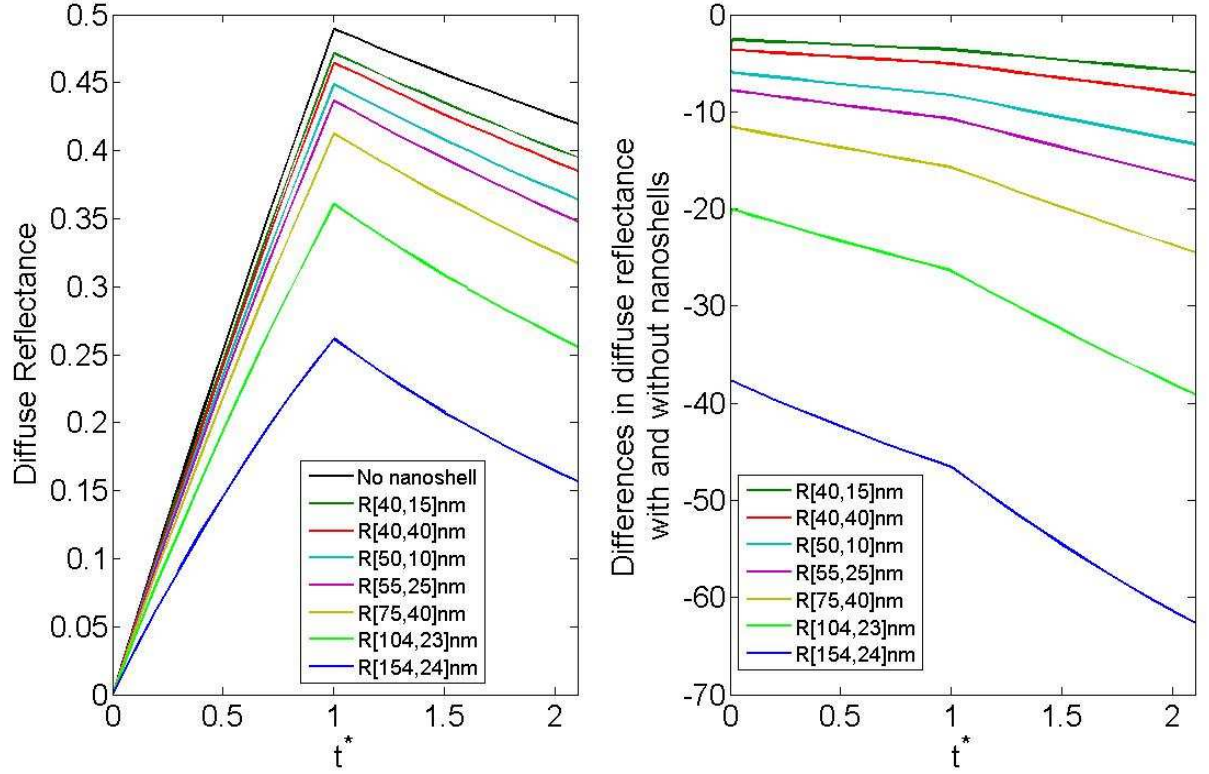


FIGURE 5.5: Transient diffuse reflectance at the laser emitting face when types of nanoshells were embedded in cancerous tissues ($k_a = 0.05cm^{-1}$, the scattering coefficient $k_s = 50cm^{-1}$) which were enclosed by normal healthy tissues (absorption coefficient $k_a = 1.5cm^{-1}$, the scattering coefficient $k_s = 50cm^{-1}$) as the optical contrast agent. Nanoshells were found in cancerous tissues only, the nanoshell concentration is $1E9$ nanoshells/ml

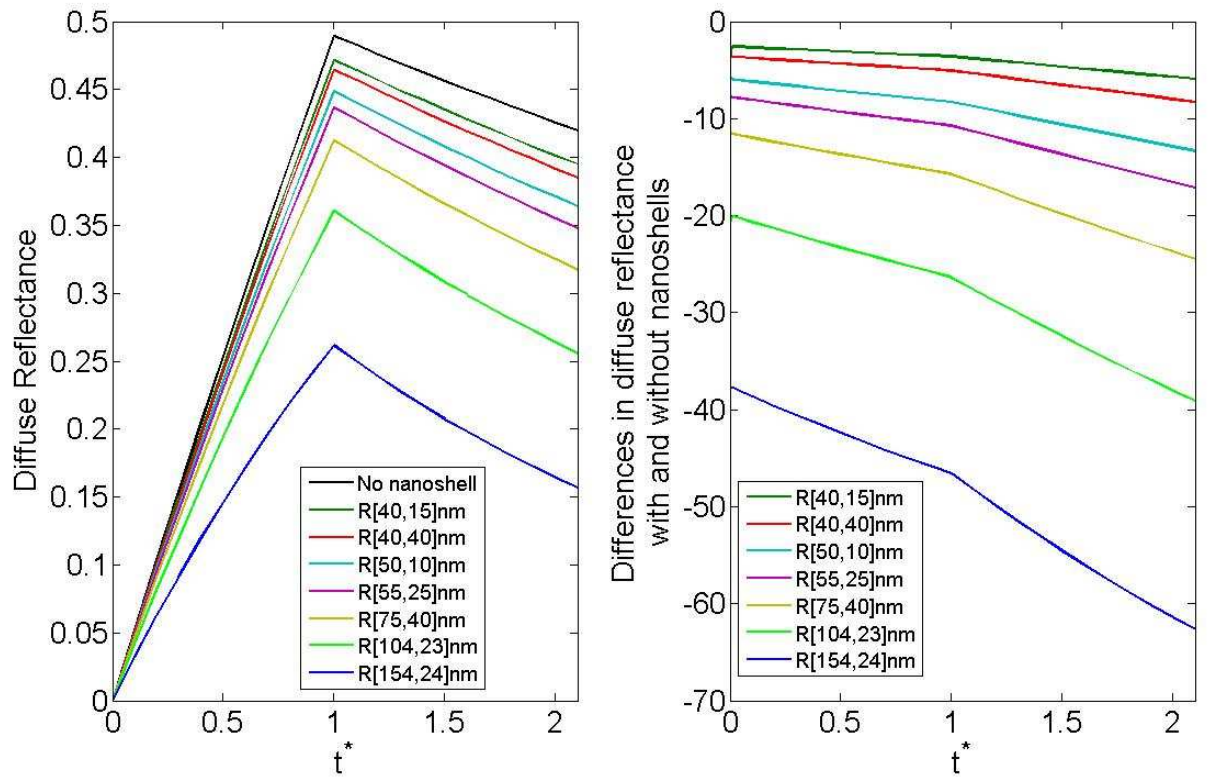


FIGURE 5.6: Transient diffuse reflectance at the laser emitting face when types of nanoshells were embedded in cancerous tissues ($k_{\alpha} = 0.05cm^{-1}$, the scattering coefficient $k_s = 50cm^{-1}$) which were enclosed by normal healthy tissues (absorption coefficient $k_{\alpha} = 1.5cm^{-1}$, the scattering coefficient $k_s = 50cm^{-1}$) as the optical contrast agent. Nanoshells were found in the cancerous tissues only, the nanoshell concentration is $1E10$ nanoshells/ml

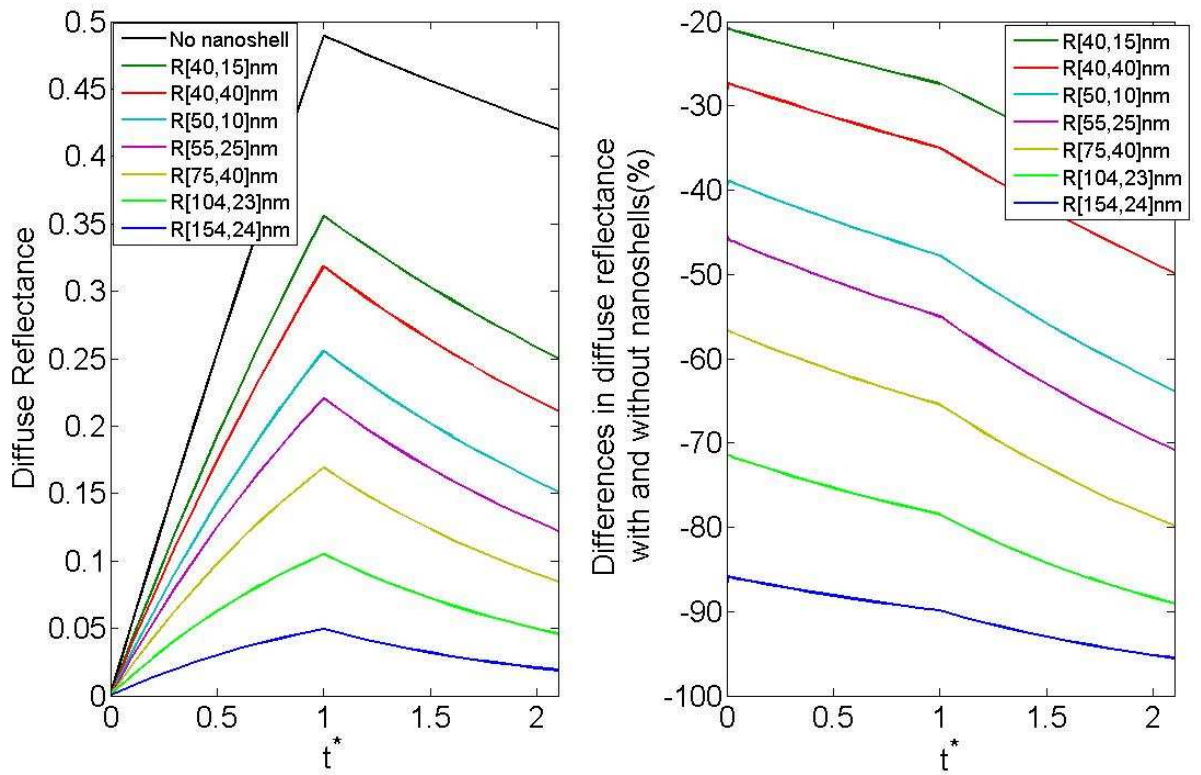


FIGURE 5.7: Transient diffuse reflectance at the laser emitting face when types of nanoshells were embedded in cancerous tissues ($k_{\alpha} = 0.05cm^{-1}$, the scattering coefficient $k_s = 50cm^{-1}$) which were enclosed by normal healthy tissues (absorption coefficient $k_{\alpha} = 1.5cm^{-1}$, the scattering coefficient $k_s = 50cm^{-1}$) as the optical contrast agent. Nanoshells were found in the cancerous tissues only, the nanoshell concentration is $1E10$ nanoshells/ml

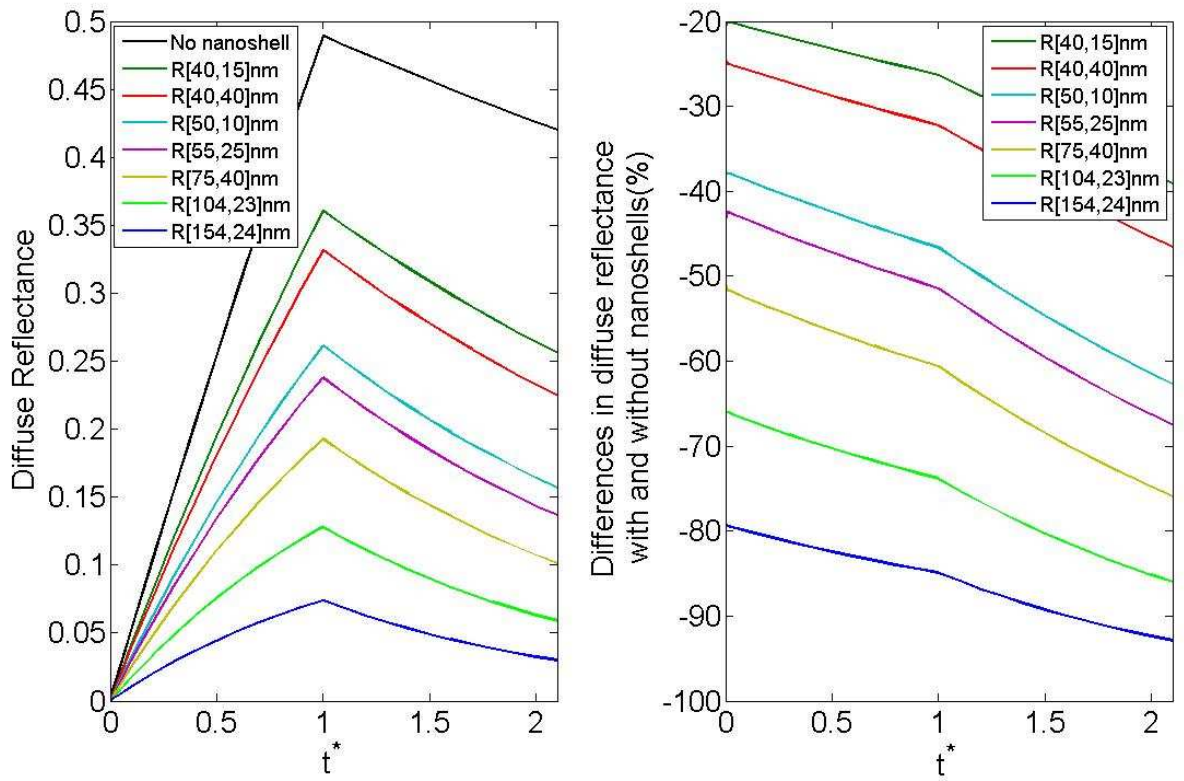


FIGURE 5.8: Transient diffuse reflectance at the laser emitting face when types of nanoshells were embedded in cancerous tissues ($k_{\alpha} = 0.05cm^{-1}$, the scattering coefficient $k_s = 50cm^{-1}$) which were enclosed by normal healthy tissues (absorption coefficient $k_{\alpha} = 1.5cm^{-1}$, the scattering coefficient $k_s = 50cm^{-1}$) as the optical contrast agent. Nanoshells were found in both the cancerous tissues and the enclosing tissue, the nanoshell concentration in the enclosing tissue is $1E9$ nanoshells/ml, the nanoshell concentration in the enclosed cancerous tissue is $1E10$ nanoshells/ml

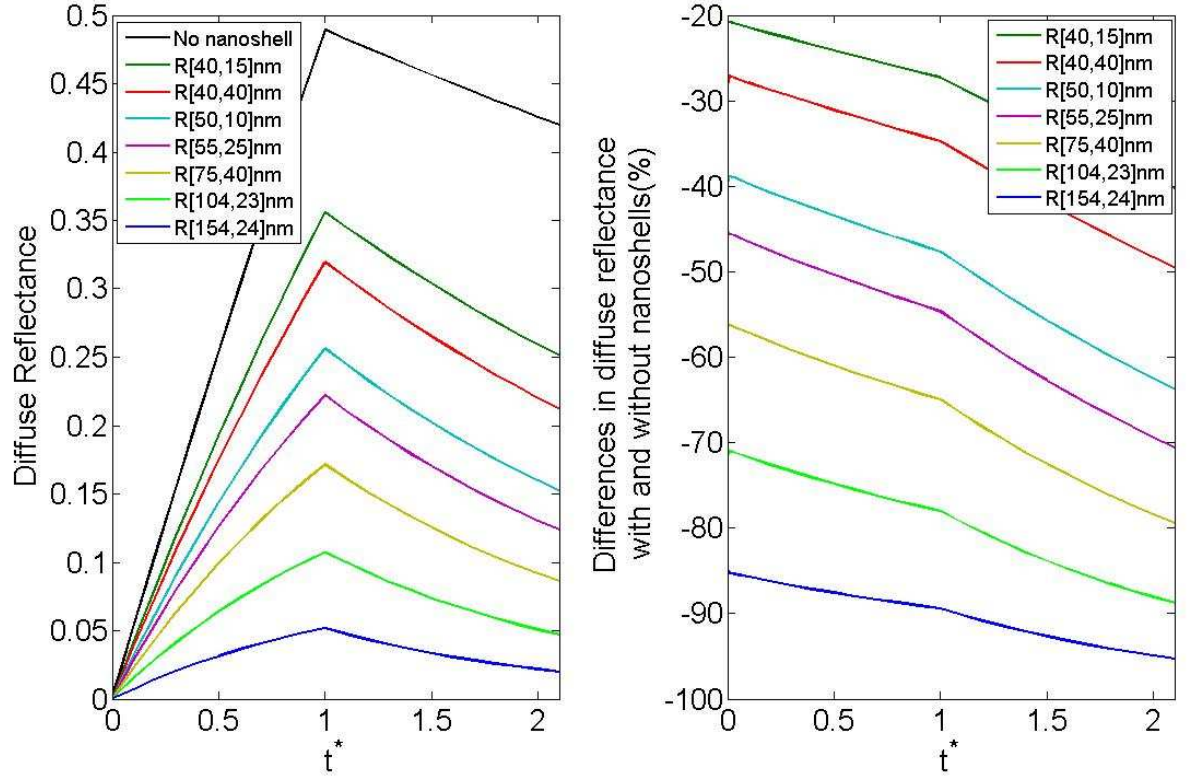


FIGURE 5.9: Transient diffuse reflectance at the laser emitting face when types of nanoshells were embedded in cancerous tissues ($k_{\alpha} = 0.05cm^{-1}$, the scattering coefficient $k_s = 50cm^{-1}$) which were enclosed by normal healthy tissues (absorption coefficient $k_{\alpha} = 1.5cm^{-1}$, the scattering coefficient $k_s = 50cm^{-1}$) as the optical contrast agent. Nanoshells were found in both the cancerous tissues and the enclosing tissue, the nanoshell concentration in the enclosing tissue is $1E10$ nanoshells/ml, the nanoshell concentration in the enclosed cancerous tissue is $1E11$ nanoshells/ml

Bibliography

- [1] Vera J and Bayazitoglu Y(2009)“Gold nanoshell density variation with laser power for induced hyperthermia”,*Int. J. Heat Mass Transfer* 52: 564-573.
- [2] Vera J and Bayazitoglu Y(2009)“A note on laser penetration in nanoshell deposited tissue”, *International Journal of Heat Mass Transfer* 52(13/14): 3402-3406.
- [3] Eillot AM, Schwartz JS, Wang J, Shetty AM, Bougoyne C, O’Neal D, Hazle J and Stafford RJ (2009) “Quantitative comparison of delta P1 versus optical diffusion approximations for modeling nea-infrared gold nanoshell heating”,*Med, Phys* 36(4):1351-1358.
- [4] Pitsillides CM, Joe EK, Wei X, Anderson RR and Lin CP(2003) “Selective cell targeting with light-absorbing microparticles and nanoparticles”, *Biophysical Journal* 84: 4023-4032.
- [5] Zharov VP, Galitovsky V and Viegas M(2003) “Photothermal detection of local thermal effects during selective nanophoto-thermolysis with nanoparticles”, *Applied physics letter* 83(24): 4897-4899.
- [6] Hainfeld JF, Slatkin DN and Smilowitz HM(2004) “The use of gold nanoparticles to enhance radiotherapy in mice”, *Physics in Medicine and Biology* 49: 309-315.
- [7] Huff TB, Tong L, Zhao Y, Hansen MN, Cheng JX and Wei A (2007) “Hyperthermia effects of gold nanorods on tumor cells”, *Nanomedicine* 2(1): 125-132.

- [8] Takahashi H, Niidome T, Nariai A, Niidome Y and Yamada S (2006) “Photothermal reshaping of gold nanorods prevents further cell death”, *Nanotechnology* 17: 4431-4435.
- [9] Huang X, El-Sayed IH, Qian W and El-Sayed MA (2006) “Cancer cell imaging and photothermal therapy in the near-infrared region by using gold nanorods”, *Journal of the American Chemical Society* 128(6): 2115-2120.
- [10] Hirsch LR, Stafford RJ, Bankson JA, Sershen SR, Rivera B, Price RE, Hazle JD, Halas NJ and West JL(2003) “Nanoshell-mediated near-infrared thermal therapy of tumors under magnetic resonance guidance”, *Proceeding of National Academy of Science* 100(23): 13549-13554.
- [11] Loo C, Lin A, Hirsch L, Lee M, Barton J, Halas N, West J and Drezek R(2004) “Nanoshell-enabled photonics-based imaging and therapy of cancer”, *Technology in Cancer Research & Treatment* 3(1): 33-40.
- [12] O’Neal DP, Hirsch LR and Halas NJ (2004) “Photo-thermal tumor ablation in mice using near infrared-absorbing nanoparticles”, *Cancer letters* 209(2):171-176.
- [13] Loo C, Lowery A, Halas NJ, West JL and Drezek R(2005) “Immunotargeted nanoshells for integrated cancer imaging and therapy”, *Nano Lett* 5: 709-711.
- [14] Shi Kam NW, O’Connell M, Wisdom JA and Dai H(2005) “Carbon nanotubes as multifunctional biological transporters and near-infrared agents for selective cancer cell destruction”, *Proceeding of National Academy of Science* 102(33): 11600-11605.
- [15] Chen J, Wiley B, Li ZY, Campbell D, Saeki F, Cang H, Au L, Lee J, Li X and Xie Y(2005) “Gold nanocages: engineering their structure for biomedical applications”, *Advanced Materials* 17: 2255-2261.

- [16] Hu M, Petrova H, Chen J, McLellan JM, Siekkinen AR, Marquez M, Li X, Xia Y and Hartland GV (2006) "Ultrafast laser studies of the photothermal properties of gold nanocages", *Journal of physical chemistry B* 110(4): 1520-1524.
- [17] Connor EE, Mwamuka J, Gole A, Murphy CJ and Wyatt MD (2005) "Gold nanoparticles are taken up by human cells but do not cause acute cytotoxicity", *Small* 1: 325-327.
- [18] Khan JA, Pillai B, Das TK, Singh Y and Maiti S (2007) "Molecular effects of uptake of gold nanoparticles in HeLa cells", *Chembiochem* 8: 1237-1240.
- [19] Shukla R, Bansal V, Chaudhary M, Basu A, Bhonde RR and Sastry M (2005) "Biocompatibility of gold nanoparticles and their endocytotic fate inside the cellular compartment: a microscopic overview", *Langmuir* 21: 10644-10654.
- [20] Katz E and Willner I (2004) "Integrated nanoparticle biomolecule hybrid systems: synthesis, properties, and applications", *Angewandte Chemie International Edition* 43: 6042-6108.
- [21] Goodrich G, Bao L, Gill-Sharp K, Sang K, Wang L and Payne J (2010) "Photothermal therapy in a murine colon cancer model using near-infrared absorbing gold nanorods", *Journal of Biomedical Optics* 15(1): 018001-1 - 018001-7.
- [22] Lu W, Xiong C, Zhang G, Huang Q, Zhang R, Zhang J and Li C (2009) "Targeted photothermal ablation of murine melanomas with melanocyte-stimulating hormone analog - conjugated hollow gold nanospheres", *Clinical Cancer Research* 15: 876-886.
- [23] Lal S, Clare S and Halas N (2008) "Nanoshell-enabled photothermal cancer therapy: impending clinical impact", *Accounts of Chemical Research* 41(12): 1842-1851.

- [24] Terentyuk G, Maslyakova G, Suleymanova L, Khlebtsov N, Khlebtsov G, Akchurin G, Maksimova I and Tuchin V (2009) "Laser-induced tissue hyperthermia mediated by gold nanoparticles: toward cancer phototherapy", *Journal of Biomedical Optics* 14(2): 021016-1 - 021016-9.
- [25] Perrault S and Chan W (2010) "In vivo assembly of nanoparticle components to improve targeted cancer imaging", *Proceeding of the National Academy of Sciences* 107(25): 11194-11199.
- [26] Ruoslahti E, Bhatia S and Sailor M (2010) "Targeting of drugs and nanoparticles to tumors", *The Journal of Cell Biology* 188(6): 759-768.
- [27] Huang X, Jain P, El-Sayed I and El-Sayed M (2006) "Determination of the minimum temperature required for selective photothermal destruction of cancer cells with the use of immunotargeted gold nanoparticles", *Photochemistry and Photobiology* 82: 412-417.
- [28] Lin A, Lewinski N, West J, Halas N, and Drezek R (2005) "Optically tunable nanoparticle contrast agents for early cancer detection: model-based analysis of gold nanoshells", *J. Biomed. Opt.* 10(6): 064035
- [29] Loo C, Hirsch L, Lee M, Chang E, West J, Halas N, and Drezek R (2005) "Gold nanoshell bioconjugates for molecular imaging in living cells", *Optics Letters* 30(9): 1012-1014.
- [30] Loo C, Lee M, Hirsch L, West J, Halas N, and Drezek R (2004) "Nanoshell bioconjugates for integrated imaging and therapy of cancer", *Proceeding of SPIE* 5327: 1-4.
- [31] Huang X, El-Sayed I, Qian W and El-Sayed M (2007a) "Cancer cells assemble and align gold nanorods conjugated to antibodies to produce highly en-

- hanced, sharp, and polarized surface Raman spectra: a potential cancer diagnosis marker”, *Nano Letter* 7: 1591-1597.
- [32] Perrault D and Chan W (2010) “In vivo assembly of nanoparticle components to improve targeted cancer imaging”, *Proceedings of The National Academy of Sciences* 107(25): 11194-11199.
- [33] El-Sayed I, Huang X, and El-Sayed M (2005) “Surface plasmon resonance scattering and absorption of anti-EGFR antibody conjugated gold nanoparticles in cancer diagnostics: applications in oral cancer”, *Nanoletters* 5(5): 829-834.
- [34] Barton JK, Halas NJ, West JL, and Drezek RA (2004) “Nanoshells as an optical coherence tomography contrast agent”, *Proc.SPIE* 5316: 99-106.
- [35] Wang Y, Xie X, Wang X, Ku G, Gill K, O’Neal D, Stoica G, and Wang L (2004) “Photoacoustic tomography of a nanoshell contrast agent in the in vivo rat brain”, *Nanoletters* 4(9): 1689-1692.
- [36] Brigger I, Dubernet C and Couvreur P(2002) “Nanoparticles in cancer therapy and diagnosis”, *Adv. Drug. Delivery Rev.* 54: 631-651.
- [37] Liang C, Sung KB, Richards-Kortum RR, Descour MR (2002) “Design of a high-numerical aperture miniature microscope objective for an endoscopic fiber confocal reflectance microscopy”, *Appl. Opt.* 41(22): 4603-4610.
- [38] Sung KB, Liang C, Descour M, Collier T, Follen M, Richards-Kortum R (2002) “Fiber-optic confocal reflectance microscope with miniature objective for in vivo imaging of human tissue”, *IEEE Trans. Biomed.Eng.* 49(10): 1168-1172.
- [39] Collier T, Lacy A, Richard-Kortum R, Malpica A, Follen M (2002) “Near real-time confocal microscopy of amelanotic tissue”, *Acad. Radiol.* 9(5): 504-512.

- [40] Xie TQ, Zeidel ML, Pan YT (2002) “Detection of tumorigenesis in urinary bladder with optical coherence tomography: optical characterization of morphological changes”, *Opt. Exp.* 10: 1431-1443.
- [41] Matheny ES, Hanna NM, Jung WG, Chen Z, Wilder-Simth P, Mina-Araghi R, Brenner M (2004) “Optical coherence tomography of malignancy in hamster cheek pouches”, *J. Biomed.Opt.* 9(5): 978-981.
- [42] Drexler W, Morgner U, Kartner FX, Pitris C, Boppart SA, Li XD, Ippen EP and Fujimoto JG (1999) “ In vivo ultrahigh resolution optical coherence tomography”, *Opt. Lett.* 24: 1221-1223.
- [43] Fujimoto JG(2003) “Optical coherence tomography for ultrahigh resolution in vivo imaging”, *Nat. Biotech* 21(11):1361-1367.
- [44] Zeng H, Petek M, Zorman MT, McWilliams A, Palcic B, and Lam S (2004) “Integrated endoscopy system for simultaneous imaging and spectroscopy for early lung cancer detection”, *Opt. Lett* 29(6): 587-589.
- [45] Amelink A, Sterenborg H, Bard M, and Burgers S (2004) “In vivo measurement of the local optical properties of tissue by use of differential path-length spectroscopy”, *Opt. Lett.* 29 (10):1087-1089.
- [46] Sokolov K, Nieman LT, Myakov A, and Gillenwater A (2004) “Polarized reflectance spectroscopy for pre-cancer detection”, *Technol. Cancer Res. Treat* 3(1):1-14.
- [47] Onofre MA, Sopsto MR, and Navarro CM (2001) “Reliability of toluidine blue application in the detection of oral epithelial dysplasia and in situ and invasive squamous cell carcinomas”, *Oral Surg. Oral Med. Oral. Pathol. Oral. Radiol. Endod.* 91(5): 535-540.

- [48] Tincani AJ, Brandalise N, Altemani A, Scanavini RC, Valerio J, Lage HT, Molina G, and Martins AS (2000) “Diagnosis of superficial esophageal cancer and dysplasia using endoscopic screening with a 2% Lugol dye solution in patients with head and neck cancer”, *Head and Neck* 22(2): 170-174.
- [49] Feng Y, Rylander MN, Bass J, Oden JT and Diller K (2005) “Optimal design of laser surgery for cancer treatment through nanoparticle-mediated hyperthermia therapy”, *NSTI-Nanotech* 1: 39-42.
- [50] Feng Y, Fuentes D, Hawkins A, Bass J, Rylander MN, Eillot A, Shetty A, Stafford RJ and Oden JT (2009) “Nanoshell-mediated laser surgery simulation for prostate cancer treatment”, *Engineering with Computers* 25 : 3-13.
- [51] Tjahjono I. and Bayazitoglu Y (2008) “Near-Infrared light heating of a slab by embedded nanoparticles”, *International Journal of Heat and Mass Transfer* 51:1505-1515.
- [52] Bayazitoglu Y(2009) “Nanoshell Assisted Cancer Thermal Therapy: Numerical Simulations”, *Proceedings of the 2nd ASME Micro/Nanoscale Heat Mass Transfer: An International Conference, Shanghai*.
- [53] Wang LH, Jacques SL, Zheng LQ (2005) “MCML-Monte Carlo modeling of light transport in multi-layered tissues”, *Computer Methods and Programs in Biomedicine* 47: 131-146.
- [54] Mie G (1908) “Beitrge zur Optik trber Medien, speziell kolloidaler Metallsungen. Leipzig”, *Annals of Physics* 330: 377445.
- [55] Lin A (2006) “Nanoengineered contrast agents for biophotonics: modeling and experimental measurements of gold nanoshell reflectance”, Ph. D dissertation, Rice University.

- [56] Toricelli A, Pifferi A, Taroni P, Giambattistelli E and Cubeddu R (2001) “In vivo optical characterization of human tissues from 610-1010nm by time-resolved reflectance spectroscopy”, *Phys. Med. Biol.*46: 2227-2237.
- [57] Doornbos R, Lang R, Aalders M, Cross F and Sterenborg H(1999) “The determination of in vivo human tissue optical properties and absolute chromophore concentrations using spatially resolved steady-state diffuse reflectance spectroscopy”, *Phys. Med. Biol.* 44: 967-981.

6

Future work

The research on the medical applications of nanoparticles toward tumor/cancer diagnosis and treatment has been ongoing for almost a decade by now. Much related information, knowledge and learning have been accumulated in this field. Overall speaking, the decade long research in this field has been very successful and inspiring. Many pioneering explorations have been done and many exciting discoveries have been made, repeatedly confirming the medical potentials of nanoparticles. However, in my opinion, the most meaningful achievement so far is that the ten years knowledge accumulation has gradually revealed the underlying core problems and challenges of pushing forward the biomedical applications of nanoparticles. Only by facing up to these problems and challenges and finding solutions for them, can the so-called nanoparticle assisted tumor/cancer diagnosis and treatment really be pushed from the bench to the clinic.

Based on this present study, I feel the following problems are pending to be answered in order to push forward the research in this field:

1. To be used as the photo-thermal agent, the absorption spectrum of nanoparticles plasmonic resonance should be explored and the nanoparticles are engineering to be such that the absorption heavily dominates over the scattering. When exposed to the laser exposure, these particles are desired to be point-wise heat source, converting the laser photon energy to thermal heat and transmitting the produced heat to their surrounding medium very quickly. However, the preferentially absorbing nature of the nanoparticles most likely would refrain the laser lights from both propagating deep and diffusing out (see Chapter 3 and Chapter 4 for more details about this problem). Therefore, an immediate concern is that whether the refrainments in the optical transportation could be so strong that current laser delivery techniques could not guarantee that the intended laser dose could be delivered to the targeted location. In other words, how to deliver the intended laser dose efficiently to the targeted site, particularly, if the targeted site is relatively deep down from the laser irradiance beam frontier?

2. In Chapter 5, a preliminary numerical study has been carried out on using the ultra-short pulse laser and nanoparticles for optical imaging process. The ultra-short pulse lasers, whose pulses last from picoseconds to nanoseconds, have attracted much interest and attention of researchers from the optical imaging field during the recent few years. Optical signals, including the diffuse reflectance and the transmissivity, induced by the ultra short pulse lasers, are temporal and it is believed that time revolving optical signals carry more information of the optical properties of the tissue within which the laser lights propagate through. Although to my information, systematic investigations on using ultra short pulsed lasers for nanoparticle assisted optical imaging procedures have not been reported yet, I believe that such explorations will be brought to the calendar very soon. Within such a context, it is natural to pop up the question: Besides being used for the diagnostic optical imag-

ing, could the ultra-short pulse laser be used for therapies as well? It is worthwhile to search for the answer of this question because the bio-nano community as a whole believes that, the most ideal way of applying nanoparticles would be that nanoparticles could perform dual functions as the optical contrast agent for diagnostic imaging and being the photo-thermal agent for the therapy. Therefore, if it could be proved that ultra short pulse lasers are feasible power sources for therapies, then, at least one forward step could be made toward the goal of using nanoparticles dually.